On mass transport and surface kinetics in protein crystal growth

Maurits Heijna

On mass transport and surface kinetics in protein crystal growth

een wetenschappelijke proeve op het gebied van de
Natuurwetenschappen, Wiskunde en Informatica

Proefschrift

ter verkrijging van de graad van doctor
aan de Radboud Universiteit Nijmegen,
op gezag van de rector magnificus prof. mr. S.C.J.J. Kortmann,
volgens besluit van het College van Decanen
in het openbaar te verdedigen op maandag 21 april 2008
om 15:30 uur precies

door

Maurits Christiaan Robert Heijna

geboren op 24 september 1976
te Utrecht

Promotores: Prof. dr. E. Vlieg
                 Prof. dr. W.J. de Grip

Copromotores: Dr. W.J.P. van Enckevort
                 Dr. P.C.M. Christianen

Manuscriptcommissie:
Prof. dr. ir. J.C. Maan
Prof. dr. S. S. Wijmenga
Prof. dr. J. M. García Ruiz (Universiteit van Granada, Spanje)

Contents

Chapter 1

Introduction

1.1 Proteins

Proteins nowadays receive full attention from the scientific community. When one tries "protein" as a search term in Google Scholar[1] one finds in excess of 13 million hits. By the same method one finds 9 million hits on "metals", and less on other classes of (solid state) materials (see table 1.1). The same picture is given by a search on Web of Science[2] in which one can find 93 thousand hits on protein publications during 2004 alone*. Although one could argue that apparently the protein science community writes a lot, it is a good indication of the interest people have in the subject. Part of the interest in proteins originates from its omnipresence in living organisms, including ourselves. Proteins play a crucial role in many biochemical processes on a cellular level, for instance catalysis (enzymes), structural or mechanical functions (e.g. cytoskeleton, transport), cell signaling, and immune responses (e.g. references [3–7]).

Protein molecules consist of a chain of L-α-amino acids, linked together by peptide bonds (fig. 1.1). The length of this chain ranges typically from 100 to 27,000 amino acids, thus ranking proteins in the class of biological macro-

---

*2004 is the last year for which the Web of Science database returns less than 10^5 hits on "protein", which is the maximum number of hits shown by the search engine.

Table 1.1: Google Scholar and Web of Science "experiment" for different classes of solid state materials: Number of Google Scholar hits at February 10, 2007; Web of Science database hits for the year 2004.

Search term	# of hits ($\times 10^6$) Google Scholar	# of hits ($\times 10^4$) Web of Science, 2004
protein	13.6	9.3
metal	9.6	3.0
semiconductor	2.5	0.64
ceramic	1.3	0.37
oxides	1.0	0.59
superconductor	0.2	0.15

molecules together with molecules like nucleic acids and polysaccharides[8]. Although proteins contain many amino acids, the variation in type is limited to a set of 20 different amino acids, which differ in the composition of their side chains, or "residues". The specific sequence of amino acids in a protein is called its primary structure and is usually given by a list of three-letter abbreviations of the amino acid type (fig. 1.2a).
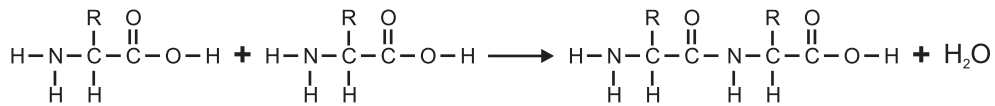
Figure 1.1: The peptide bond.

The peptide bonds between the amino acids form the backbone of the protein molecule. Within the backbone the peptide bonds can occur in different conformations which can have a repetitive character. Typical local repetitive structures are the α-helix and the β-sheet (fig. 1.2b), the occurrence of which is called the secondary structure of a protein. The three-dimensional structure of a protein as a whole is called its tertiary structure (fig. 1.2c). In general, a protein molecule seeks to minimize its free energy by folding up into a specific

three-dimensional structure, which is stabilized through salt bridges, hydrogen bonds, disulfide bonds and van der Waals forces. Here, the side chains play an important role as their (non-)polarity determines the type of interactions possible and thus the 3D structure. For instance, globular proteins tend to form a hydrophobic core with the hydrophobic residues on the inside of the molecule and the hydrophilic ones at the surface[9].
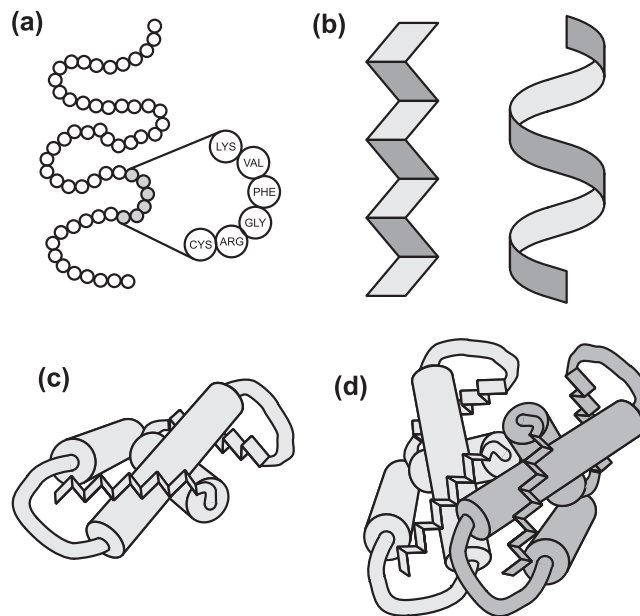
Figure 1.2: Structure of protein molecules. (a) Primary structure; the sequence of amino acids in the protein. (b) Secondary structure; β-sheets and α-helices, formed by a sequence of amino acids linked by hydrogen bonds. (c) Tertiary structure; the folding of the amino acid chain. The cylinders represent α-helices, the zigzags β-sheets (d) Quaternary structure; a protein complex consisting of more than one amino acid chain.

The biological function of a protein usually cannot be understood from the amino-acid sequence alone. Often, the biological potency of proteins depends on their 3D structure[10, 11], while the primary structure for the different conformations is the same. Another example for which knowledge of the 3D

Table 1.2: Number of structures in the Protein Data Bank[12] divided by type of biological macromolecule and the methods used to obtain their structures, as of the 10th of February 2007.

Method	Proteins	Nucleic Acids	Protein/NA Complexes	Other	Total	Deposited in 2006
XRD	32723	941	1526	28	**35218**	5650
NMR	5208	738	128	7	**6081**	872
EM†	95	10	38	0	**143**	34
Other	78	4	3	0	**85**	12
Total	**38104**	**1693**	**1695**	**35**	41527	**6568**

structure is required is drug design. To design a drug which enters and blocks the active site of a malfunctioning protein molecule, knowledge of the atomic positions of this site is required. Thus, to understand the functionality or, in the case of diseases, dysfunctionality of a protein, one would like to know the tertiary structure of the protein molecule.

Various methods exist to determine the three-dimensional structure of a protein molecule down to atomic resolution. Solved structures usually are deposited in the Protein Data Bank[12], whose statistics show that the main method for structure determination is X-ray diffraction (XRD), see table 1.2. For small protein molecules (<20.000 Da) atomic resolution can be achieved by nuclear magnetic resonance (NMR). Neutron scattering and electron microscopy form a minority in solved structures.

Any structure determination starts with the acquisition of the protein from biological material (fig. 1.3a). Tissue containing the protein of interest is dissolved, and subsequently purified by methods like centrifugation and high precision liquid chromatography (HPLC) [13]. For a structure determination by XRD, a single crystal is required (fig. 1.3b) to acquire diffraction patterns like the one shown in figure 1.3c. The positions of the peaks in these patterns supply information on the crystal lattice, i.e. the axis lengths and angles of the

---

†Electron Microscopy

unit cell. In addition, the intensities of the peaks supply information on the electron density in three dimensions[14, 15], thus enabling one to form a 3D picture of the structure of the protein molecule (fig. 1.3d). Both the signal-to-noise ratio and the spatial extent of the diffraction pattern are of importance for the level of structural detail one can obtain by XRD[16]. These factors depend on the quality of the crystal, i.e. the better the crystalline order, the better the XRD pattern. Thus, a prerequisite for structure determination by XRD is to obtain a high quality single crystal of the protein of interest. However, proteins do not crystallize easily, and structure determinations seldomly reach details of 1 Å, whereas resolutions of 2~3 Å are more common[12], which for macromolecules usually is insufficient to obtain essential structural information. In the process of 3D structure determination of biological macromolecules, growing XRD quality crystals remains the bottle-neck.

1.2   Protein crystal growth

Because most proteins are water soluble, they are usually crystallized from aqueous solutions. For crystals to be formed in the solution, the protein concentration must be higher than the equilibrium concentration, i.e. the protein concentration in a saturated solution. From a thermodynamical point of view, the chemical potential difference between the dissolved phase and the crystalline phase, $\Delta\mu$, indicates which of these two phases is the most energetically favourable, being positive for crystallization and negative for dissolution. In the case of crystal growth from solution, the chemical potential difference is related to the solute concentration, c, by

$$\Delta\mu = kT \ln \frac{f\,c}{f_{eq}\,c_{eq}} \;,\tag{1.1}$$

in which k is Boltzmann's constant, T is the temperature, f (f_{eq}) is the (equilibrium) activity coefficient of the protein in solution, c is protein concentration, and c_{eq} is the equilibrium protein concentration. In this equation the activity coefficient of the dissolved protein is assumed to be independent of concentration. In equation 1.1 one can see that to create a supersaturated
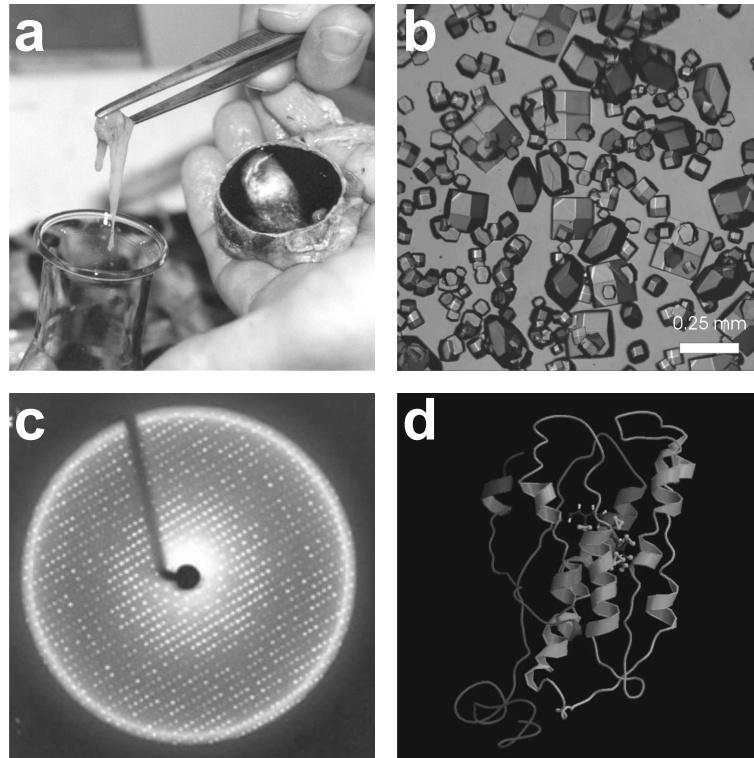
Figure 1.3: The process of determination of the 3D molecular structure of proteins. (a) Acquisition of proteins from biological material, in this case bovine rhodopsin from the retina of cow's eyes (photo by courtesy of Petra Bovee-Geurts, NCMLS). (b) Growth of protein single crystals. Shown is a sample of tetragonal hen egg-white lysozyme (HEWL) crystals. (c) Example of an X-ray diffraction pattern of a protein. (d) 3D structure of bovine rhodopsin (PDB entry 1jfp), showing the folding of the protein.
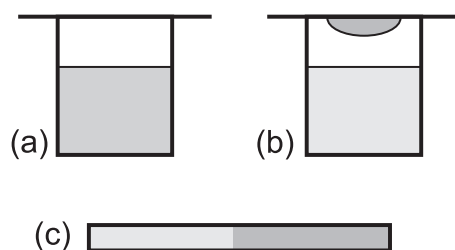
Figure 1.4: Crystallization methods for proteins. (a) In the batch method a supersaturated mixture is prepared and left to nucleate and crystallize. (b) The vapour diffusion method is based on vaporization of the undersaturated mother liquor due to a salt concentration difference with the larger reservoir. (c) For the free interface diffusion method a protein solution and a salt solution are carefully brought into contact in a capillary. Due to diffusion a range of different supersaturation conditions is formed.

solution, one can either increase the protein concentration or decrease the equilibrium concentration. The equilibrium concentration depends on many parameters including temperature, pH, and solution composition[17–19]. These parameters make up the complex multidimensional phase diagram of the protein in solution.

Traditional macromolecular crystallization techniques include the batch method, vapour diffusion methods, and free interface diffusion (fig. 1.4). These methods have in common the use of salts to reduce the protein solubility, while also polyethylene glycol (PEG) is often used as an additional precipitating agent. The methods differ in the starting point and pathways through the phase diagram (fig. 1.5). Every protein has its own specific phase diagram, and a crystallization experiment should be designed to fit this phase diagram. When crystallizing a protein for XRD purposes, usually its phase diagram is unknown. A first attempt thus can be nothing more than an educated guess based on experience with similar proteins.

To find the protein crystallization conditions, one screens the solution composition, i.e. type and concentration of additives, by trail-and-error. A typical protein crystallization can take days up to months. To reduce the time to find
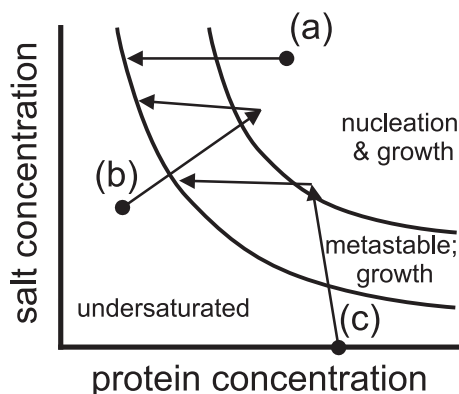
Figure 1.5: Pathways through the phase diagram for three of the most common macromolecular crystallization techniques. As an example, salt concentration is taken as solubility parameter. (a) Batch crystallization. (b) Vapour diffusion. The solution approaches supersaturation from undersaturated conditions. (c) free interface diffusion, or counter diffusion. In this method a whole range of conditions is tested at the same time. Shown is a pathway starting at zero salt concentration

the proper conditions for XRD-quality, crystals screenings are performed in multi-well plates. Experiments are often automated by robotics[20]. An advantage of the trail-and-error approach is that it increases the rate at which XRD-quality protein crystals can be produced with little knowledge of the complex machinations of the crystal growth process. However, the educated guess on the correct crystallization conditions becomes more educated if one acquires knowledge on the fundamental aspects of the protein crystallization processes.

1.3   Surface kinetics versus mass transport

Protein crystals grow mainly via the same mechanisms as small molecules[9, 21], i.e. normal (or rough) growth, birth-and-spread, and spiral growth. Surface kinetics processes, like surface diffusion, step bunching, and impurity blocking also occur for macromolecular crystals [22–24] albeit quantitatively

different compared to small molecular crystals. For instance, the step kinetic coefficient β_s for proteins is in the order of $10^{-4}\ cm\,s^{-1}$, while for small molecules it is in the order of $10^{-2}\ cm\,s^{-1}$ [25].

Solution crystal growth is a sequence of two processes. The first process is transport of mass toward the surface of the crystal, the second is the incorporation of growth units into the crystal (fig. 1.6). In other words, without a fresh supply of growth units to the solution-crystal interface the crystal cannot grow, and a crystal will not grow as well in case it is difficult to attach growth units to the surface. The overall growth rate of the crystal is determined by the slowest of these two processes.
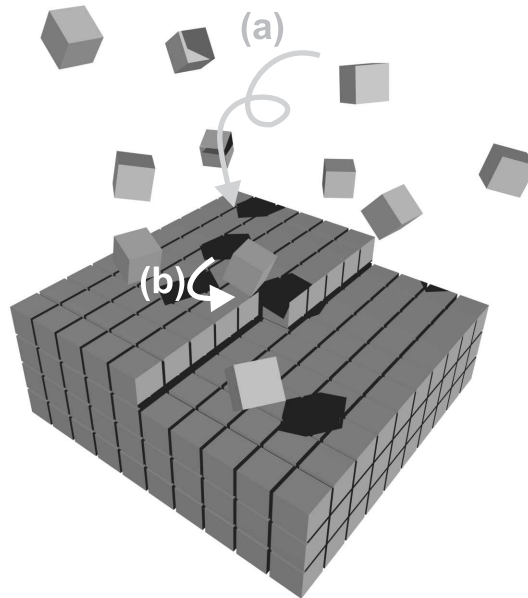
Figure 1.6: Schematic, simplified, representation of the crystallization process, consisting of a mass transport part (a) and a surface incorporation part (b). The crystal growth rate is determined by the slowest of these two parts.

Mass transport itself can be subdivided into two different processes; con-

vection and diffusion. Natural convection is a consequence of density differ-
ences in the solution, created by the growing crystal, and gravity. Convection
is an effective means of mass transport, strong enough to drag along large
impurities. Upon reaching the crystal surface, these impurities can become
incorporated into the crystal and thus reduce the crystal quality. Therefore,
mass transport is not only important for the crystal growth rate, but also for
the crystal quality[25–28]. Research focuses on various methods to influence
the transport of impurities to the surface, all of them aiming to cancel convec-
tional mass transport. These methods include the use of gels[29–31], experi-
ments in microgravity (i.e. in space) [28, 32], using nanoliter volumes[33, 34],
and, as described in this thesis, the use of inhomogeneous high magnetic fields.
With convection cancelled, diffusion remains as the sole means of transport,
and is a slow process for large impurities compared to the diffusion of protein
molecules. Another beneficial effect of cancelling convection is the reduced lo-
cal supersaturation during growth. For nucleation a high $\Delta\mu/kT$ is required,
but for further growth a low supersaturation is preferred because experience
shows low $\Delta\mu/kT$ to give higher quality crystals. Thus, it is thought that the
cancellation of convection should improve crystal quality[25–28]. However, if
the growth is very much limited by the rate of diffusion, the morphology of a
crystal can become unstable or dendritic[35]. To grow a good quality crystal,
one needs to find the right balance between all processes.

1.4   So, this thesis....

The work in this thesis focuses on the crystallization of the protein hen egg-
white lysozyme (HEWL). Hen egg-white lysozyme is a well-known protein,
and serves as the guinea pig of protein crystallization. Although much has
been written about this protein, its crystallization process is still not well un-
derstood. For instance, in 1937 the protein was crystallized for the first time[‡],
but only since the 1990's the role of liquid-liquid phase separation for the
crystallization process became more apparent[36, 37]. In this thesis, the lyso-

---

[‡]By P. Abraham and R. Robinson.

zyme crystallization process is investigated from a physico-chemical point of view, mainly by optical microscopy, aiming to contribute to the understanding of mass transport and surface kinetics in protein crystal growth. The first few chapters focus on the surface processes during crystallization, revealing anisotropic growth spirals by atomic force microscopy, and showing growth inhibition, probably due to a self-poisoning mechanism, by optical microscopy. Subsequently, the focus shifts to mass transport, showing its influence in the formation of spherulites, and in crystal growth from a liquid-liquid phase separated system. Control of mass transport is the topic of chapters 6 and 7, in which the use of high magnetic fields to cancel convection during crystal growth is explored. In the last chapter, surface kinetics and mass transport find each other in an experiment in which both processes compete to dominate, resulting in morphologically unstable crystals.

References

[1] http://scholar.google.com.

[2] Web of Science, Thompson, http://isiknowledge.com.

[3] Kerssemakers, J.; Munteanu, E.; Laan, L.; Noetzel, T.; Janson, M.; Dogterom, M. *Nature* **2006,** *442,* 709-712.

[4] Uemura, T.; Kashiwagi, K.; K.Igarashi, *The Journal of Biological Chemistry* **2007,** *282,* 7733-7741.

[5] Rautsi, O.; Lehmusvaara, S.; Salonen, T.; Häkkinen, K.; Sillanpää, M.; Hakkarainen, T.; Heikkinen, S.; Vähäkangas, E.; Ylä-Herttuala, S.; Hinkkanen, A.; Julkunen, I.; Wahlfors, J.; Pellinen, R. *The Journal of Gene Medicine* **2007,** *9,* 122-135.

[6] Boyman, O.; Kovar, M.; Rubinstein, M.; Surh, C.; Sprent, J. *Science* **2007,** *311,* 1924-1927.

[7] Pawson, T. *Nature* **1995,** *373,* 573-580.

[8] Hennessy, D.; Buchanan, B.; Subramanian, D.; Wilkosz, P.; Rosenberg, J. *Acta Crystallographica D* **2000,** *56,* 817-827.

[9] McPherson, A. *Crystallization of Biological Macromolecules;* Cold Spring Harbor Laboratory Press: New York, 1999.

[10] Svensson, M.; Håkansson, A.; Mossberg, A.-K.; Linse, S.; Svanborg, C. *Proceedings of the National Academy of Sciences of the United States of America* **2000,** *97,* 4221-4226.

[11] Kang, T.; Radic, Z.; Talley, T.; Jois, S.; Taylor, P.; Kini, R. *Biochemistry* **2007,** *46,* 3338-3355.

[12] RCSB-Protein Data Bank, http://www.pdb.org.

[13] Lorber, B.; Giegé, R. Biochemical aspects and handling of macromolecular solutions and crystals. In *Crystallization of Nucleic Acids and Proteins*; Oxford University Press: Oxford, 1999.

[14] Drenth, J. *Principles of Protein X-Ray Crystallography;* Springer: New York, 1999.

[15] Sawyer, L.; Turner, M. X-ray analysis. In *Crystallization of Nucleic Acids and Proteins*; Oxford University Press: Oxford, 1999.

[16] Weiss, M. *Applied Crystallography* **2001,** *34,* 130-135.

[17] Howard, S.; Twigg, P.; Baird, J.; Meehan, E. *Journal of Crystal Growth* **1988,** *90,* 94-104.

[18] Cacioppo, E.; Pusey, M. *Journal of Crystal Growth* **1991,** *114,* 286-292.

[19] Riès-Kautt, M.; Ducruix, A. From solution to crystals with a physico-chemical aspect. In *Crystallization of Nucleic Acids and Proteins*; Oxford University Press: Oxford, 1999.

[20] Stevens, R. *Current Opinion in Structural Biology* **2000,** *10,* 558-563.

[21] Land, T.; Malkin, A.; Kuznetsov, Y.; McPherson, A.; Yoreo, J. D. *Physical Review Letters* **1995,** *75,* 2774-2777.

[22] Malkin, A.; Kuznetsov, Y.; McPherson, A. *Journal of Crystal Growth* **1999,** *196,* 471-488.

[23] Astier, J.; Bokern, D.; Lapena, L.; Veesler, S. *Journal of Crystal Growth* **2001,** *226,* 294-302.

[24] Plomp, M.; McPherson, A.; Malkin, A. *Proteins* **2003,** *3,* 486-495.

[25] Chernov, A. *Journal of Structural Biology* **2003,** *142,* 3-21.

[26] Carter, D.; Limb, K.; Hoa, J.; Wright, B.; Twigg, P.; Miller, T.; Chapman, J.; Keeling, K.; Rublea, J.; Vekilov, P.; Thomas, B.; F. Rosenberger, A. C. *Journal of Crystal Growth* **1999,** *196,* 623-637.

[27] Snell, E.; Judge, R.; Crawford, L.; Forsythe, E.; Pusey, M.; Sportiello, M.; Todd, P.; Bellamy, H.; Lovelace, J.; Cassanto, J.; G.E.O.Borgstahl, *Crystal Growth & Design* **2001,** *1,* 151-158.

[28] Thomas, B.; Chernov, A.; Vekilov, P.; Carter, D. *Journal of Crystal Growth* **2000,** *211,* 149-156.

[29] Robert, M.; Lefaucheux, F. *Journal of Crystal Growth* **1988,** *90,* 358-367.

[30] Biertümpfel, C.; Basquin, J.; Suck, D.; Sauter, C. *Acta Crystallographica D* **2002,** *58,* 1657-1659.

[31] Garcia-Ruiz, J.; Moreno, A.; Viedma, C.; Coll, M. *Materials Research Bulletin* **1993,** *28,* 541-546.

[32] Kundrot, C.; Judge, R.; Pusey, M.; Snell, E. *Crystal Growth & Design* **2001,** *1,* 87-99.

[33] Carter, D.; Rhodes, P.; McRee, D.; Tari, L.; Dougan, D.; Snell, G.; Abolac, E.; Stevens, R. *Journal of Applied Crystallography* **2005,** *38,* 87-90.

[34] Cherezov, V.; Caffrey, M. *Journal of Applied Crystallography* **2003,** *36,*
     1372-1377.

[35] Nanev, C. *Progress in Crystal Growth and Characterization of Materials*
     1997, *35,* 1-26.

[36] Berland, C.; Thurston, G.; Kondo, M.; Broide, M.; Pande, J.;
     O. Ogun, G. B. *Proceedings of the National Academy of Sciences of the
     United States of America* **1992,** *89,* 1214-1218.

[37] Muschol, M.; Rosenberger, F. *Journal of Chemical Physics* **1997,** *107,*
     1953-1962.

Chapter 2

An atomic force microscopy study of the (001) surface of triclinic hen egg-white lysozyme crystals

The (001) surface of triclinic hen egg-white lysozyme-nitrate crystals has been investigated by *in-situ* atomic force microscopy to compare its growth mechanisms and properties to those of other lysozyme pseudo-polymorphs. The crystal morphology derived from connected net analysis using the macrobond concept is in good agreement with the experimental morphology of the crystals. Surface structures observed by AFM include rounded steps, growth spirals, 3D nucleation and impurity pinning. The growth spirals are rounded and highly anisotropic. Both screw and edge dislocations are found, characterised by hollow core outcrops. The observed hollow core radii are an order of magnitude larger than theoretical values, but do depend on supersaturation. From the rounded shape of the spirals and the absence of 2D nucleation we find an edge free energy $1.3 < \gamma_m/kT < 3$, which is similar to values found for tetragonal lysozyme. Serrated step patterns indicate impurity pinning. Complete blocking by impurities is not found. The step velocity is proportional to the relative

supersaturation. Using the kinetic coefficient, we find a sticking fraction of 4×10^{-4} for HEWL molecules to become attached to a kink, which is significantly higher compared to the sticking fraction for orthorhombic lysozyme.

2.1   Introduction

X-ray diffraction is the main route towards structure determination of protein macromolecules. To increase X-ray resolution scientists continue to search for methods to improve protein crystal quality, using both practical and fundamental approaches[1]. In both approaches hen egg-white lysozyme (HEWL) is often used as a model compound to test new techniques and ideas.

Lysozyme can be crystallised in various crystal structures, for example tetragonal, orthorhombic, monoclinic and triclinic[2, 3]. The crystal structure obtained depends on the choice of the salt used as crystallising agent. Using sodium nitrate as a crystallising agent, monoclinic as well as triclinic HEWL can be grown[4, 5]; sodium chloride yields tetragonal HEWL. In the tetragonal form, chloride ions are incorporated into the crystal structure, whereas in the triclinic form nitrate ions are incorporated. Therefore, these different lysozyme crystal structures are pseudo-polymorphs.

Atomic force microscopy (AFM) is often used to investigate crystallisation mechanisms, because crystal growth is a surface process. Most AFM studies on HEWL involve the tetragonal form[6, 7], despite that this crystal structure with eight molecules per unit cell is the most complex of all HEWL pseudo-polymorphs. Few AFM studies involve other pseudopolymorphs of lysozyme (orthorhombic[8], monoclinic[9]). Triclinic lysozyme has the most simple structure with only one molecule per unit cell. This implies a Kossel-like [10] growth mechanism for triclinic lysozyme, which should make the growth process relatively simple to understand. In spite of its simplicity and yielding the highest XRD resolution[11], the growth mechanisms of triclinic lysozyme have not yet been investigated in detail. In this paper we aim for a more quantitative understanding of the growth mechanisms and properties of triclinic lysozyme-nitrate crystals, such as morphology, spiral growth, step kinetics and the edge

free energy, and compare our observations with other pseudo-polymorphs to investigate similarities and differences.

2.2 Experimental procedures

2.2.1 Crystal growth

HEWL from Sigma-Aldrich (lot nrs. 51K7028 and 81K1554) was used, without further purification, as source material for crystal growth. Sodium nitrate, sodium acetate and acetic acid were all of analytical grade. A buffer stock solution of sodium acetate and acetic acid was made in deionised water (>15 MΩcm) to result in a 0.05 M NaCH$_3$COO/HCH$_3$COO solution of pH 4.5. Salt and lysozyme stock solutions were made in buffer solution. The buffer, salt and protein stock solutions were filtered over 0.2 μm membranes (Schleicher & Schuell). By mixing these three stock solutions, the crystallisation solutions were prepared containing 10 mg/ml HEWL and 0.2 M NaNO$_3$ in 0.05 M NaCH$_3$COO/HCH$_3$COO buffer.

A glass cell of 2 ml volume was filled with mother liquor. This glass cell was placed in a larger water flow cell. Temperature was controlled by flowing water from a Julabo F25 temperature controlled water bath around the glass cell. To grow triclinic lysozyme crystals, a strategy similar to that reported in [5] was used. First, the temperature is set at 4 $^{\circ}$C for 12 hours to induce nucleation. This turns the solution turbid and both monoclinic and triclinic crystals are formed. After 2 hours, the glass cell is taken out of its flow cell and subsequently left at room temperature (18-25°C) for 5 to 6 days. At room temperature the number of nuclei is largely reduced and the turbid system turns clear. The meta-stable monoclinic crystals dissolve, while the stable triclinic crystals continue to grow slowly.

2.2.2 *In-situ* atomic force microscopy

To prepare the triclinic lysozyme crystals for AFM measurements the contents of the glass cell is emptied into a glass petri-dish. A solution of 3 mg/ml HEWL

and 0.2 M NaNO$_3$ in sodium acetate buffer of pH 4.5 is added up to the rim of the petri-dish (12 ml in total). Then the petri-dish is sealed off, preventing exposure of the solution to the ambient air. Exposure to the ambient air results in the growth of spherulites and a surplus of small crystallites. The solution containing triclinic crystals is left at room temperature for a further 2 days. During this period of continued growth the crystals adhere to the glass bottom of the petri-dish, which prevents specimen slip during the AFM measurements

Before measurements a part of the solution is removed from the petri-dish so that 5.5 ml remained. The petri-dish is placed on the stage of a Nanoscope Dimension (Digital Instruments Inc.) AFM. An oxide-sharpened silicon nitride tip is used. The cantilever, a 120-μm-high isosceles triangle, has a spring constant of 0.06 Nm^{-1}. The microscope is operated in constant-force contact mode, and both height and deflection images are recorded. Surfaces of lysozyme crystals are very soft. In order to reduce tip-induced damage of the surface, the feedback controls are set to react quickly. Slow response runs the tip into the surface of the crystal, wearing out a square pattern.

Observations were carried out at room temperature, which can fluctuate. In our case we had a spread of 2°C during a single day of measurements and a range from 20.5^{o}C up to 24.5^{o}C for all experiments. During the AFM observations samples of solution of 100 μl were removed from the petri-dish at half hour intervals. From these samples the lysozyme concentration was determined by UV absorption measurements at 281.5 nm (absorption coefficient: 2.64 l g^{-1} cm^{-1} [12]). Temperature and concentration are necessary parameters to determine the driving force of crystal growth $\frac{\Delta\mu}{kT}$, which is given by

$$\frac{\Delta\mu}{kT} = \ln\frac{fc}{f_{eq}c_{eq}} \ , \tag{2.1}$$

where k is Boltzmann's constant, T is the temperature, f and f_{eq} are activity coefficients, which we take as independent of concentration, and c and c_{eq} are the actual and equilibrium lysozyme concentrations, respectively, at a given temperature. To change the driving force $\frac{\Delta\mu}{kT}$ during AFM measurements, part of the solution was replaced with a more dilute solution of lysozyme.

2.3 Results and discussion

2.3.1 Morphology

Figure 2.1a shows a typical example of the triclinic lysozyme crystals grown in our laboratory for AFM measurements. From X-ray diffraction data we obtained the following cell parameters for the triclinic unit cell with space group P_1: a=27.18 Å, b=31.88 Å, c=34.21 Å, α=88.67^o, β=108.42^o and γ=111.98^o. These values are very close to the unit cell parameters reported in the literature [11] and confirm the identity of the triclinic pseudo-polymorph. Using angular measurements of crystals viewed in the optical microscope as well as single crystal X-ray diffraction measurements we indexed the crystal faces of our lysozyme crystals. The crystals were usually oriented in the petri-dish with either their (001) or (00$\bar{1}$) face upward*. Besides the (00$\pm$1), (0$\pm$10) and ($\pm$100) faces, which were always observed, in many cases we also encountered (1$\bar{1}$0) and ($\bar{1}$10).

To compare experiment with theory, the crystal shape was calculated by using the cell parameters and the computer program Facelift [13]. This program is based on the Hartman-Perdok theory [14], which relates crystal morphology to internal structure using bond energies between growth units. We start with finding the connected nets in the triclinic lysozyme structure. As a lysozyme molecule has many bonds of various strengths with each neighbouring molecule, we used the macrobond energies as derived by Matsuura and Chernov [15] to sum these. These bonds are used in Facelift to identify the connected nets and to calculate the vacuum attachment energies belonging to them (table 2.1). From the attachment energies we find the growth form by assuming that the growth rate of each face is proportional to its attachment energy[14]. Experiments and calculations show good agreement: both show the ($\pm$100), (0$\pm$10), (00$\pm$1), (1$\bar{1}$0) and ($\bar{1}$10) faces to be present in the morphology (figure 2.1b). The distance between the opposite (001) and (00$\bar{1}$) faces of our crystals is smaller than in the calculated morphology, because growth

---

*As the absolute configuration of the non-centrosymmetric crystal structure is not known, we are not able to distinguish between the faces (hkl) and ($\bar{h}\bar{k}\bar{l}$).
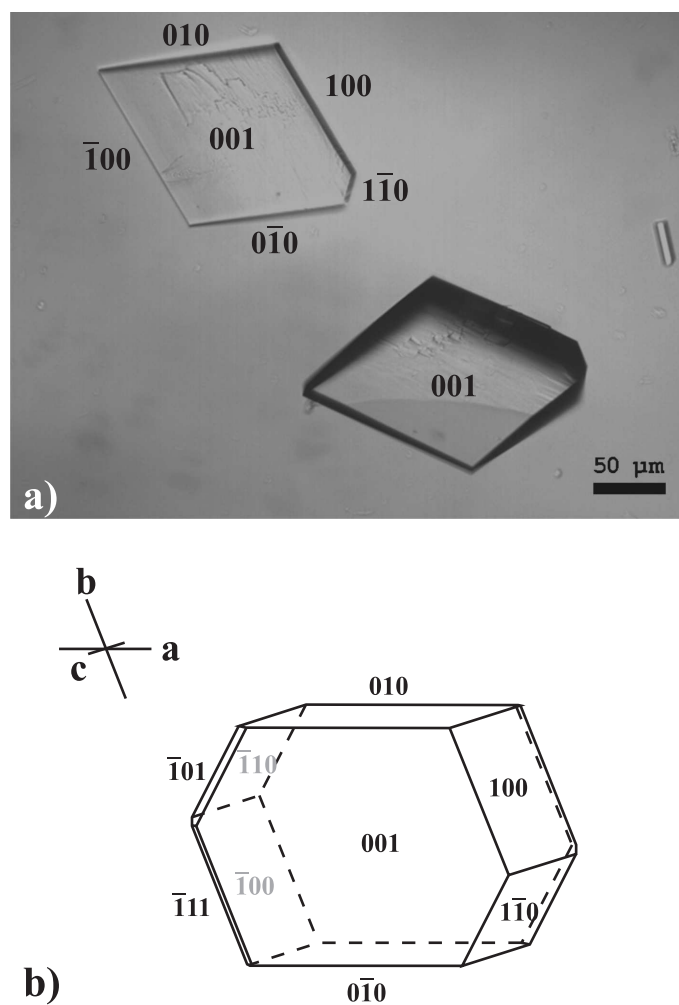
Figure 2.1: a) Optical view of triclinic hen egg-white lysozyme crystals, obtained in a 0.2 M NaNO$_3$, 50 mM acetate buffer solution as described in section 2.2. b) Morphology of triclinic lysozyme as calculated by Facelift. This is *not* a 3D representation, but a projection of the morphology on the *ab*-plane.

Table 2.1: Attachment energies in vacuum and interplanar distances for the connected nets of triclinic HEWL crystals on the basis of macrobonds.

Connected net (F-face)	$E_{Att.}$ (kJ/mol)	d_{hkl} (nm)
001	-382	3.23
010	-418	2.95
100	-464	2.39
$\bar{1}$10	-536	2.35
10$\bar{1}$	-706	2.33
1$\bar{1}\bar{1}$	-712	2.17

downwards is stopped by the glass bottom of the cell or petri-dish. $(1\bar{1}1)/(\bar{1}1\bar{1})$ and $(\bar{1}01)/(10\bar{1})$ faces are not found in our experiments. These faces are very small, and it might be difficult to reveal them by optical microscopy due to projection effects. We conclude that the macrobond concept introduced by Matsuura [15] is a good approximation for calculations on triclinic lysozyme.

2.3.2   Surface structure

AFM measurements on the (001) and (00$\bar{1}$) faces of triclinic lysozyme show various surface phenomena. Step sources were observed in the form of single and multiple growth spirals (figure 2.2a). We also found incorporation of sedimented particles (figure 2.2b). In a few cases we observed tip-induced 2D nucleation. Also 3D islands were observed. The step patterns often showed bunching and impurity pinning. The outcrops of both screw and edge dislocations at the surface are characterised by hollow cores. No differences in surface morphology were found on the opposite (001) and (00$\bar{1}$) faces. Therefore in the rest of this paper both faces are indexed as (001).
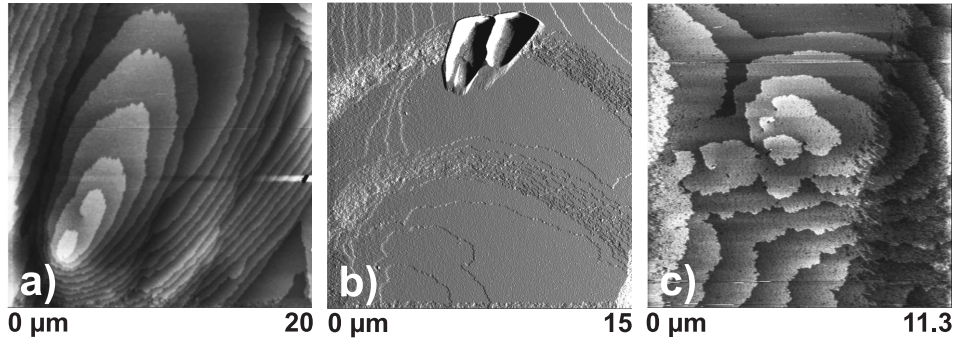
Figure 2.2: *In-situ* AFM images of growth patterns on the (001) face of triclinic lysozyme crystals. (a) Height image showing a double spiral. (b) Deflection image of a sedimented particle being incorporated into the crystal. (c) Height image of an array of dislocations. On the left and right side of image (c), scan-induced damage to the surface is visible.

Spirals and other step sources

A variety of growth spirals was found: single spirals, double spirals, closed loop steps originating from dislocation pairs of opposite sign, and dislocation arrays (see figure 2.2c). The step height of these spirals was always 3.2 ± 0.2 nm, matching the interplanar distance, d_{001}, of 3.23 nm. This height also corresponds to approximately the diameter of one lysozyme molecule.

Individual or groups of dislocations are the sources of the spirals. The component of the Burgers vector perpendicular to the surface, $b_\perp$, is equivalent to d_{001}. All spirals found are rounded, regardless of supersaturation, and polygonal spirals were not observed. The spiral shapes were found to be highly anisotropic (see figure 2.3a), appearing elliptical with the long axis parallel to the [010] direction. Besides the anisotropy between the $<010>$ and the $<100>$ directions, a strong anisotropy exists between the [010] and the [0$\bar{1}$0] direction. This indicates a large difference in step velocity for these opposite directions. Entire triclinic lysozyme crystals also show polar growth along $<010>$, as we concluded from in-situ optical microscopic observations.

While spirals are the main source of steps on the (001) surface of triclinic
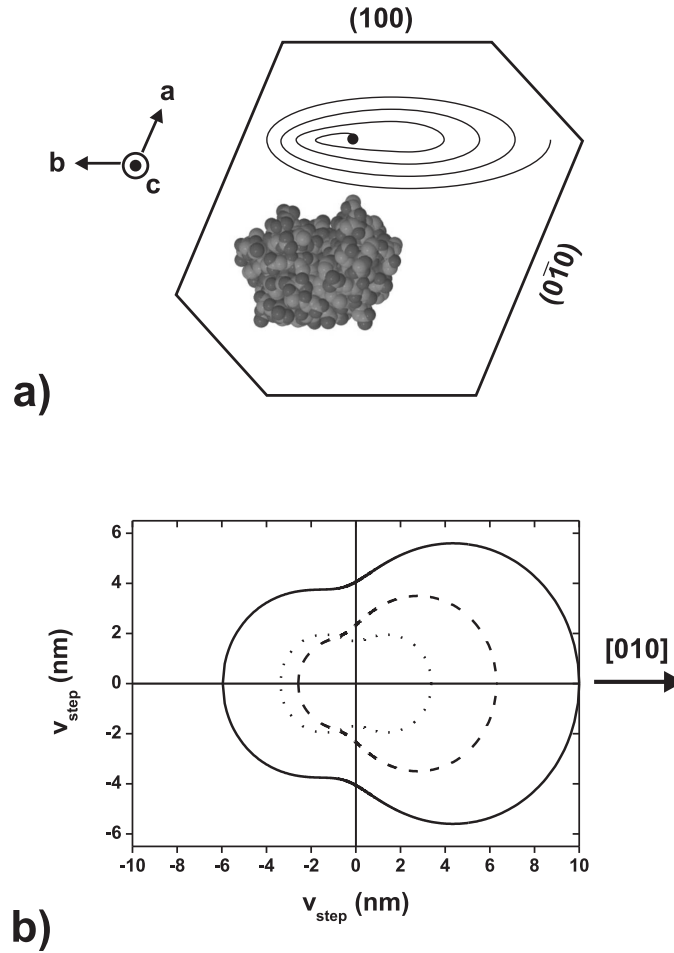
Figure 2.3: Morphology of the anisotropic spirals on (001) lysozyme. a) Orientation of spirals with respect to the crystal habit. A lysozyme molecule is drawn to show its orientation with respect to crystal habit. b) Kinetic Wulff plot showing step velocity versus step orientation for spirals on the (001) surface at $\frac{\Delta\mu}{kT} = 0.4$ (dashed line) and $\frac{\Delta\mu}{kT} = 1.2$ (solid line). Spirals are approximated by ellipses to simplify the reconstruction. The dotted line shows the Wulff plot in case the growth centre would lie at the centre of the ellipse.

HEWL, other sources do occur. Step sources in the form of 3D islands were observed (see figure 2.4). These islands are likely to originate from sedimented particles, as reported by e.g. [[16, 17]], which may originate from the solution-air interface where the local supersaturation is increased due to evaporation. The islands expand as step bunches of typically 40-80 steps high. The accumulated steps propagate at a slightly slower rate than the mono-molecular steps of the spirals. The 3D islands show the same anisotropy as the spirals.

In a few cases we observed 2D nucleation of islands. Taking into account their position at the edges of the AFM scan range, these nuclei are likely a result of tip-surface interaction. Two-dimensional nucleation does not play a role as a step source for any of the applied supersaturations in this study.

Steps

The step speed is anisotropic, as is clear from the shape of the spirals. The shape of the spirals at large distance from the growth centres is determined by the anisotropy in step velocity. Using a two-dimensional inverse kinetic Wulff construction [18] it is possible to determine the step speed as a function of the orientation from the shape of the spirals (see appendix). Figure 2.3b shows the Wulff plots obtained in this way for low and high $\frac{\Delta\mu}{kT}$. The step velocity is higher for the high $\frac{\Delta\mu}{kT}$, but the polar velocity plots are similar in shape, thus the anisotropy in step propagation changes little with supersaturation.

Step speeds for the slowest step directions were determined from series of scans at various supersaturations. Figure 2.5 shows the results as function of HEWL concentration and of driving force $\frac{\Delta\mu}{kT}$. We find the step speed to be linear in its concentration dependence:

$$v_{step} = \beta \frac{c - c_{eq}}{c_{eq}} \; , \tag{2.2}$$

in which c_{eq} is 0.4 mg/ml and β is 2.9 nm/s. The equilibrium concentration was verified by additional experiments in which the occurrence of growth or dissolution of seeded triclinic HEWL crystals was examined in solutions of different concentrations around c_{eq}. The linear dependence of the step velocity
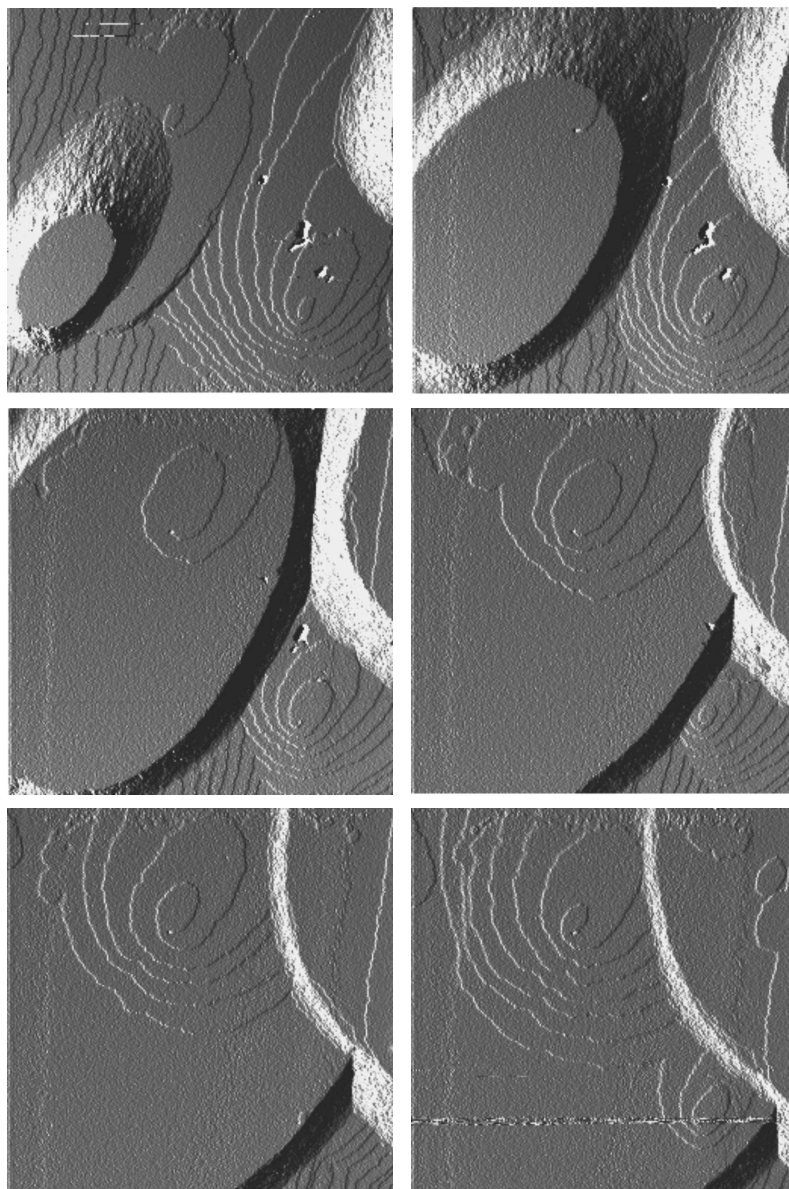
Figure 2.4: Series of *in-situ* AFM deflection images of a 20 μm x 20 μm surface area showing the evolution of 3D islands on the (001) face of triclinic lysozyme. The pictures are recorded at a 8.5 minute interval. Spirals and hollow cores are overgrown by the islands, but reappear on top.
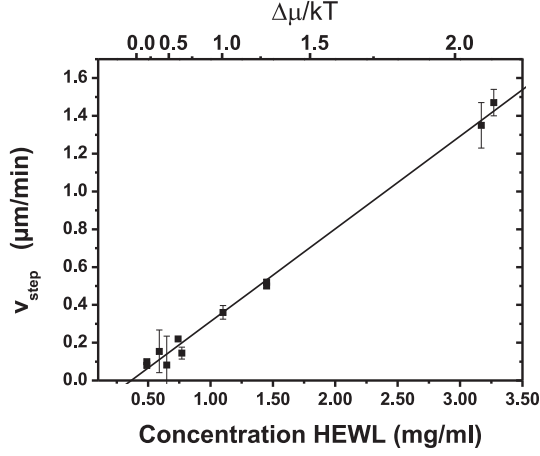
Figure 2.5: Step velocity as a function of HEWL concentration and driving force. The step velocities are averaged values for those directions that correspond with the "slowest" 180° segment of the kinetic Wulff plot. The average temperature is 295 K.

complies with the linear law of Wilson-Frenkel [19, 20]:

$$
\begin{aligned}
v_{step} \quad &\propto \quad J_0 \left(e^{\Delta\mu/kT} - 1 \right) \\
&\approx \quad J_0 \frac{c - c_{eq}}{c_{eq}} \ ,
\end{aligned}
\tag{2.3}
$$

where equation (2.1) was used to rewrite the exponential.

All spirals observed were rounded, even for the driving force approaching zero. This indicates a high kink density of the steps and thus low kink energies ϕ_k. Another possible cause of the roundness of the spirals is impurity pinning. As the step speed is proportional to the supersaturation σ, this influence must be small.

Impurity pinning has been observed on protein crystals [21] before, including tetragonal lysozyme [22]. Although in our experiments the influence of impurity pinning on step propagation is small, serrated step patterns as shown in figure 2.6 provide evidence for its presence. This conclusion is supported
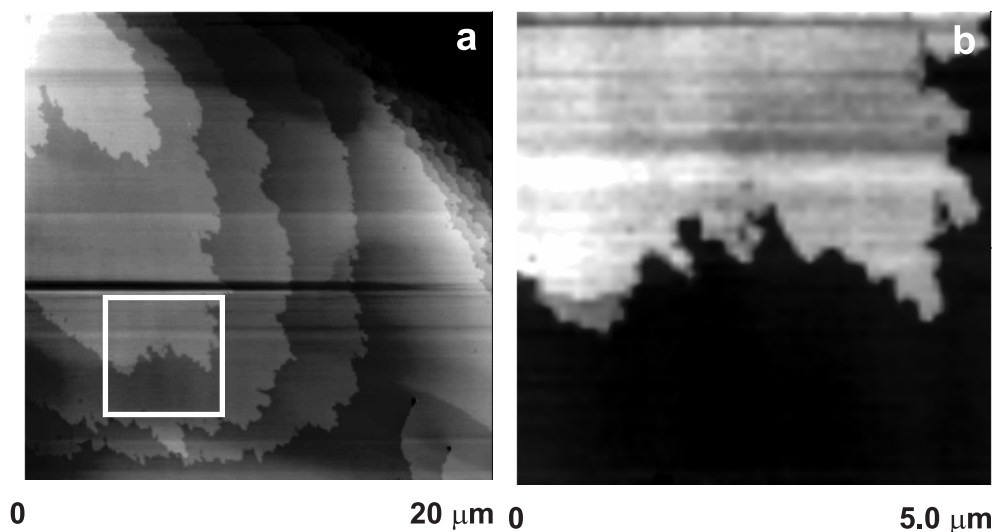
Figure 2.6: Impurity pinning of steps on the (001) face of triclinic lysozyme. a) AFM scan giving an overview of the serrated step patterns. In some areas, the shape of subsequent steps is roughly the same, which confirms impurity pinning. b) Detail, showing the part outlined by the square in a). The two deep 'fjords' indicate local blocking of steps by impurities.

by the fact that the perturbed patterns are often repetitive for subsequent steps. Steps are blocked completely by impurities if the distance d between adjacent impurities is smaller than twice the radius of the critical nucleus size, i.e. $d < 2\,r_c$. The critical radius, r_c, depends on the edge free energy γ and the driving force. Thus, also the critical distance d_{crit} depends on γ and $\Delta\mu$:

$$d_{crit} = \frac{2\gamma\Omega}{\Delta\mu} \; , \qquad\qquad (2.4)$$

in which Ω is the volume of one growth unit (25.9 nm^3 for triclinic lysozyme). As the edge free energy for triclinic lysozyme crystals is not available in literature, we use that of tetragonal lysozyme. For tetragonal lysozyme literature reports values[†] in the order of 1 mJ/m^2 [7, 23–25]. To calculate an upper limit for the critical distance d_{crit}, we use the largest value of γ from literature

---

[†]In the protein literature edge free energy is often expressed as a measure of energy per

and the smallest value of $\Delta\mu$ from our experiments. We find $d_{critical}$ <75 nm. Locally, blocking can occur by inhomogeneously distributed groups of closely separated impurities, with the steps flowing around these groups. Such a mechanism is suggested by the presence of deep "fjords" (figure 2.6b). However, on average, the distance between pinning points is larger than d_{crit}, the smallest observed distance being 180±10 nm, and impurity blocking is not expected to occur. Moreover, if impurity adsorption had a strong blocking effect, step bunches would move faster than individual steps [26]. We observed the opposite, which is in compliance with the limited role of impurities. To get an idea of the molecular weight of the impurities in the source material, we performed Matrix Assisted Laser Decoupling/Ionising Time-of-Flight (MALDI-TOF) measurements on our HEWL material. The impurities found by this method were of low molecular weight (< 5 kDa).

Hollow cores

Similar to other types of protein crystals [16, 27, 28], the outcrops of dislocations ending at the (001) surface of the triclinic lysozyme crystals are marked by hollow cores. The hollow cores remain present even when step bunches pass over them (see figure 2.4). Two types of hollow cores were observed. The first type emits steps and it produces either spirals (figure 2.4) or extra steps in step trains (figure 2.7). Steps emitted from hollow cores of this type all have a height of d_{001}, indicating screw dislocations with a Burgers vector b=[001]. As for a given supersaturation the hollow core radii of this type are all the same, we do not expect an extra edge component [100] or [010] for the dislocations, because in that case a part of the hollow cores would be wider.

The second type of hollow core does not emit steps (see figure 2.7). Here only edge dislocations are involved. As the hollow core radii have practically the same size as that of screw dislocations, the Burgers vector must be comparable in length. Edge dislocations have a Burgers vector of either [100] or [010], which is close to the Burgers vector length $\|[001]\|$ of a screw disloca-

---

molecule. Conversion from "per molecule" to "per square meter" depends on the choice of surface area per molecule.
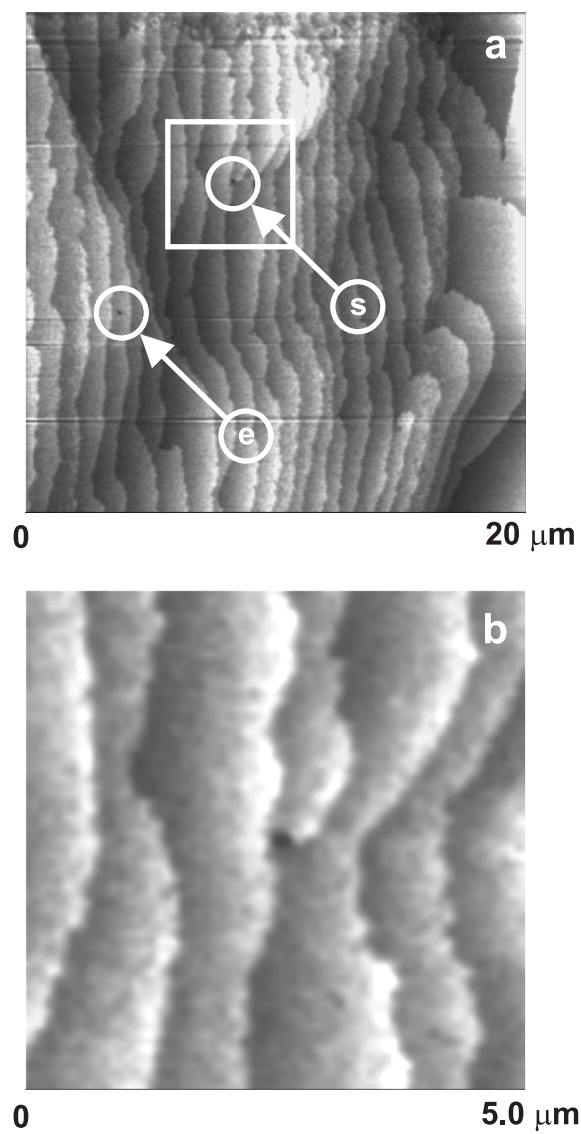
Figure 2.7: a) AFM height image showing hollow core outcrops on the (001) surface of triclinic lysozyme. Arrows indicate a screw (s) and an edge (e) dislocation. b) Detail showing the hollow core in the part outlined by the square in figure a).
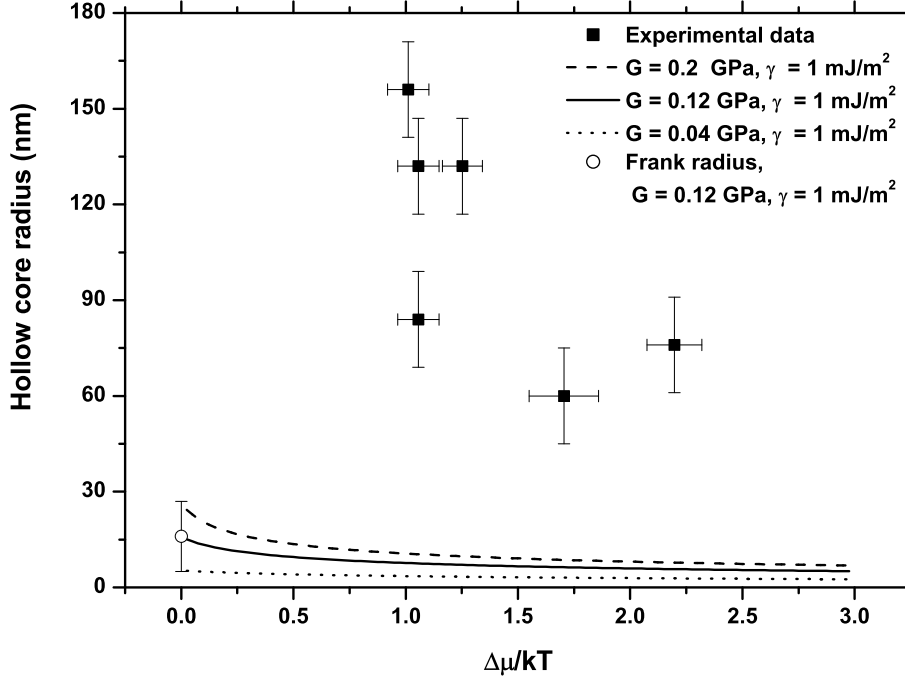
Figure 2.8: Hollow core radius versus driving force. Squares indicate experimental data. The circle indicates the (calculated) Frank radius for $\gamma = 1 \ mJ/m^2$ and $G = 0.12 \ GPa$. The lines indicate calculated hollow core radii as a function of driving force $\frac{\Delta\mu}{kT}$ for $\gamma = 1 \ mJ/m^2$ and various shear moduli G. Experimental data are an order of magnitude larger than theoretical values.

tion. Thus, dislocations ending on the (001) surface of triclinic lysozyme have Burgers vectors [001], [100] or [010].

For various driving forces, radii of hollow cores associated with screw dislocations were determined by recording cross sections through the hollow cores in the AFM height images (figure 2.8). The theoretically expected hollow core size follows from thermodynamic models [29–31] as well as from the analysis of an isotropic growth spiral [32], both considering the stress field around its dislocation:

$$r_{hc} = -\frac{\gamma\,\Omega}{2\,\Delta\mu}\left(1 - \sqrt{1 + 4\frac{G\,b^2\,\Delta\mu}{8\pi^2\,\gamma^2\,\Omega}}\right) \ . \tag{2.5}$$

In this equation, r_{hc} is the hollow core radius, b the length of the Burgers vector and G the shear modulus. Using literature data on the Young's modulus for triclinic lysozyme crystals [33] and a Poisson's ratio of 0.25, the shear modulus was calculated to be 0.12±0.08 GPa. The calculated hollow core radius for an edge free energy of 1 mJ/m^2 versus driving force is indicated by the lines in figure 2.8. The open circle indicates the Frank radius [29],

$$r_f = \frac{G\,b^2}{8\,\pi^2\,\gamma} \; , \tag{2.6}$$

using the same parameter values. This radius corresponds with the theoretical size of the hollow core at equilibrium. The measured core radius decreases with increasing driving force, as is expected from theory. Data, however, show that the observed hollow core radii are one order of magnitude larger than theory. Great care should be taken in interpreting measured hollow core sizes. It is energetically unfavourable for a hollow core to simply end at the surface. At the surface, a trumpet-shaped hollow core outcrop develops as described by Frank [29] and Srolovitz and Safran [34] for equilibrium. Combined TEM and AFM measurements on GaN confirm the existence of such craters [35]. Due to the AFM tip radius of about 20 nm the crater region is imaged, but the actual hollow core is not. It cannot descent down a hollow core of comparable radius more than approximately 5 nm. The combination of a crater-like outcrop and limitations due to the AFM tip size results in measuring a wider and more shallow pattern than the actual hollow core[35]. Liu *et al.* [36] modelled the shape of the crater region at equilibrium and at $\frac{\Delta\mu}{kT} = 0.2$ using Monte Carlo simulations. These indicate a steeper crater region for $\frac{\Delta\mu}{kT} > 0$. Although we did not measure the actual core size, the supersaturation dependence of the core radius is expected to be reflected in the measured crater radii.

2.4 Step energetics and kinetics

2.4.1 Energetics

As mentioned above, the fact that the steps are rounded implies a low kink energy and thus a high kink density. For the (001) face of a Kossel crystal the

transition between rounded and polygonised spirals occurs for a kink energy $\phi_k/kT \approx 1.5$[37], which corresponds with a kink density of $n_k \approx 0.37$ [38]. So for (001) triclinic lysozyme $\phi_k/kT \leq 1.5$, if we assume a similar behaviour of the connected net in the d_{001} slice. On the other hand, the edge free energy must be relatively high, as no 2D nuclei were observed. This apparent contradiction can be explained by looking at the connected net in the d_{001} slice, as shown in figure 2.9 for a step parallel to [010]. For the other steps the situation is similar. For this simple crystal graph the kink and edge energy are proportional to $\frac{1}{2}E_D$ and $\frac{1}{2}(E_C + E_A)$ respectively. Since the macrobond energies E_A, E_C and E_D do not differ too much [15], one can state that the edge energy is roughly twice the kink energy. For the Kossel crystal the edge energy is lower, being equal to the kink energy.
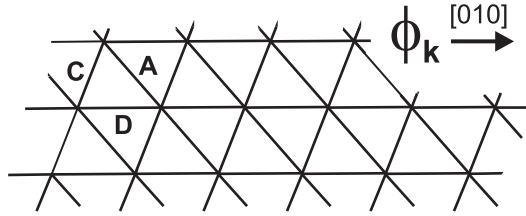
Figure 2.9: Connected net in the d_{001} slice of triclinic HEWL showing a step parallel to [010]. Bond notation is according to Matsuura and Chernov [15]. A kink is indicated by ϕ_k.

An alternative way to make an estimate of ϕ_k/kT using the equivalent wetting assumption[14]:

$$\frac{\phi_k}{kT} = \frac{1}{2}\frac{E_D}{E_{cryst}} \times \frac{\Delta H_{diss}}{RT} \ . \tag{2.7}$$

This gives ϕ_k/kT=3.7, which is too high. From this value it follows that we have "more than equivalent wetting" [39], i.e. a situation in which the solvent interacts stronger with the crystal surface than with dissolved protein molecules.

A lower limit for ϕ/kT can be obtained from the fact that the surface was never kinetically roughened, even for the highest $\frac{\Delta\mu}{kT} = 2$. Thus, the critical

nucleus size was always larger than one growth unit. This sets a lower limit to the edge energy per molecule γ_m of

$$\frac{\gamma_m}{kT} > \frac{1}{2}\frac{\Delta\mu}{kT} \; , \tag{2.8}$$

which follows from the expression for the critical nucleus $r^* = \gamma\Omega/\Delta\mu$ with the edge energy γ *per square meter* . Thus, $\gamma_m/kT \approx 2\phi/kT$ is larger than 1. As for (001) lysozyme $\phi_k \approx \phi$, it follows from the above that the edge energy must be confined between

$$1 < \frac{\gamma_m}{kT} < 3 \; .$$

If we consider an edge free energy of tetragonal lysozyme of 1.2 mJ/m^2 [24] and an effective surface of 3 by 3 nm (i.e. approximately one side of the molecule), we find γ_m/kT is 1.3 for this crystal form. This edge free energy is within the range we find for triclinic lysozyme. At a driving force of 0.5 tetragonal lysozyme grows by 2D nucleation[7], whereas for triclinic HEWL 2D nucleation is absent up to a driving force of at least 2. Thus, the edge free energy of the triclinic form will be higher than $1.3kT$.

For isotropic spirals, the step spacing far away from the spiral centre is related to the critical radius by [30]

$$\Delta r^\infty = 19 r_c \; . \tag{2.9}$$

At $\frac{\Delta\mu}{kT} = 1$ the critical radius is between 3 to 9 nm for $1 < \frac{\gamma_m}{kT} < 3$. Thus, the step spacing of the spiral arms should be 60-180 nm for this supersaturation. However, experiment shows step spacings varying from 1 up to 5 μm, which is one order of magnitude larger. This discrepancy is explained by the fact that the stress field of the dislocation associated with the hollow core slows down the rotation speed of the spiral [40]. For constant step speed this results in a larger step spacing. A simple expression for the step spacing of a spiral emerging from a central obstacle with perimeter length P has been put forward by De Yoreo *et al.* [40]:

$$\lambda = 19 r_c + P \; . \tag{2.10}$$

For a hollow core the length of the perimeter is $P = 2\pi r_{hc}$, in which the crater region is included in r_{hc}. Using measured values of $r_{hc} \approx 150$ nm we now come to step spacings of about 1 μm, which is the right order of magnitude.

2.4.2 Kinetics

The propagation velocity of a step v_{step} is determined by the kink length w, the kink density (number of kinks per step site) n_k, and the effective addition frequency of growth units into a kink position, v_{eff} [38, 41, 42]:

$$v_{step} = n_k \cdot w \cdot \nu_{eff} \; . \tag{2.11}$$

The effective addition frequency is the difference between the addition frequency and the removal frequency of growth units to and from a kink site: $\nu_{eff} = \nu_{add} - \nu_{rem}$. The addition frequency is given by:

$$\begin{aligned} \nu_{add} &= \chi \, S \, \nu_o \\ &= \chi_{eq} \, \exp^{\Delta\mu/kT} S \, \nu_o \; , \end{aligned} \tag{2.12}$$

in which χ is the volume fraction of growth units (instead of concentration, as the protein growth units are much larger than the solvent molecules). ν_0 is the number of times per second a growth unit adjacent to a kink attempts to stick to this position. S is the sticking fraction, i.e. the chance that such an attempt is successful. The removal frequency is assumed to be independent of supersaturation.

At equilibrium ($\Delta\mu = 0$), the removal frequency is equal to the addition frequency:

$$\nu_{rem} = \chi_{eq} \, \exp^{0/kT} S \, \nu_o \; . \tag{2.13}$$

Thus, the effective addition frequency becomes

$$\begin{aligned} \nu_{eff} &= \chi_{eq} \, S \, \nu_o \left[\exp^{\Delta\mu/kT} - 1 \right] \tag{2.14} \\ &= \chi_{eq} \, S \, \nu_o \, \sigma \; , \tag{2.15} \end{aligned}$$

in which σ is the relative supersaturation defined by $\frac{\chi - \chi_{eq}}{\chi_{eq}} \cong \frac{c - c_{eq}}{c_{eq}}$.

The time for a lysozyme molecule to displace over a distance $d \approx (\bar{d^2})^{1/2}$ in its solution is given by $t = \frac{\bar{d^2}}{6D}$, with D the diffusion constant [43]. Since addition to a kink site proceeds by a "jump" downwards over the step height, h, and movement upwards and in the horizontal directions does not play a role, it follows that

$$\nu_o \cong (6t)^{-1} \cong \frac{D}{h^2} \; . \tag{2.16}$$

Substituting 2.15 and 2.16 into 2.11 we find for the step speed

$$v_{step} = n_k \, w \, \chi_{eq} \, S \, \frac{D}{h^2} \, \sigma \; . \tag{2.17}$$

So, the sticking fraction S becomes

$$S \;\; = \;\; \frac{v_{step} \, h^2}{n_k \, w \, \chi_{eq} \, D \, \sigma} \tag{2.18}$$

$$= \;\; \frac{\beta \, h^2}{n_k \, w \, \chi_{eq} \, D} \; , \tag{2.19}$$

in which β is the kinetic coefficient. β is 2.9 nm/s as determined by experiment (see section 2.3.2). The kink density n_k is about 0.5, as the steps in our experiments are rounded. By approximating the HEWL molecule by a cube of 3 by 3 nm we take the step height h and kink length w to be 3 nm. The equilibrium volume fraction of lysozyme χ_{eq} is approximately 4×10^{-4}. From literature we take an averaged value of the diffusion coefficient for lysozyme in a 0.05 M NaAc buffer and NaCl as precipitating agent, which is 1.2×10^{-10} $m^2 \, s^{-1}$ [44, 45]. Thus, we find a sticking fraction S of 4×10^{-4} for triclinic lysozyme. For [100] steps on (010) orthorhombic lysozyme the sticking fraction was found to be in the order of 10^{-6} [9]. The kink sites of the orthorhombic crystals are made up of four molecules, which results in four different sticking fractions for the individual molecules. Some of the additions are less favourable than others, leading to a lower average S than in the case of our triclinic crystals with only one molecule per kink site. Also, orthorhombic lysozyme is grown from a chloride solution in stead of a nitrate solution. Kink kinetics and pre-kink orientation requirements may therefore differ significantly.

2.5 Conclusions

The observed morphology of triclinic HEWL crystals grown for *in-situ* AFM measurements on the (001) face is in agreement with the morphology derived from the connected net analysis using the macrobond concept by Matsuura and Chernov[15]. AFM images show rounded steps, single and multiple growth spirals with large anisotropy, hollow cores and step bunching.

The main step sources are the growth spirals, although 3D nucleation was also observed. Step patterns indicate the occurrence of impurity pinning. However, steps are not blocked completely by the impurities. Both screw and edge dislocations are marked by hollow core outcrops at the surface. But the radii of the hollow cores are one order of magnitude larger than theoretical values, which is explained by their trumpet shaped emergence at the surface. The velocity of the steps is proportional to the relative supersaturation. From morphology and the experimentally determined kinetic coefficient we find a sticking fraction $S = 4 \times 10^{-4}$ for a protein molecule to become attached to a kink site, which is significantly different compared to the sticking fraction for orthorhombic lysozyme. From the rounded shape of the spirals and the absence of 2D nucleation we conclude that the step free energy must be in the range $1.3 < \gamma_m/kT < 3$, which is comparable to values of tetragonal lysozyme.

Acknowledgements

The authors would like to thank prof. W.J. de Grip of the Nijmegen Center for Molecular Life Sciences for stimulating discussions on protein crystal growth.

Appendix A: Inverse Wulff construction applied to growth spirals

The inverse Wulff construction is used to obtain a polar plot of step velocity versus step orientation from spiral shapes imaged by AFM. In this an ellipse is used as an approximation of the more or less elliptically shaped growth spirals.

For an ellipse with the centre at (0,0) we can write the following expression:

$$\frac{x^2}{k^2} + \frac{y^2}{(k-1)^2} = p^2 \; , \tag{A.1}$$

in which, k and p are constants defining the ellipse. Equation A.1 can be rewritten as a function $f(x)$

$$f(x) = \pm(k-1)\sqrt{p^2 - \frac{x^2}{k^2}} \; , \tag{A.2}$$

in which the $\pm$ indicates the top and bottom sides of the ellipse. The first step in performing the inverse Wulff construction is to find the tangent for every point of the ellipse. Then, we draw a line perpendicular to the tangent. This line should run through the so-called growth centre, which is the dislocation outcrop for a spiral (see figure A.1). The growth centre can be any point within the ellipse.
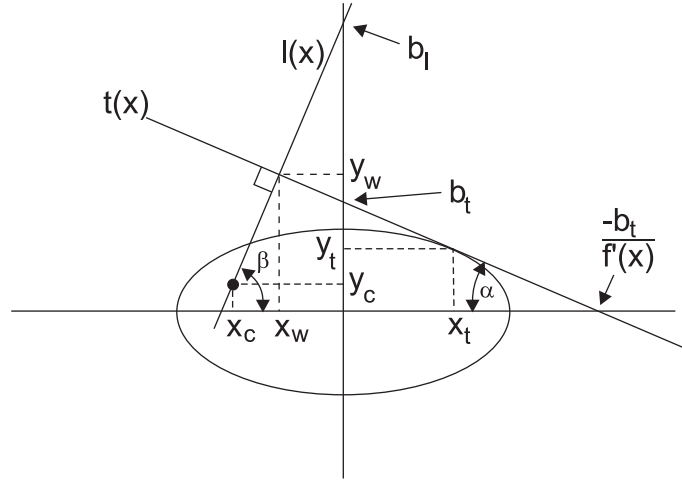
Figure A.1: Principle of the inverse Wulff construction starting from an elliptical spiral shape.

Thus, the first step is to find the tangent in every point of the ellipse. The derivative of $f(x)$

$$f'(x) = \pm\frac{(1-k)}{k^2}\frac{x}{\sqrt{p^2 - \frac{x^2}{k^2}}} \; , \tag{A.3}$$

gives the direction of the tangent for all points on the ellipse. As one can see, for $x = pk$ this results in a division by zero, i.e. a vertical line. The tangent $t(x)$ can be written as

$$t(x) = f'(x_t)\, x + b_t \ , \tag{A.4}$$

in which $f'(x_t)$ is the derivative of the ellipse, and thus the slope of the tangent line, in point x_t of the ellipse, and b_t is the intersection of the tangent with the vertical y-axis. In the point where the tangent touches the ellipse, at (x_t, y_t) (see figure A.1), we find that $f(x_t) = t(x_t)$. We can use this fact to find a value for b_t:

$$b_t = f(x_t) - f'(x_t)\, x_t \ . \tag{A.5}$$

Next step is to define the line perpendicular to $t(x)$ that passes through the growth centre (x_c, y_c). For this perpendicular line $l(x)$ we can derive:

$$\begin{aligned} l(x) &= a_l x + b_l \\ &= x \tan \beta + b_l \ , \end{aligned} \tag{A.6}$$

in which $\beta = (\frac{1}{2}\pi - \alpha)$ as defined in figure A.1. In the resulting equation b_l is unknown. Since $\beta = \frac{1}{2}\pi + \arctan[f'(x_t)]$ we can write for b_l

$$\begin{aligned} b_l &= y_c - x_c \tan \beta \tag{A.7} \\ &= y_c - x_c \tan\left(\frac{1}{2}\pi + \arctan\left(f'(x_t)\right)\right) . \tag{A.8} \end{aligned}$$

Now we can find the intersection point of the tangent and the perpendicular line, which is the point (X_W, Y_W) on the Wulff plot corresponding to the point (x_t, y_t) on the ellipse. This is the point where $t(X_W) = l(X_W)$:

$$\begin{aligned} f'(x_t)\, X_W + b_t &= X_W \tan \beta + b_l \tag{A.9} \\ (f'(x_t) - \tan \beta) X_W &= b_l - b_t \tag{A.10} \\ X_W &= \frac{(b_l - b_t)}{f'(x_t) - \tan \beta} \ . \tag{A.11} \end{aligned}$$

By substituting X_W in either equation A.4 or A.6 we find Y_W

$$Y_W = \frac{(b_l - b_t) \tan \beta}{f'(x_t) - \tan \beta} + b_l \ .$$
(A.12)

The complete set of points (X_W, Y_W) represents the polar Wulff plot, which relates step velocity to step orientation.

References

[1] McPherson, A. *Crystallization of Biological Macromolecules;* Cold Spring Harbor Laboratory Press: New York, 1999.

[2] Ries-Kautt, M.; Ducruix, A. F. *J. Biol. Chem.* **1989,** *264,* 745-748.

[3] Vaney, M.; Broutin, I.; Retailleau, P.; Douangamath, A.; Lafont, S.; Hamiaux, C.; Prange, T.; Ducruix, A.; Ries-Kautt, M. *Acta Crystallogr., Sect. D* **2001,** *57,* 9229-9240.

[4] Steinrauf, L. *Acta Crystallogr.* **1959,** *12,* 77-79.

[5] Legrand, L.; Ries-Kautt, M.; Robert, M. *Acta Crystallogr., Sect. D* **2002,** *58,* 1564-1567.

[6] Durbin, S.; Carlson, W. *J. Cryst. Growth* **1992,** *122,* 71-79.

[7] Gorti, S.; Forsythe, E.; Pusey, M. *Cryst. Growth Des.* **2005,** *5,* 473-482.

[8] Rashkovich, L.; Gvozdev, N.; Sil'nikova, M.; Chernov, A. *Crystallogr. Rep.* **2002,** *47,* 859-866.

[9] Chernov, A.; Rashkovich, L.; Yaminski, I.; Gvozdev, N. *J. Phys.: Condens. Matter* **1999,** *11,* 9969-9984.

[10] Kossel, W. *Angew. Chem.* **1952,** *64,* 276.

[11] Walsh, M.; Schneider, T.; Sieker, L.; Dauter, Z.; Lamzin, V.; Wilson, K. *Acta Crystallogr., Sect. D* **1998,** *54,* 522-546.

[12] Aune, K.; Tanford, C. *Biochemistry* **1969,** *8,* 4579-4585.

[13] Boerrigter, S.; Grimbergen, R.; Meekes, H. 2001 Facelift-2.50, a program for connected net analysis, Dept. of Solid State Chemistry, Radboud University of Nijmegen; email: H.Meekes@science.ru.nl.

[14] Bennema, P. . In *Handbook of Crystal Growth*, Vol. 1a; North-Holland: 1993; Chapter 7.

[15] Matsuura, Y.; Chernov, A. *Acta Crystallogr., Sect. D* **2003,** *59,* 1347-1356.

[16] Kuznetsov, Y.; A.J. Malkin, A. M. *J. Cryst. Growth* **1999,** *196,* 489-502.

[17] Waizumi, K.; Plomp, M.; van Enckevort, W. *Colloids Surf., B* **2003,** *1-2,* 73-86.

[18] Wulff, G. *Z. Kristallogr. Miner.* **1901,** *34,* 449-530.

[19] Wilson, H. *Philos. Mag.* **1900,** *50,* 238.

[20] Frenkel, J. *Phys. Z. Sowjetunion* **1933,** *1,* 498.

[21] Plomp, M.; A. McPherson, A. M. *Proteins: Struct., Funct., Genet.* **2003,** *50,* 486-495.

[22] Nakada, T.; Sazaki, G.; Miyashita, S.; Durbin, S.; Komatsu, H. *J. Cryst. Growth* **1999,** *196,* 503-510.

[23] Durbin, S.; Feher, G. *J. Cryst. Growth* **1986,** *76,* 583-592.

[24] Chernov, A. *Phys. Rep.* **1997,** *288,* 61-75.

[25] Fiddis, R.; Longman, R.; Calvert, P. *J. Chem. Soc.* **1979,** *75,* 2753.

[26] Land, T.; Martin, T.; Potapenko, S.; Palmore, G.; Yoreo, J. D. *Nature* **1999,** *399,* 442-445.

[27] Land, T.; Malkin, A.; Kuznetsov, Y.; McPherson, A.; De Yoreo, J. *Phys. Rev. Lett.* **1995,** *75,* 2774-2777.

[28] Wang, S.; Li, G.; Xiang, Y.; Huang, R.; Zhang, Y.; Wang, D. *Acta Crystallogr., Sect. D* **2005,** *61,* 826-831.

[29] Frank, F. *Acta Crystallogr.* **1951,** *4,* 497-501.

[30] Cabrera, N.; Levine, M. *Philos. Mag.* **1956,** *1,* 450-458.

[31] van der Hoek, B.; van der Eerden, J.; Bennema, P. *J. Cryst. Growth* **1982,** *56,* 621-632.

[32] van der Hoek, B.; van der Eerden, J.; Bennema, P. *J. Cryst. Growth* **1982,** *56,* 108-124.

[33] Vekilov, P.; Chernov, A. *Solid State Physics* **2002,** *57,* 1-147.

[34] Srolovitz, D.; Safran, S. *Philos. Mag., Sect. A* **1985,** *52,* 793-800.

[35] Qian, W.; Rohrer, G.; Skowronski, M.; Doverspike, K.; Rowland, L.; Gaskill, D. *Appl. Phys. Lett.* **1995,** *67,* 2284-2286.

[36] Liu, G.; van der Eerden, J.; Bennema, P. *J. Cryst. Growth* **1982,** *58,* 152-162.

[37] van Enckevort, W. . In *Facets of 40 years of crystal growth. A tribute to Piet Bennema on the occasion of his retirement*; IMM department of Solid State Chemistry, Radboud University Nijmegen: 1997.

[38] Burton, W.; Cabrera, N.; Frank, F. *Philos. Trans. R. Soc. London, A* **1951,** *243,* 299-358.

[39] Liu, X.; Bennema, P. *J. Chem. Phys.* **1993,** *98,* 5863-5872.

[40] DeYoreo, J.; Land, T.; Rashkovich, L.; Onischenko, T.; Lee, J.; Monovskii, O.; Zaitseva, N. *J. Cryst. Growth* **1997,** *182,* 442-460.

[41] van der Eerden, J. . In *Handbook of Crystal Growth*, Vol. 1a; North-Holland: 1993; Chapter 5, page 307.

[42] Cuppen, H.; Meekes, H.; van Veenendaal, E.; van Enckevort, W.; Bennema, P.; Reedijk, M.; Arsic, J.; Vlieg, E. *Surf. Sci.* **2002,** *506,* 183-195.

[43] Moore, J.; Pearson, R. *Kinetics and mechanisms;* John Wiley & Sons: 3 ed.; 1981.

[44] Muschol, M.; Rosenberger, F. *J. Chem. Phys.* **1995,** *103,* 10424-10432.

[45] Kim, Y.; Myerson, A. *J. Cryst. Growth* **1994,** *143,* 79-85.

Chapter 3

Growth inhibition of protein crystals:
A study of lysozyme polymorphs

Crystal morphology is determined by the relative growth rates of the different faces involved. Opposite faces (hkl) and $(\bar{h}\bar{k}\bar{l})$ can show different rates if the crystal structure does not have inversion symmetry. Protein crystals, being built of asymmetric molecules do not have identical opposite faces, except for those pairs linked by rotational symmetry. Here, we present an in-situ microscopy study on the polar growth of various polymorphs of hen egg-white lysozyme crystals. It was found that in a number of cases the growth of one of the two faces was blocked, whereas the opposite one was not slowed down. To explain our results we propose a self-poisoning mechanism based on solvent-induced adsorption of misorientated lysozyme molecules on the inhibited faces. This mechanism can also prevent some proteins from forming crystals at all.

3.1   Introduction

X-ray diffraction remains the most important method to solve the 3D structure of biological macromolecules. The success of this method depends on whether protein crystals can be grown and if so, on their quality. To understand the factors responsible for this, knowledge of the mechanisms involving the formation of protein crystals is important. A model system for investigations into protein crystal growth mechanisms is the enzyme hen egg-white lysozyme (HEWL). Like many proteins[1], this protein can crystallise in various crystal structures depending on the crystallising agent and temperature, a phenomenon called polymorphism*. Lysozyme crystals grown from a sodium chloride solution have either the well-known tetragonal $P4_32_12$ structure or the orthorhombic $P2_12_12_1$ structure (at higher temperatures), while crystals grown from a sodium thiocyanate solution are monoclinic $P2_1$. HEWL crystals growing in a sodium nitrate solution can either turn out as monoclinic $P2_1$ or triclinic $P1$ (fig. 3.1). The difference in crystal structure also shows up

Figure 3.1: Monoclinic and triclinic HEWL crystals coexisting in a HEWL/ NaNO$_3$ / NaOAc / HOAc solution.

---

*The various possible crystal structures of lysozyme are not polymorphs in the strictest sense of the word, because the salts are incorporated in the crystal and thus induce different compositions

in the crystal morphology, or outer shape, of the crystals. An often observed feature of the monoclinic polymorph of lysozyme is an asymmetry in the crystal habit between the two opposite top faces of the rod shaped crystals (see figure 3.1 and refs. [2–5]).

A polar morphology, i.e. a crystal habit lacking inversion symmetry, is the result of opposite faces (hkl) and $(\bar{h}\bar{k}\bar{l})$ growing at a different rate, called polar growth, or unidirectional growth. A classical example is the growth of α-resorcinol, which shows polar growth from solution as well as from the vapour phase[6, 7]. A prerequisite for polar growth is a crystal structure in which the pair of opposite faces are not related by a symmetry operator of the crystal's point group. Typically, this is likely to occur for molecules which do not have inversion symmetry, like α-resorcinol and also proteins which, being build of only left-handed amino-acids, by definition do not have inversion symmetry. The Hartman-Perdok theory[11], relating growth rate to attachment energy, does not provide for difference in growth rates of opposite faces. Explanations can be found in surface-solvent interactions[8], presence of impurities[9, 10], and self-poisoning mechanisms[12].

Here we present a study on the formation of polar morphologies in protein crystal growth. By using optical microscopy, we compare growth rates of opposite crystal faces for the tetragonal, monoclinic and triclinic form of hen egg-white lysozyme crystals. Based on our experiments and literature data on lysozyme anion binding sites we propose a self-poisoning mechanism by misoriented lysozyme molecules adsorbed on one of the opposite polar surfaces, which leads to a reduction or complete arrest of its growth. A complete blocking of opposite faces offers a possible explanation for the fact that some proteins do not form crystals at all.

3.2   Experimental methods

Chemicals of analytical grade were used in this study. A buffer stock solution of sodium acetate and acetic acid was made in deionised water (>15 MΩcm) to result in a 0.05 M NaOAc/HOAc solution of pH 4.5. HEWL from Sigma-

Aldrich (lot nr. 094K1454) was used as source material for crystal growth after purification by dialysis (MWCO 8 kDa) in buffer solution. NaCl, NaNO$_3$ and NaSCN stock solutions were also prepared in buffer solution. Lysozyme, salt and buffer solutions were filtered over a 0.2 μm membrane (Schleicher & Schuell), and mixed with each other in the appropriate proportions just prior to the growth experiments. For experiments on the effects of impurities ultrapure lysozyme (99.99%, Mol Logics Inc., Japan) was used without further treatment in filtered buffer and salt solutions.

Growth solutions were inserted in a cell consisting of an X-ring in between two microscope cover glasses and sealed by vacuum grease to prevent evaporation. The internal dimensions of the growth cell are a radius of 7 mm and a height of 1.8 mm, comprising a volume of 270 μl. Crystals were either nucleated in the cell or seeded into it. For the experiment, the growth cell was placed on a temperature-controlled stage with a hole of 6 mm in diameter to allow for transmission optical microscopy, while stabilising the temperature within a 0.3 ^{o}C margin.

Images were acquired by in-situ optical transmission microscopy in combination with a CCD camera. A combination of image processing software (ImagePro Plus [13]) and Matlab[14] was used to determine crystal side face displacement from the images. Using a macro in ImagePro Plus, image intensity line profiles perpendicular to the edges of the crystal top face, which correspond to the crystal side faces of interest, were taken from subsequent micrographs. In the intensity profiles these crystal surfaces show up as a sharp decrease in intensity with respect to the bright background. A script in Matlab is used to detect these decreases automatically for the series of line profiles, and thus the position of the surfaces with respect to the fixed image frame of the image as function of time.

3.3 Results & Discussion
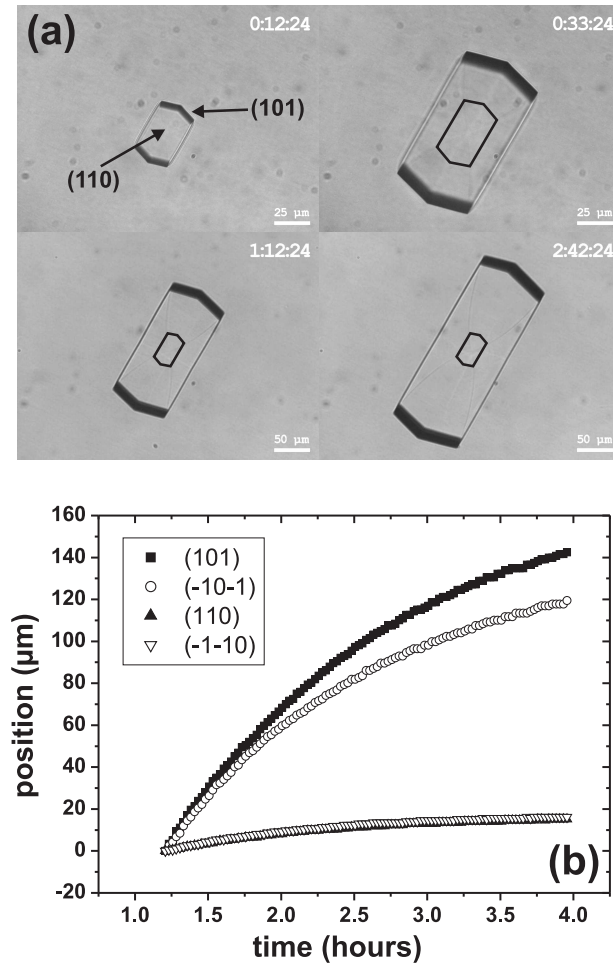
3.3.1 Tetragonal lysozyme

Figure 3.2a shows a tetragonal lysozyme crystal growing from a 40 mg/ml HEWL, 0.685 M NaCl[†], 0.05 M NaOAc/HOAc solution at 21 ^{o}C. The crystal is viewed upon one of its {110} faces, with the c-axis parallel to the longer crystal direction. The aspect ratio of tetragonal lysozyme crystals changes with supersaturation[15], changing from plate-like at high to elongated crystals at low supersaturation. Curved lines inside the crystal are just visible, which indicate the different growth sectors of the crystal[4]. The point group of the tetragonal crystal structure of HEWL is 422. Because this point group has a four-fold axis along the c-axis and two-fold axes along the a- and b-axis, the four {110} faces are symmetrically equivalent as well as the eight {101} faces. As a result, the crystal growth rates are equal in opposite {110} directions (fig. 3.2b) and nearly equal in opposite {101} directions. The slight difference in the latter case is due to the presence of crystals outside the field of view influencing the nutrient supply to one of the two {101} faces. A difference in the number of dislocations outcropping at the surface may also account for this difference.

3.3.2 Monoclinic lysozyme

Monoclinic lysozyme crystals can be grown from sodium nitrate solutions and sodium thiocyanate solutions. Literature shows a slight difference in cell parameters for these two lysozyme-salt complexes (e.g. Protein Data Bank[16] entries 1HF4, using $NaNO_3$, and 1LCN, using NaSCN), as do the morphologies of the crystals (figs. 3.3a and b). In both cases the point group symmetry is 2. Figure 3.3a shows a series of images of a monoclinic lysozyme crystal growing in a 15 mg/ml HEWL, 0.2 M $NaNO_3$ 0.05 M NaOAc/HOAc solution at 20 ^{o}C. The crystal shows the typical polar morphology of the monoclinic polymorph. In the positive b-direction, as determined by Hondoh et al.[2], the (010) face is properly faceted. In the opposite direction the crystal has

---

[†]0.685 M NaCl = 4% w/v NaCl.

Figure 3.2: (a) Series of optical time-lapse images of a tetragonal lysozyme crystal growing in a 40 mg/ml HEWL, 4% w/v NaCl, 0.05 M NaOAc/HOAc solution of pH 4.5 at 21ºC. Note that in the first two pictures the scale bar indicates 25 μm, and in the last two it indicates 50 μm. The crystal size of the first picture is represented in the other pictures by black lines. (b) Crystal surface position of the {110} and {101} surfaces of the crystal in (a). Zero indicates the position of the surfaces in the first image of the series.

a rounded surface which does not show any growth. As this rounded surface does not grow it is not kinetically roughened as suggested by Ref. [2], but it is round as a result of growth blockage over a range of directions containing a negative b component. Since the average orientation is $[0\bar{1}0]$, we shall indicate this set of faces $(h\bar{k}l)$ as $(0\bar{1}0)$.

Similar to the monoclinic NaNO$_3$-lysozyme crystal, the NaSCN-lysozyme crystal exhibits polar growth along the b-axis. Figure 3.3b shows a series of images of a monoclinic HEWL crystal growing in a 10 mg/ml HEWL, 0.1 M NaSCN, 0.05 M NaOAc/HOAc solution with the ultra-pure lysozyme, at 18 ^{o}C. We assume the similarity in crystal structure and morphology also to hold for the orientation of the polar faces of the thiocyanate-grown monoclinic polymorph, and thus identify the blocked and rounded face to be -on the average- the $(0\bar{1}0)$ face. New crystals preferably nucleate and grow out at this side. In comparison to the experiment with NaNO$_3$, the NaSCN solution has a higher supersaturation ($\Delta\mu/kT = 1.1$ versus $\Delta\mu/kT = 0.76$, with $\Delta\mu/kT = \ln(c/c_{\mathrm{eq}})$) and both the (010) and the side faces grow faster. Figure 3.4 shows the crystal surface position for the crystals in the thiocyanate and the nitrate experiments. The side faces show little asymmetry, while the (010) and $(0\bar{1}0)$ faces show one to two orders of magnitude difference in growth rate. This agrees with the point group 2 of the crystals for which the side faces $(h0l)$ and $\bar{h}0\bar{l})$ are symmetrically equivalent, in contrast to the opposite (010) and $(0\bar{1}0)$ pair. Experiments using lysozyme from Sigma, less pure than that used for the experiment shown in figure 3.3b, gave similar results. From this, we conclude that heterogeneous impurities cannot be responsible for the polar growth of monoclinic HEWL crystals.

3.3.3   Triclinic lysozyme

The triclinic polymorph of the lysozyme-nitrate system can be grown by first inducing nucleation of both the triclinic and the monoclinic polymorph by lowering the temperature. After a raise in temperature the monoclinic polymorph will dissolve while the stable triclinic polymorph remains[17, 18]. A triclinic lysozyme crystal was removed from the solution and seeded into a fresh growth
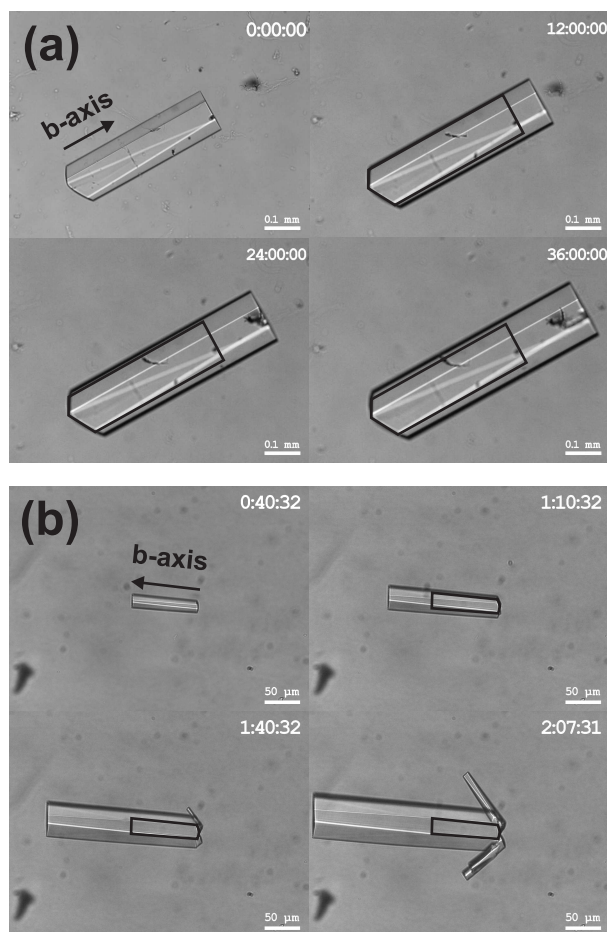
Figure 3.3: (a) Series of optical time-lapse images of a monoclinic lysozyme crystal growing in a 15 mg/ml HEWL, 0.2 M NaNO$_3$ 0.05 M NaOAc/HOAc solution of pH 4.5 at 20 $^o C$. The black lines are a guide to the eye indicating the size of the crystal in the first image of the series. Time indicated in the upper right corners is in hours. (b) Series of optical time-lapse images of a monoclinic lysozyme crystal growing from in a 10 mg/ml HEWL, 0.1 M NaSCN, 0.05 M NaOAc/HOAc solution, at 18 ^{o}C, using ultra-pure lysozyme (99.99%). The black lines indicate the size of the crystal in the first image for comparison.
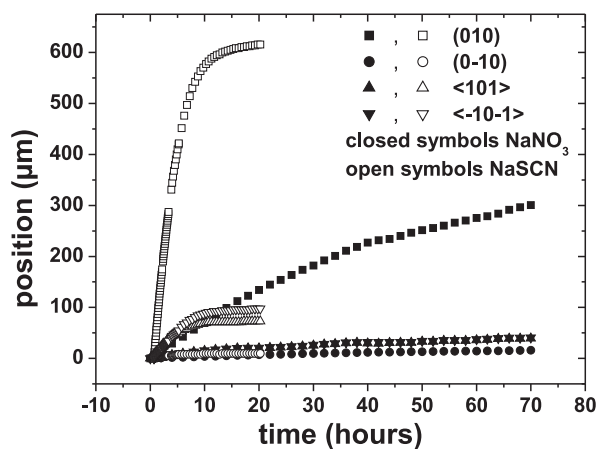
Figure 3.4: Crystal surface position for the (010) and the (0$\bar{1}$0) surfaces of the monoclinic crystals in figure 3.3a (closed symbols), and figure 3.3b (open symbols).

solution of 5 mg/ml HEWL, 0.2 M NaNO$_3$ and 0.05 M NaOAc/HOAc. Figure 3.5a shows a time-lapse series of micrographs of the triclinic crystal exhibiting polar growth at 20 ^{o}C, at a supersaturation $\Delta\mu/kT$ of 1.1. Both directions of the crystal in the image plane show asymmetry in the growth rate (fig. 3.5b). The faces of one pair both show growth, the fastest about five times faster than the slowest; for the second pair one face is blocked in its growth. The growth rate of the third, out-of-plane direction cannot be determined from these images. In contrast to the polar surface of the monoclinic polymorph, all polar faces are properly faceted. New crystals often nucleate at the blocked face, which is similar to the monoclinic crystals grown from the NaSCN solutions.

3.3.4 Comparing lysozyme polymorphs

Polar growth, i.e. a difference in growth of opposite faces (hkl) never occurs if the point group of the crystal is centrosymmetric. Proteins are chiral growth units, so the crystal structure of these macromolecules will never contain an inversion centre or a (glide) mirror plane. So, protein crystals are prone to
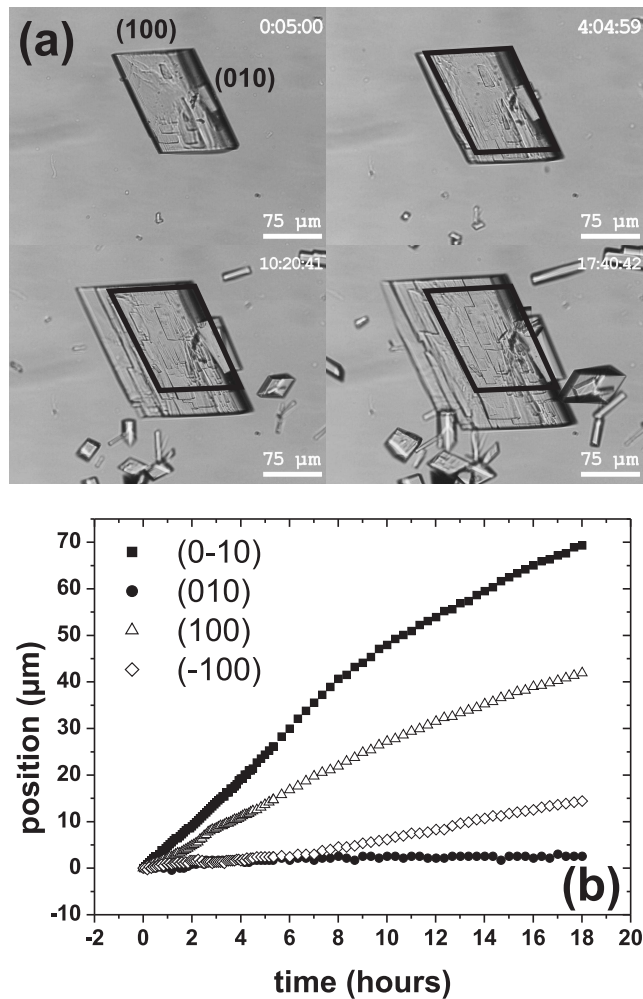
Figure 3.5: Series of optical time-lapse images of a triclinic lysozyme crystal growing in a 5 mg/ml HEWL, 0.2 M NaNO$_3$ and 0.05 M NaOAc/HOAc solution of pH 4.5 at 20 ^{o}C. The black lines in subsequent figures indicate the crystal size of the first image. The crystal exhibits polar growth in two crystallographic directions. Time indicated in the upper right corner is in hours. (b) Crystal surface position for the crystal in (a) showing quantitatively the polar growth of the {100} and {010} faces.

polar growth. For point groups with high symmetry it is more likely that opposite faces are linked by symmetry. For tetragonal lysozyme crystals with point group 422 the opposite faces of the forms {101} and {110}, which determine the morphology of the crystals, are symmetrically equivalent. Therefore, no polar growth is expected to occur, as is observed. For the monoclinic crystals with point group 2 only the side face pairs $(h0l)$ and $(\bar{h}0\bar{l})$ are related by symmetry. The top faces (010) and $(0\bar{1}0)$ are different, which leads to the observed polar growth along the b-axis. The point group of the triclinic crystals is 1, that is, they lack symmetry and all possible pairs of opposite faces (hkl) and $(\bar{h}\bar{k}\bar{l})$ are not symmetry related. Here polar growth can occur for all directions.

Often, an asymmetry in growth rate is caused by the presence of impurities in the solution. If these impurities preferably adsorb onto a specific crystal surface[9], this surface is slowed down or blocked for further growth[19]. In both "normal" and extra-pure solutions, the monoclinic polymorph grown from NaSCN solutions showed a growing (010) and a stationary $(0\bar{1}0)$ face. From this, we conclude that the presence of impurities are not a prerequisite for polar growth of lysozyme crystals.

The correlation between space group and number of polar growth directions suggest that the polar growth is an intrinsic property of the crystal structure. When we regard the interactions between lysozyme molecules using the macrobond concept as introduced by Hondoh et al.[2] and Matsuura et al.[20] there is no difference in a bond from a molecule A to a molecule B and vice versa. Thus, these bonds do not force a preferential direction for growth and also do not include solvent effects. Therefore, polar growth can not be explained from a simple point of view, only considering bulk bonds between adjacent growth units in the crystal.

The origin of the polar growth may be found in the interactions of the crystal surface with the solvent or with lysozyme molecules in the solvent. For crystals of small organic molecules, interactions with the solvent can result in a surface-bound layer of solvent molecules which prohibit the attachment of the crystal growth units[10, 21]. For proteins, the size difference between

the growth units and the solvent molecules, water molecules and ions, is very large, and it does not seem feasible that these block the attachment of a protein molecule. Experiment shows that for the monoclinic case polar growth is independent of the choice of the anion (i.e. NO_3^- or SCN^-). In fact, the presence of water or ions is even necessary to form a crystalline contact between molecules[22]. However, the solvent molecules can change the surface charge distribution by binding to the lysozyme molecule, and as such change the characteristics of the crystal surface.

For polar growth to occur the molecular structure of the opposite (hkl) and $(\bar{h}\bar{k}\bar{l})$ surfaces must differ. Figure 3.6a shows the orientation of the lysozyme molecule in the (001) and $(00\bar{1})$ surfaces of the triclinic polymorph, with the basic residues depicted in light grey and the acidic residues in dark grey. All directions show a different local composition of basic and acidic residues. These residues lead to a difference in charge density distribution over the molecule surface, which again leads to a difference in water and anion binding. Since these bindings form the interactions between the different molecules in the crystals a difference in growth rate in opposite directions seems feasible. The same conclusion can be drawn for the monoclinic polymorphs. Figure 3.6b shows a different local composition of residues for the (010) and $(0\bar{1}0)$ surfaces, but the other faces $(h0l)$ and $(\bar{h}0\bar{l})$ are identical.

No detectable growth was observed for the $[0\bar{1}0]$ directions of the monoclinic crystals as well as for one of the (010) faces of the triclinic crystals. Since impurities and small molecules can not explain this arrest in growth, we suggest that blocking is caused by wrongly oriented protein molecules covering the surface. It is expected that protein molecules adsorbed on the crystal surface can have several orientations, different from the correct one, which are still energetically favourable. If the surface is covered by a large number or a complete layer of such misoriented HEWL molecules, then no new layers can develop on top of it and crystal growth is blocked. A similar self-poisoning of crystal growth has also been proposed to explain the polar growth of the steroid crystal 7αMNa[12]. A self-poisoning mechanism due to misorientated protein molecules on the crystal surfaces may also explain the difficulty in
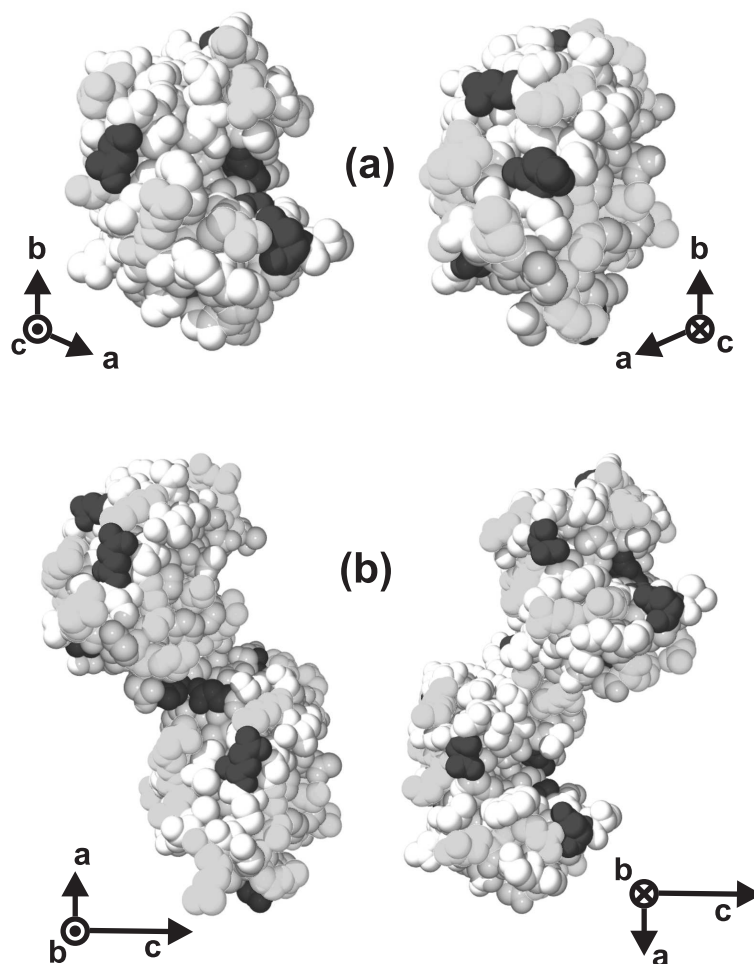
Figure 3.6: (a) Schematic representation of a hen egg-white lysozyme molecule viewed upon as if in the triclinic (001) (left) and (00$\bar{1}$) (right) surfaces. For this image structural data taken from the Protein Data Bank[16] (code 4LZT) was used. Dark grey colored atoms indicate acidic residues and light grey colored atoms indicate basic residues. (b) Schematic representation of the two lysozyme molecules in the asymmetric unit of the monoclinic structure, viewed upon its (010) face (left) and (0$\bar{1}$0) face (right), (PDB code 1HF4).

Figure 3.7: Clusters of monoclinic crystals in a 10 mg/ml, 0.1 M NaSCN, 0.05 M NaOAc/HOAc solution of pH 4.5 at 15 ^{o}C. The large crystal was seeded into the solution. The scale bar indicates 50 μm.

crystallisation of many proteins, because when the opposite faces are both blocked, growth of the crystal cannot occur.

Secondary nucleation often occurs at the rounded, blocked side of the monoclinic crystals grown from thiocyanate solutions. The formation of secondary crystallites was also encountered on the blocked (010) face of the triclinic crystals. This nucleation is partly the result of a higher supersaturation as the crystal does not grow and so does not lower the solute concentration at the blocked side. Further, in contrast to the growing parts of the crystals, sub-micron crystallites sedimented onto the surface[23] are not grown-in and develop into larger sized crystals. In addition misoriented HEWL molecules on the (0$\bar{1}$ 0) faces of monoclinic crystals might stimulate secondary heterogeneous nucleation, which results in clusters of crystals with the $+\vec{b}$ direction pointing outward, as often observed experimentally (figure 3.7).

3.4 Conclusion

Growth rates of crystal surfaces (hkl) and their opposites $(\bar{h}\bar{k}\bar{l})$ were investigated for four polymorphs of hen egg-white lysozyme. Crystals were found to grow polar in directions in which the opposite surfaces are not linked by symmetry operations. Therefore, the tetragonal $P4_32_12$ polymorph bounded by {110} and {101} faces cannot exhibit polar growth, whereas the monoclinic $P2_1$ structure can and does show polar growth along the b-axis for crystals grown from NaSCN and NaNO$_3$ solutions. The triclinic $P1$ polymorph, which does not have any symmetry related surfaces, showed polar growth in the two observable directions. For the monoclinic and triclinic crystals one of the polar faces is almost completely blocked in growth. Experiments using ultra-pure lysozyme showed that the presence of impurities is not a prerequisite for polar growth of lysozyme crystals. A simple view only considering bulk bonds between growth units can neither explain a polar morphology. We propose that self-poisoning induced by misoriented lysozyme molecules with an energetically favourable orientation on the crystal surface reduces or blocks growth and thus plays a major role in the polar growth of lysozyme crystals. Self-poisoning may also play an important role in the difficulties in crystallisation of many proteins, as crystal growth cannot occur if opposite faces both suffer from such a mechanism. The tuning of crystallisation conditions could then be viewed as the tuning of interactions to avoid self-poisoning.

Acknowledgements

References

[1] Carugo, O.; Argos, P. *Protein Science* **1997**, *6*, 2261-2263.

[2] Hondoh, H.; Sazaki, G.; Miyashita, S.; Durbin, S.; Nakajima, K.; Matsuura, Y. *Crystal Growth & Design* **2001,** *1,* 327-332.

[3] Jones, W.; Wiencek, J.; Darcy, P. *Journal of Crystal Growth* **2001,** *232,* 221-228.

[4] Vidal, O.; Robert, M.; Arnoux, B.; Capelle, B. *Journal of Crystal Growth* **1999,** *196,* 559-571.

[5] Rashkovich, L.; Gvozdev, N.; Sil'nikova, M.; Chernov, A. *Crystallography Reports* **2002,** *47,* 859-866.

[6] Weissbuch, I.; Leiserowitz, L.; Lahav, M. *Crystal Growth & Design* **2006,** *6,* 625-628.

[7] Srinivasan, K.; Sherwood, J. *Crystal Growth & Design* **2005,** *5,* 1359-1370.

[8] Bisker-Leib, V.; Doherty, M. *Crystal Growth & Design* **2001,** *1,* 455-461.

[9] Orme, C.; Noy, A.; Wierzbicki, A.; McBride, M.; Grantham, M.; Teng, H.; Dove, P.; DeYoreo, J. *Nature* **2001,** *411,* 775-779.

[10] Weissbuch, I.; Popovitz-Biro, R.; Lahav, M.; Leiserowitz, L. *Acta Crystallographica* **1995,** *B51,* 115-148.

[11] Hartman, P.; Perdok, W. *Acta Crystallographica* **1955,** *8,* 49-52.

[12] Stoica, C.; Tinnemans, P.; Meekes, H.; van Enckevort, W.; Vlieg, E. *Crystal Growth & Design* **2006,** *6,* 1311-1317.

[13] IMAGEPRO PLUS 4.5, MediaCybernetics.

[14] MATLAB 6.5 (Release 13), The MathWorks Inc.

[15] Durbin, S.; Feher, G. *Journal of Crystal Growth* **1991,** *110,* 41-51.

[16] Berman, H.; Westbrook, J.; Feng, Z.; Gilliland, G.; Bhat, T.; Weissig, H.; Shindyalov, I.; Bourne, P. *Nucleic Acids Research* **2000,** *28,* 235-242.

[17] Legrand, L.; Ries-Kautt, M.; Robert, M. *Acta Crystallographica* **2002,** *D58,* 1564-1567.

[18] Heijna, M.; van den Dungen, P.; van Enckevort, W.; Vlieg, E. *Crystal Growth & Design* **2006,** *6,* 1206-1213.

[19] Plomp, M.; McPherson, A.; Malkin, A. *Proteins* **2003,** *50,* 486-495.

[20] Matsuura, Y.; Chernov, A. *Acta Crystallographica* **2003,** *59,* 1347-1356.

[21] Stoica, C.; Verwer, P.; Meekes, H.; van Hoof, P.; Kaspersen, F.; Vlieg, E. *Crystal Growth & Design* **2004,** *4,* 765-768.

[22] Frey, M.; Genovesio-Taverne, J.; Fontecilla-Camps, J. *Journal of Physics D: Applied Physics* **1991,** *24,* 105-110.

[23] Kuznetsov, Y.; A.J. Malkin, A. M. *Journal of Crystal Growth* **1999,** *196,* 489-502.

Chapter 4

Spherulitic growth of hen egg-white lysozyme crystals

In protein crystallography spherulites are considered the result of a failed crystallisation experiment. Understanding the formation of these structures may contribute to finding methods to prevent their formation. Here we present an in-situ study on lysozyme spherulites grown from sodium nitrate and sodium thiocyanate solutions, investigating their morphology and growth kinetics using optical microscopy. In a morphodrom we indicate the conditions at which spherulites form for the lysozyme-nitrate system, showing that liquid-liquid phase separation is not a prerequisite to form sheave-like spherulites and that supersaturation is not the only factor determining their creation. Despite their sheave-like morphology the spherulites all appear to be formed through heterogeneous nucleation. The spherulites are of a new polymorphic form and are less stable than the monoclinic form. For a single needle growth kinetics indicate surface processes to be the rate limiting step during growth, but for an entire spherulite volume diffusion still plays a role. Spherulites simulated by using a time dependent tip splitting model are found to compare well to experimentally observed spherulites.

4.1   Introduction

X-ray diffraction (XRD) is the main route towards structure determination of protein macromolecules. The success of a structure determination by this method depends on the quality of the crystal. Trial-and-error methods are often used to find the proper crystallisation conditions for a specific protein. In this process of screening of protein crystallisation conditions most experiments do not yield XRD quality single crystals. Often the system does not exhibit crystal nucleation at all, or precipitates amorphously [1], depending on the degree of supersaturation of the system. In addition, proteins frequently precipitate in the form of spherulites [2, 3], also known as a "sea urchin" crystal morphology[4]. Spherulitic growth is a generic term for the formation of radial arrays of crystalline needles [5]. Although the term "spherulite" suggests an approximately spherical form, it is used in a broader sense for various forms of densely branched, polycrystalline solidification patterns [6] originating from a common initial nucleation point. It is also used as a term for radial patterns of fibres, for instance fibres formed by the gelling of the protein deoxyhemoglobin S [7]. In polymer science[5, 8], biomineralisation[9, 10] and mineralogy[11] spherulitic growth is an extensively studied phenomenon. For crystallisation from the melt, Keith and Padden[12] indicated the presence of static heterogeneities (e.g. impurities or polydispersity) to cause the non-crystallographic branching typical for the spherulitic growth form. On the other hand, spherulites found in pure liquids[13] indicate that the presence of impurities cannot be a general explanation of the spherulitic growth form. In the closely related phenomenon of the formation of nanocrystalline fibre networks, which may lead to the formation of spherulites[14, 15], the branching structure is formed by crystallographic mismatch branching[16–18]. This process has been studied in detail and is shown to be controlled by adding additives[16] or by changing supersaturation[17]. In protein crystal growth, spherulites are often observed (e.g. [19, 20]) but little attention has been offered to the mechanisms forming them.

In general, protein spherulites are discarded as a failure, since they do not yield usable XRD patterns. Understanding protein spherulite growth may

contribute to finding methods to prevent their formation. Hen egg-white lyso-zyme (HEWL) is often used as a model compound for understanding protein crystal growth in general, usually focusing on its tetragonal form obtained from sodium chloride solutions. Spherulitic growth of HEWL has been observed in liquid-liquid phase-separated lysozyme-chloride systems, and thus the formation of spherulites is thought to be a consequence of the presence of high-density phase droplets[3, 4]. Literature data indicate that spherulitic growth in these systems is controlled by surface kinetics[21].

In this paper we focus on spherulitic growth of HEWL in sodium nitrate and thiocyanate solutions, investigating in detail the morphology of individual spherulites. The objective is to improve the understanding of the formation and growth of protein spherulites.

4.2   Experimental procedures

Chemicals of analytical grade were used in this study. A buffer stock solution of sodium acetate and acetic acid was made in deionised water (>15 MΩcm) to result in a 0.05 M NaCH$_3$COO/HCH$_3$COO solution of pH 4.5. HEWL from Sigma-Aldrich (lot nr. 094K1454) was used as source material for crystal growth after purification by dialysis (MWCO 8 kDa) in buffer solution. NaNO$_3$ and NaSCN stock solutions were also prepared in buffer solution. Lysozyme, salt and buffer solutions were filtered over a 0.2 μm membrane (Schleicher & Schuell), and mixed with each other in the appropriate proportions just prior to the growth experiments.

A 1 μl droplet of the resulting mother liquor is placed between two microscope cover-slides, forming an approximately 10 μm thick layer, and is sealed off along the sides by immersion oil to prevent evaporation. Spherulites growing between two cover slides result in 2D objects, which are more suitable for imaging than 3D spherulites. The cover slides are placed, either in a temperature-controlled box for multiple, simultaneous experiments, or in a temperature controlled cell for in-situ optical microscopy. Experiments were performed at 18 ^{o}C with an accuracy of 0.1 ^{o}C and 0.5 ^{o}C respectively. The in-

situ cell consists of a brass plate through which water from a thermostatically controlled reservoir can flow. The cover slides are placed on top of the brass plate and are covered by another brass plate without water flow throughput. A 6 mm hole and a 15 mm hole at the centre of the bottom and top brass plate respectively allow for optical transmission microscopy.

Observations of the spherulites were made mainly by optical microscopy. Attempts to observe the crystal patterns by atomic force microscopy and cryo-scanning electron microscopy were not successful. A Zeiss Axioplan 2 microscope and an Olympus Vanox microscope were used, both suitable for polarisation microscopy. Higher magnification images were made using an Olympus oil immersion objective of 1.30 numerical aperture. To investigate the growth kinetics of the spherulites, series of images were recorded by time lapse CCD-photography. To determine the growth speed, the size of the spherulites in subsequent images was measured with the help of image processing software (Image-Pro Plus).

4.3   Results and discussions

4.3.1   Morphodrom

The typical morphology of 2D spherulites grown in $NaNO_3$ and NaSCN solutions is shown in figure 4.1. The conditions at which this type of structures form were investigated for the $NaNO_3$ system at 18 ^{o}C. The $NaNO_3$ concentration was varied between 0.2 M and 1 M, while the HEWL concentration ranged from 5 mg/ml up to 30 mg/ml. The presence or absence of spherulites and monoclinic crystals was verified by optical microscopy after growth in the temperature controlled box during several hours, typically needed for spherulites to form and reach their maximum size. Figure 4.2 shows the resulting morphodrom for this system, including the conditions at which liquid-liquid phase separation was observed. The solid line indicates the solubility of the monoclinic crystals as reported in literature[22]. Triclinic crystals, the stable
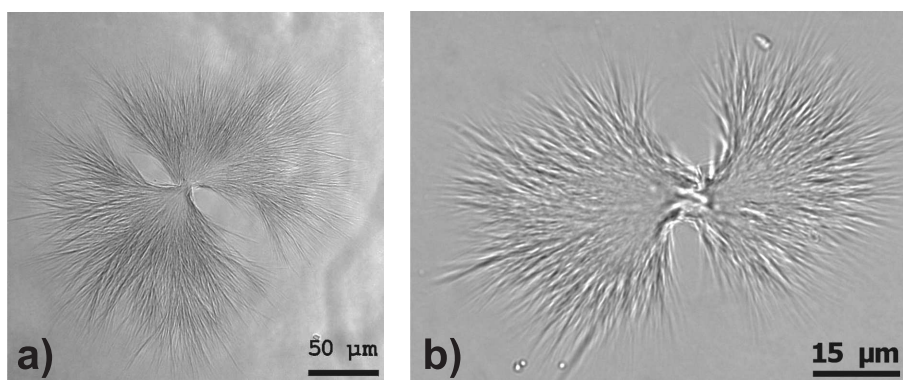
Figure 4.1: The morphology of two-dimensional HEWL spherulites grown at 18 ^{o}C in a 0.05 M sodium acetate buffer solution of pH 4.5 with a) 1 M NaNO$_3$, and b) 0.2 M NaSCN as crystallising agent, and 29 mg/ml HEWL.

polymorph* in this system and optically distinct from the monoclinic form by its crystal habit[23], were not found for these conditions.

Spherulites frequently coexist with monoclinic crystals, which in most cases appear before the spherulites do. When the temperature was raised to 28 ^{o}C, the spherulites dissolved, while the monoclinic crystals continued to grow (figure 4.3). Because the monoclinic crystals are metastable with respect to the triclinic polymorphs, the spherulites are thus a third, metastable, polymorph in the lysozyme-nitrate system. This observation does not follow Oswald's Rule of Stages, which postulates that the most metastable polymorph is the one to appear first[24]. Although powder diffraction on thick lysozyme needles is possible according to Ref. [25], in our case the needles were too thin for this method and the crystal structure of our spherulites remains unknown. From the morphodrom it follows that in order to avoid the formation of spherulites, it is better to choose a low NaNO$_3$ concentration and a high HEWL concentration than vice versa, although both mixtures can be chosen to be equally

---

*In principle, the various possible phases of the lysozyme in the nitrate system are not polymorphs in the strictest sense of the word, because their water and salt composition will vary somewhat.
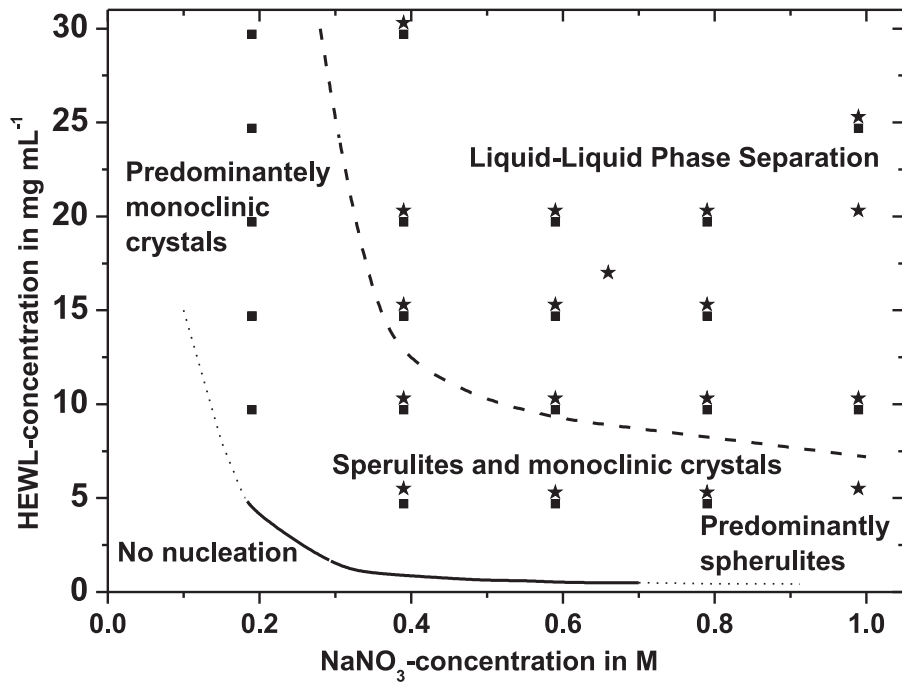
Figure 4.2: The morphodrom of the HEWL/NaNO$_3$/NaCH$_3$COO system at 18±0.5 ^{o}C and pH 4.5. Stars indicate the presence of spherulites, squares indicate the presence of monoclinic crystals. All experiments above the dashed line exhibit liquid-liquid phase separation. The solid line indicates the solubility of monoclinic HEWL, taken from literature [22], which is extrapolated to lower and higher NaNO$_3$ concentrations (dotted line) by assuming a normal solubility behaviour.
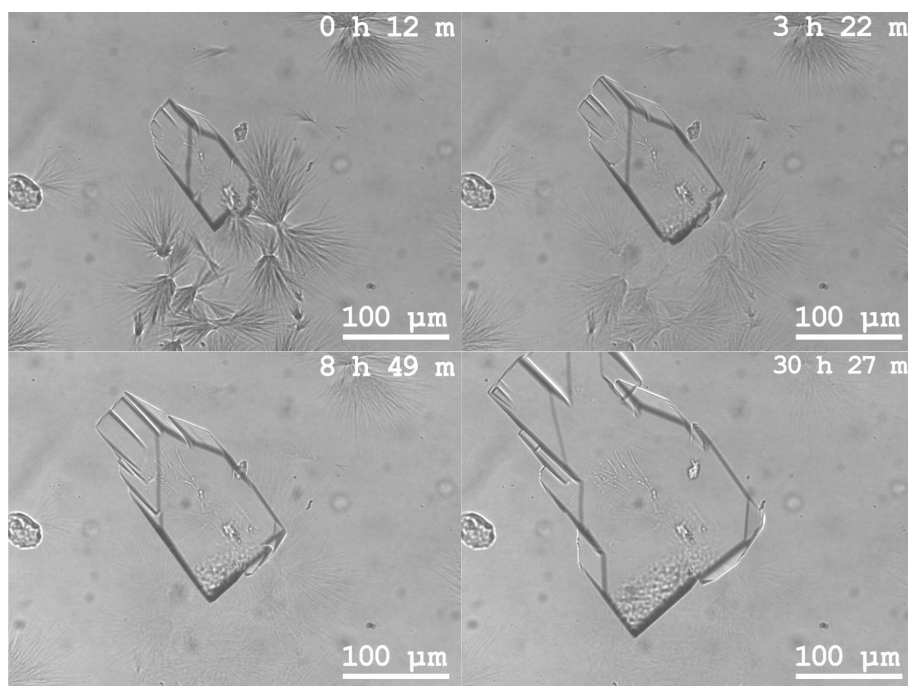
Figure 4.3: Series of in-situ optical micrographs of HEWL spherulites and a monoclinic HEWL crystal coexisting in the same solution, grown at 18°C from a 15 mg/ml HEWL, 0.6 M NaNO$_3$ and 0.05 M NaCH$_3$COO/HCH$_3$COO buffer solution at pH 4.5. Due to a raise in temperature up to 30°C, the spherulites dissolve while at the same time the monoclinic crystal continues to grow. Time since the temperature raise is indicated in the upper right corner of the micrographs.

supersaturated with respect to the monoclinic polymorph. Thus, increasing solute concentration appears to be a better strategy to prevent spherulite formation than modifying the solvent properties by increasing the salt concentration, which changes the ionic strength of the solution.

The spherulites grown in sodium thiocyanate solutions show similar behaviour with respect to their stable monoclinic counterpart. This implies that also in the lysozyme-thiocyanate system the spherulites form a second, metastable, polymorph.

In literature, the nucleation of protein spherulites is often associated with the presence of liquid-liquid phase separation[3, 4, 21, 25]. The small gelled protein droplets might act as heterogeneous nuclei for the needles. However, we found that the number of spherulites found in phase separated systems did not differ greatly from the number of spherulites in non-separated systems. The nucleation probably occurs heterogeneously, because more spherulites were observed in the presence of foreign particles, i.e. when using stock solution without filtering.

4.3.2   Morphology of spherulites

Spherulites are often divided into two morphologic categories, which differ in the nucleation mechanism[5]. Type I is assumed to be a result of heterogeneous nucleation, with thin needles radially growing outward from a more or less spherical particle (figure 4.4a). The second type is thought to be the result of homogeneous nucleation. A single needle is formed by homogeneous nucleation, which subsequently branches leading to a *sheave*-like morphology (figure 4.4b). After continued growth, the branching can even result in both ends of the dumbbell shaped spherulite touching, creating a spherical shape with cavities inside.

Clearly, the spherulites in our experiment resemble type-II spherulites, with similar morphologies independent of salt and lysozyme concentration. In growth cells with large spacing in the third dimension the sheave-like spherulites can also resemble type-I spherulites, when viewed along their longitudinal axis (figure 4.5). However, in the experiments with a maximum of 10 μm of
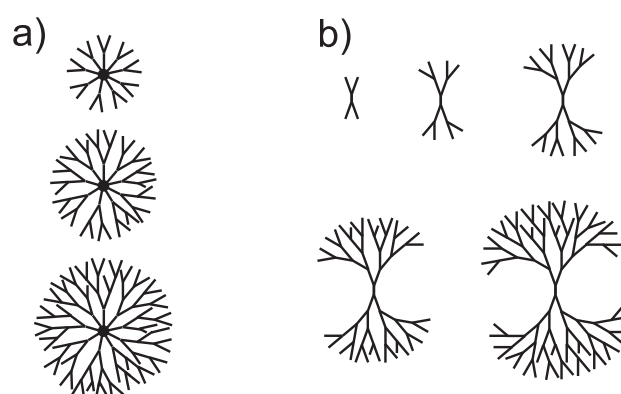
Figure 4.4: Schematic representation of the formation of spherulites. a) Type 1 spherulites are formed by heterogeneous nucleation on a foreign particle, for instance a dust particle. Crystalline needles radiate outward from this nucleus. b) Type 2 spherulites form by the homogeneous nucleation of a single crystalline needle, which subsequently grows and branches off.
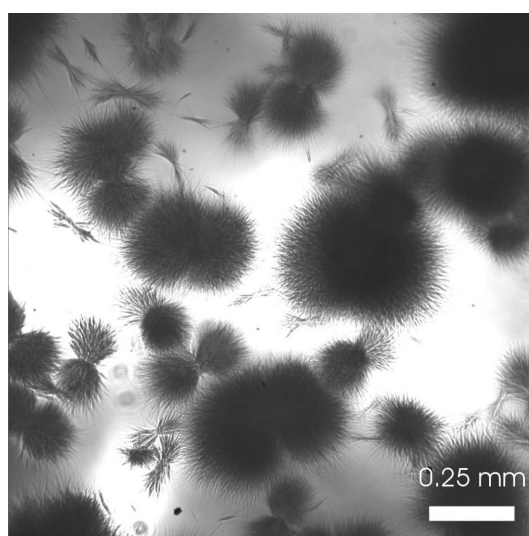
Figure 4.5: Spherulites grown from a 40 mg/ml HEWL / 0.2 M NaNO$_3$ / 0.05 M NaCH$_3$COO solution in a 2 ml vessel (5 mm in height), resulting in three-dimensional spherulites. Viewed from different angles, the spherulites seem to have different shapes.

space in between the cover slides, all spherulites are sheave-like. The sheave-like spherulites also form when no filtering is applied to the solution, in which case one would expect type I spherulites as well. Thus, in the case of lysozyme spherulites, the customary classification into the two types does not hold. The nucleation needs not to be homogeneous to form a sheave-like spherulite following the scheme of figure 4.4b. A single needle can nucleate either homogeneously or heterogeneously, after which the type-II spherulites form. Due to filtering of the mother liquor, the foreign particle on which nucleation occurs is expected to be smaller than the 0.2 μm filter pores, and thus can be incorporated completely in the needle, allowing the spherulite to develop in opposite directions.

During growth, the needles of the spherulites exhibit repeated tip splitting, with an angle of 20 ± 5° in the sodium-nitrate experiments and 19 ± 7° in the sodium-thiocyanate experiments. The branching angles thus are preferential with a spread of approximately 10°, indicating a mechanism for tip splitting similar to crystallographic mismatch branching (CMB)[16, 17]. In CMB, heterogeneous 3D nucleation, for instance induced by additives adsorbed to the needle tip cause the needle to split in preferred directions, with the needle tip acting as a template. An experiment using ultra-pure lysozyme (99.99%, Mol Logics Inc, Japan) was performed in which spherulites with identical properties did form, indicating that foreign additives are not involved. Presumably the "additives" triggering tip splitting are either misoriented lysozyme molecules or clusters of molecules. The measured spread in the branching angle is increased by uncertainties induced by the fact that the needles often have some curvature (figure 4.1a).

From the optical images we find that the thickness of the needles depends on the distance from the spherulite centre, with the thick needles located at the centre and the thin needles near the periphery. The width of the outer needles is at most 1 μm, which is explained by the fact that these crystallites have had less time to grow. Also, the branching frequency depends on the distance from the growth centre, leading to longer branches on the outside.

When the system approaches equilibrium at the end of the experiment,
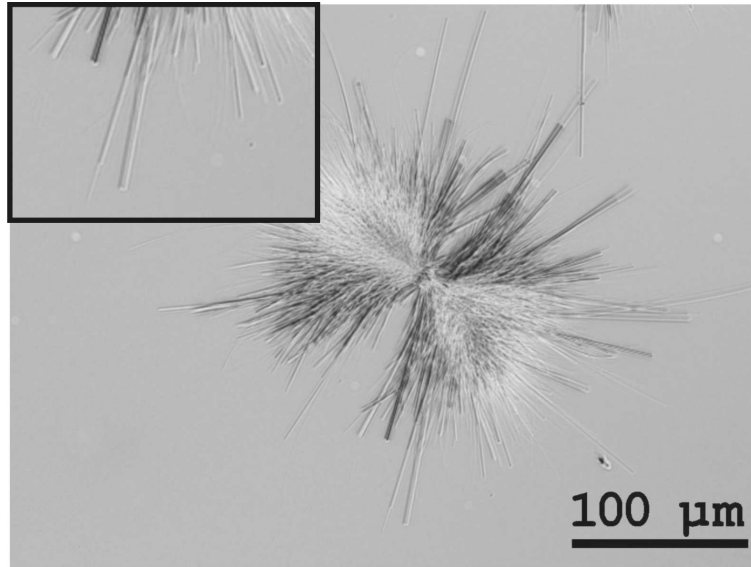
Figure 4.6: Negative of a polarisation microscope image of a spherulite with thick needles sticking out. As $\Delta\mu$ approaches zero, growth of the spherulites ceases. Some needles continue to grow very slowly, by which the aspect ratio also changes, as the top faces slow down with respect to the side faces and become faceted (inset). The extinction angle for the polarised light varies with the direction of the needles.

most needles cease to grow. Some of the needles continue to grow very slowly in width, depending on the local HEWL concentration. The width of these needles increases up to ~ 5 μm. The aspect ratio of the needles decreases and the tips of the needles become faceted (figure 4.6). These faceted top faces are not present during growth, which indicates that during growth the tips are kinetically rough[26]. The needle shape is the basic morphology of the spherulitic polymorph, both at low and high supersaturation.

4.3.3 Growth kinetics and diffusion

Using the in-situ temperature-controlled cell, the growth kinetics of the spherulites were investigated. In various experiments, the growth rate of spheru-

lites was determined from a time series of microscope CCD-images. Figure
4.7 shows a series of in-situ images of a spherulite growing from a buffered
NaNO$_3$ solution. The growth rates of the spherulites were determined by av-
eraging over an angular section of the spherulites as indicated in figure 4.7.
The spherulite size is calculated by dividing the surface area of the angular
section by the angle β. The length of the left and right side of this spherulite
is represented as function of time in figure 4.8a. Both sides show an almost
identical, constant growth speed up to a certain point at which it drops dra-
matically, due to the growth solution being exhausted. The growth speeds
in the linear regime are 0.95±0.03 μm/min and 0.86±0.01 μm/min for the
right and left side respectively. Constant growth rates were found in all ex-
periments, also for the experiments using NaSCN as crystallising agent. This
is in agreement with observations by Chow et al.[21] for HEWL spherulites
growing from sodium chloride solutions.

In the experiments of Chow et al.[21] surface kinetics are the rate limit-
ing step for the growth process. In our experiments, however, volume dif-
fusion seems also to play an important role, because during the growth of
the spherulite the region of separated liquid-liquid phase retracts from the
spherulitic growth front (figure 4.7). This retraction is a result of spherulite
growth depleting the surrounding solution. As the concentration drops, the
high-concentration droplets dissolve to replenish the lysozyme which is needed
to maintain equilibrium at the droplet interface. Thus, the boundary of the
phase separated region can be seen as an iso-concentration line correspond-
ing with the L-L phase separation equilibrium concentration. The retracting
iso-concentration line indicates that the surroundings of the spherulite are pro-
gressively depleted, suggesting that mass transport is also relevant. However,
when we regard a single needle of the spherulite as if it were a dendrite tip[27]
with a local diffusion field around it, we can write the following expression
for the concentration difference between the bulk of the solution and at the
surface (see appendix and figure 4.9):

$$c_b - c_s = \frac{v_{\mathrm{needle}}\, R}{4\, k\, D\, V_{\mathrm{mol}}} \;,\tag{4.1}$$
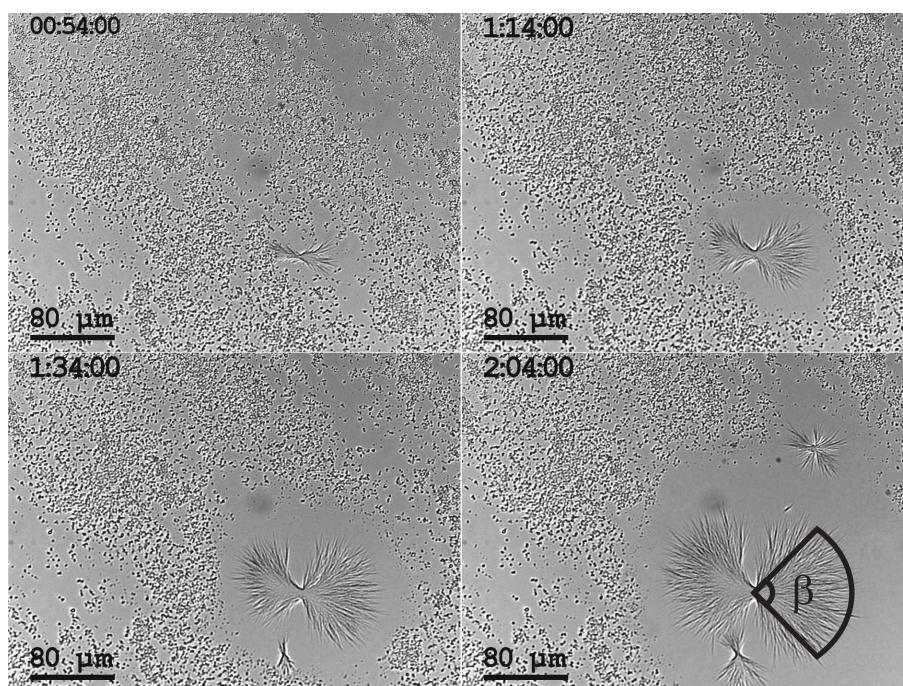
Figure 4.7: Series of images of spherulites growing in a 22 mg/ml HEWL / 0.8 M NaNO$_3$ / 0.05 M NaCH$_3$COO/HCH$_3$COO solution at 18°C and pH 4.5. Time indicated in the pictures is the time since the start of the experiment in hours-minutes-seconds. The small dots surrounding the spherulite are the liquid-liquid phase separation droplets.
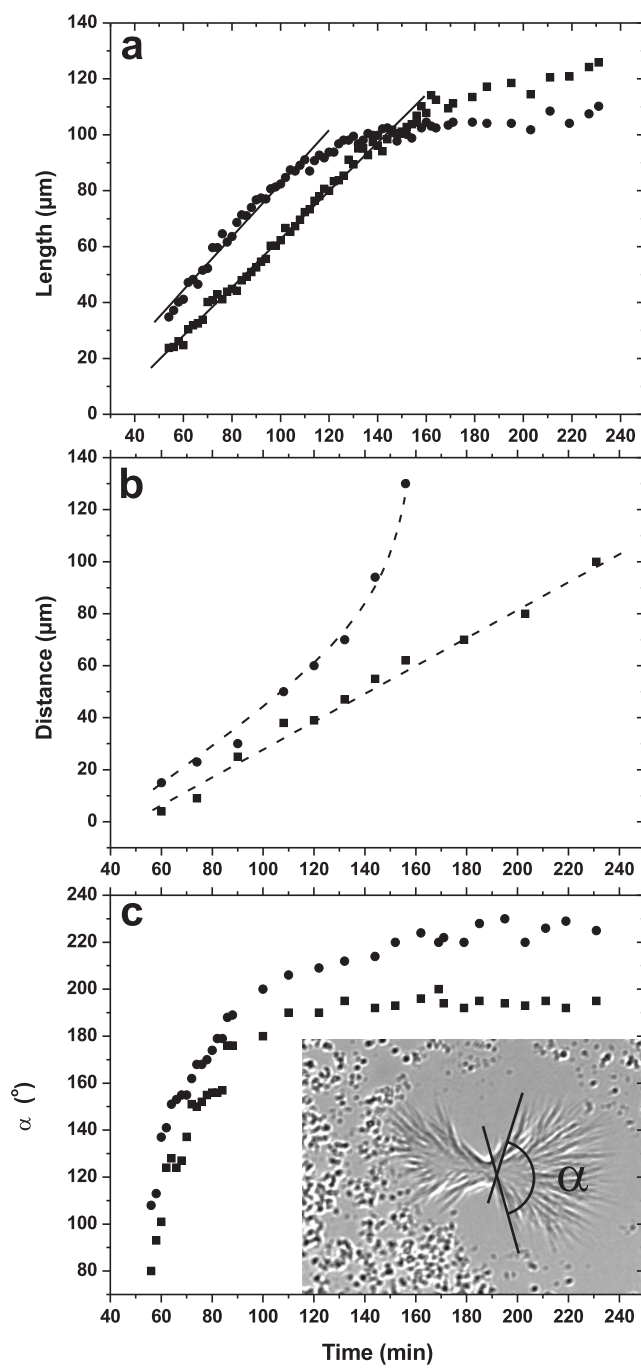
Figure 4.8: See page 74. Growth rate of the large spherulite in figure 4.7. (a)The squares indicate the length of the left side of the spherulite, and the circles indicate the length of the right side. The solid lines indicate linear fits for the surface kinetics regime. The left side has a growth rate of 0.86±0.01 μm/min, the right side 0.95±0.03 μm/min. (b) The squares and circles indicate the distance between the high-concentration droplets and the spherulite periphery for the left and right side respectively. Dashed lines are a guide to the eye. (c) The angle, α (see inset), for both the left (squares) and right (circles) side versus time.
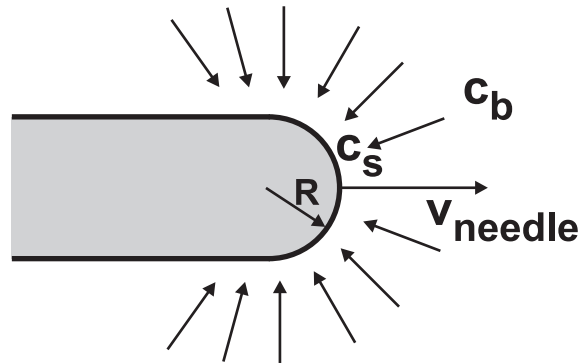
Figure 4.9: Model of a growing needle and its supply of material from its surroundings.

with c_b the bulk concentration, c_s the surface concentration, v_{needle} the growth rate of the needle, k a geometric correction factor, D the diffusion constant of lysozyme, and V_{mol} the volume of one lysozyme molecule. Taking $D = 1.2 \times 10^{-10}$ m^2/s from literature [28], and $v_{\text{needle}} = 15$ nm/s, and the needle tip radius $R = 0.5$ μm from experiment, we find a concentration difference in the order of 25 μg/ml, whereas the bulk concentration is typically in the order of 10 mg/ml, i.e. about 400 times larger. Thus, the surface concentration at the needle tips hardly drops, indicating surface kinetics to play a major role in the growth process and mass transport to have little effect.

Although for a single needle volume diffusion does not play a role, all

needles together, i.e. the spherulite as a whole, do deplete the surrounding
solution. An analysis similar to the single needle analysis can be performed,
resulting in (see appendix)

$$c_b - c_s = \frac{\xi \, v_{\text{needle}} \, R}{D \, V_{\text{mol}} \, N_A} \ln \frac{\delta}{R} \; , \tag{4.2}$$

in which δ is the distance from the origin of the spherulite to the liquid-liquid
phase separated region, R in this case the spherulite radius, and ξ a density
correction factor for the fact that the spherulite is not a 100% dense structure,
but has solution-filled spaces in between the needles. In a rough approximation
using values for R and δ from experiment (squares in figure 4.8b) and esti-
mating $\xi \approx 0.2$ from experiment, the spherulite surface concentration drops
at a rate of 0.05 mg ml^{-1} min^{-1}. The surface concentration thus becomes
significantly lower than the bulk concentration during growth, indicating that
mass transport, although not the major limiting factor, plays an important
role in the growth process.

The decrease in supersaturation during continued spherulite growth influ-
ences both the branching frequency of the needles and the length of the needles
up to the next splitting. To determine the number of times the needles have
split, we measure the angle, α, between the outermost needles (see insert in
figure 4.8c) and divide it by the angle of 20° by which the needles typically
split. The angle α increases with time, but stops increasing even before the
needles slow down (figure 4.8c). When we plot the length of the spherulite ver-
sus the angle α, or the number of times the needles have branched, n, we find a
stepwise linear dependence (figure 4.10), which indicates that the influence of
decreasing supersaturation on the angle and on the length are different. Since
the top faces of the needles are kinetically roughened[26], the growth rate of
the needles is proportional to the supersaturation:

$$v_{\text{needle}} \propto \Delta\mu \; . \tag{4.3}$$

On the other hand, the formation of a new needle branch is a heterogeneous 3D
nucleation process, which, in its simplest form, is governed by an exponential

dependency of the nucleation rate J on the driving force[16, 29]:

$$J \propto e^{-f\gamma^3/\Delta\mu^2 kT} \ , \tag{4.4}$$

with γ the edge free energy, k Boltzmann's constant and T the temperature. Further, $f = \frac{16}{3}\frac{K}{}\pi\Omega^2$ in which Ω is the volume of a growth unit and K is a constant depending on the equilibrium shape of the heterogeneous nucleus[30]. As needle growth is largely controlled by surface kinetics, a considerable supersaturation still exists at the needle tips, which makes heterogeneous nucleation quite feasible. From this it follows that any change in driving force ($\Delta\mu$) has a higher impact on the tip splitting rate than on the growth rate and the average branching length v_{needle}/J increases for decreasing $\Delta\mu$. The same conclusion was drawn by Liu et al. for the growth of branched L-DHL fibres by the CMB process[16]. Figure 4.10 shows a linear regime for the left side up to $\alpha \approx 170$ ^{o}. In this regime the branching frequency is constant, implying a constant driving force, $\frac{\Delta\mu}{kT}$ and thus surface kinetics is the rate limiting step. During further growth branching becomes limited due to depletion of the solution and by volume diffusion, which is evident from the retracting L-L phase separation droplets. For the right side, the branching frequency is constant up to an abrupt stop. Neighbouring spherulites speed up the depletion of the solution resulting in this abrupt cessation of both branching and growth. Thus, volume diffusion has a significant influence on the morphology depending on the history and surroundings of the spherulite.

4.3.4 Simulated morphologies

To investigate qualitatively the balance between needle growth and tip splitting, we developed a model to calculate the shape of a spherulite using MATLAB[31]. In this model, the spherulite starts as a single needle that splits into two new needles at each end. These new needles in their turn split up at their tip, with the angle of bifurcation and its spread taken from experiment (20 ± 5°). Repeating the process of bifurcation of the needles results in a Cayley-like tree structure[32] of which the shape depends on the relation between needle length and the number of times the needles have split. In the
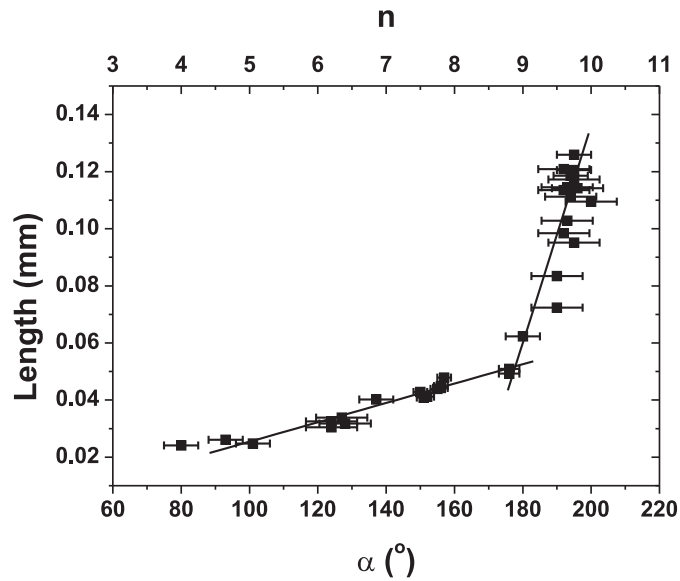
Figure 4.10: The angle, α, of the left side of the spherulite versus the length of the left side. The lines are linear fits used for the simulated morphology. n indicates the number of tip splittings.
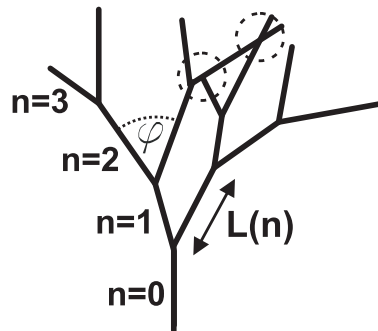
Figure 4.11: Illustration of a Cayley-like tree, showing the definition of bifurcation number n, needle length $L(n)$ and bifurcation angle φ. The length of an individual needle $L(n)$ depends on bifurcation number with an added stochastic deviation. The dashed circles indicate a needle being blocked by (left) and crossing over another needle (right).

experiments we find that needles cross over each other, but can be blocked as well. To mimic this behaviour, a blocking probability which equals the percentage of needles not surviving an encounter with another needle is added to the model (figure 4.11). The model thus builds up a Cayley-like tree with for every individual branch within a shell a stochastically different length and branching angle, and the possibility of a branch to end instead of to split.

Figures 4.12a to c show the calculated spherulite morphologies with 0%, 50% and 100% blocking probability using the two linear fits to the experimental data as indicated by the lines in figure 4.10. One fit concerns the linear surface kinetics limited regime, the second to approximate the volume diffusion limited regime, i.e.:

$$L(n) = \begin{cases} (-1.2 + 5.7n) \pm 20\% \ \mu\text{m} & n \leq 8 \\ (-512 + 65n) \pm 20\% \ \mu\text{m} & n > 8 \end{cases} \tag{4.5}$$

$L(n)$ is the needle length after the spherulite has bifurcated n times. On the basis of experimental data, the model returns a very similar morphology, indicating that tip-splitting is a viable mechanism in spherulite formation. A blocking probability of 50% results in a morphology which is most similar to experiment.

Preferably one would try equations 4.3 and 4.4 for the link between length and branching frequency in the model. However, as the nucleation rate depends on an exponential, the results strongly depend on the exponential and pre-exponential factor, which are difficult to determine from experiment. However, to illustrate the influence of the branching kinetics on the morphology, we used a few simple relations for $L(n)$. Figure 4.12d up to f show several model spherulites with a 50% blocking probability, with needle length $L(n) =$ constant, $L(n) = n$ and $L(n) = n^2$ respectively. The morphology clearly varies with the chosen relation between needle length and bifurcation number, especially the shape of the "eyes" of the spherulite. A constant branch length results in a very large, circular eye, while dependencies with excessively increasing needle-length produce long and narrow eyes. The relation $L(n) = n^2$ resembles the experiment most closely.
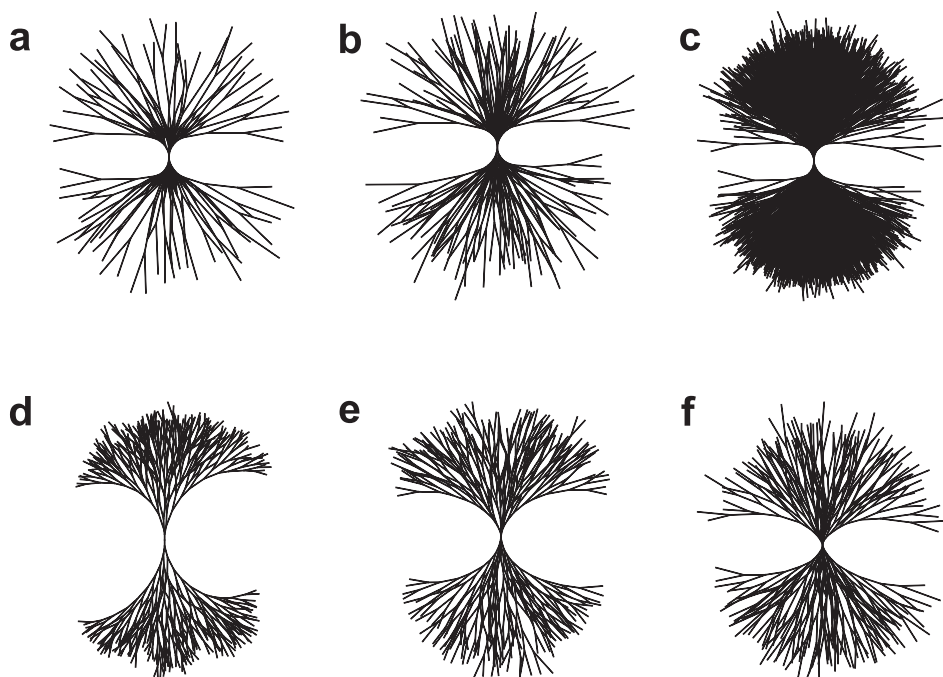
Figure 4.12: Calculated morphologies of spherulites based on the tip splitting mechanism. Panels a till c are calculations using linear fits to experiment, and a blocking probability of a) 100%, b) 50% and c) 0%. Panels d till f show calculated morphologies at a blocking probability of 50% for d) $L(n)$, the length of a branch as function of the number of tip splittings that have occurred, is constant, e) $L(n) = n$, and f) $L(n) = n^2$.

4.4   Conclusions

Hen egg-white lysozyme spherulites can be grown from NaNO$_3$ and NaSCN solutions. In both systems the needle-like crystals composing the spherulites are metastable with respect to the known HEWL protein phases. We conclude that HEWL spherulites grown from both solutions mainly grow in a sheave-like morphology, with very fine needles branching within a range of preferred angles suggesting crystallographic mismatch branching[16, 17]. Growth kinetics for the nitrate system indicate that surface kinetics largely limits the growth rate of an individual needle, while on the other hand the expanding depletion of the liquid-liquid phase separation region shows that volume diffusion can not be neglected for the spherulite as a whole. Observed and simulated morphologies indicate that volume diffusion limitation significantly influences the branching morphology of the spherulites. In general, choosing a high lysozyme concentration and a low NaNO$_3$ concentration prevents spherulite formation.

Acknowledgements

Appendix A: Stationary approximation of the diffusion fields around single needles, and around the complete spherulite

The spherulite needle can be regarded as a dendrite tip with a local diffusion field around it[27]. As the needle grows slowly compared to typical dendritic growth, the stationary approximation can be assumed. Thus, the surface of the needle does not move, and the concentration profile is time-independent. For a single needle, the system can be considered 3D as the needle thickness of ≈ 1 μm is much less than the liquid layer in the growth cell of 10 μm. Thus, mass transport for the local surroundings of the needle tip can be described

by solving Fick's equations $\nabla^2 c = 0$ and $\vec{J} = -D\vec{\nabla}c$ in spherical coordinates, i.e.

$$\frac{\mathrm{d}^2 c}{\mathrm{d}r^2} + \frac{2}{r}\frac{\mathrm{d}c}{\mathrm{d}r} = 0 \ . \tag{A.1}$$

Using boundary conditions at the needle tip and at large distance away (i.e. at infinity) the standard solution for equation A.1 becomes

$$c(r) = \frac{R\,(c_s - c_b)}{r} + c_b \ , \tag{A.2}$$

in which R is the radius of the needle tip (see figure 4.9), c_s the concentration at the surface, and c_b the bulk concentration. Using Fick's first law in spherical coordinates, $J = -D\frac{\mathrm{d}}{\mathrm{d}r}c$, we find the flux J of mass *into* the needle tip

$$J(R) = D\,\frac{c_b - c_s}{R} \ , \tag{A.3}$$

in which D is the diffusion constant of lysozyme. The gain in volume of the needle per unit time $\frac{\mathrm{d}V}{\mathrm{d}t}$ is related to this flux by

$$\begin{aligned}
\frac{\mathrm{d}V}{\mathrm{d}t} &= 4\pi\,R^2\,k\,V_{\mathrm{mol}}\,N_A\,J \\
&= 4\pi\,R\,k\,V_{\mathrm{mol}}\,N_A\,D\,(c_b - c_s) \ ,
\end{aligned} \tag{A.4}$$

in which $\frac{1}{2} \leq k \leq 1$ is a factor to compensate for the fact that the top of the needle is not a complete sphere (figure 4.9), V_{mol} the volume of one HEWL molecule, and N_A Avogadro's number. The volume increase can also be expressed in terms of the growth speed of the needle, v_{needle}:

$$\frac{\mathrm{d}V}{\mathrm{d}t} = \pi\,R^2\,v_{\mathrm{needle}} \ . \tag{A.5}$$

Thus, substituting equation A.5 in A.4 results in an expression for the difference between surface concentration and bulk concentration:

$$c_b - c_s = \frac{v_{\mathrm{needle}}\,R}{4\,k\,D\,V_{\mathrm{mol}}\,N_A} \ . \tag{A.6}$$

The spherulite as a whole can be approximated by a flat cylinder and thus the cylindrical instead of the spherical form of Fick's laws has to be used:

$$\frac{\mathrm{d}^2 c}{\mathrm{d}r^2} + \frac{1}{r}\frac{\mathrm{d}c}{\mathrm{d}r} = 0 \ , \tag{A.7}$$

with the general solution

$$c(r) = a \ln r + b .\tag{A.8}$$

In this case we cannot take the boundary condition at $r = \infty$, but we have to choose a finite distance δ for c_b. A logical choice is the perimeter of the liquid-liquid phase separated region. Although experiment clearly shows that the concentration profile cannot be considered stationary, it is a good and often used first approximation to consider the system stationary for any point in time. The concentration profile at such a time is a function of r and is given by

$$c(r) = c_s + \frac{c_s - c_b}{\ln \frac{R}{\delta}} \ln \frac{r}{R} .\tag{A.9}$$

Following the same route as for the single needle case we find an expression for the concentration difference $c_b - c_s$

$$c_b - c_s = \frac{\xi \, v_{\text{needle}} \, R}{D \, V_{\text{mol}} \, N_A} \ln \frac{\delta}{R} ,\tag{A.10}$$

in which ξ is a density correction factor for the fact that the spherulite is not a 100% dense structure but has solution-filled spaces in between the needles. The rate by which the surface concentration drops can be determined by substituting values for R and δ taken from subsequent images into equation A.10.

References

[1] McPherson, A. *Crystallization of Biological Macromolecules;* Cold Spring Harbor Laboratory Press: New York, 1999.

[2] Coleman, J.; Allan, B.; Vallee, B. *Science* **1960,** *131*, 350-352.

[3] Tanaka, S.; Yamamoto, M.; Ito, K.; Hayakawa, R.; Ataka, M. *Phys. Rev. E* **1997,** *56*, R67.

[4] Muschol, M.; Rosenberger, F. *J. Chem. Phys.* **1997,** *107*, 1953-1962.

[5] Philips, P. . In *Handbook of Crystal growth*, Vol. 2; Elsevier: Amsterdam, 1993; Chapter 18, pages 1169–1216.

[6] Gránásy, L.; Pusztai, T.; Tegze, G.; Warren, J.; Douglas, J. *Phys. Rev. E* **2005,** *72,* Art. No. 011605.

[7] Briehl, R. *J. Mol. Biol.* **1995,** *245,* 710-723.

[8] Magill, J. *J. Mater. Sci.* **2001,** *36,* 3143-3164.

[9] Prymak, O.; Sokolova, V.; Peitsch, T.; Epple, M. *Cryst. Growth Des.* **2006,** *6,* 498-506.

[10] Grases, F.; Villacampa, A.; Costa-Bauza, A. *Urological Research* **1999,** *27,* 141-147.

[11] Wang, Q.; Morse, J. *Mar. Chem.* **1996,** *52,* 99-121.

[12] Keith, H. D.; Padden, F. J. *J. Appl. Phys.* **1963,** *34,* 2409-2421.

[13] Bisault, J.; Ryschenkow, G.; Faivre, G. *J. Cryst. Growth* **1991,** *110,* 889-909.

[14] Liu, X. *Top. Curr. Chem.* **2005,** *256,* 1-37.

[15] Wang, R.; Liu, X.; Xiong, J.; Li, J. *J. Phys. Chem. B* **2006,** *110,* 7275-7280.

[16] Liu, X. Y.; Sawant, P. D.; Tan, W. B.; Noor, I. B. M.; Pramesti, C.; Chen, B. H. *J. Am. Chem. Soc.* **2002,** *124,* 15055-15063.

[17] Li, J. L.; Liu, X. Y.; Wang, R. Y.; Xiong, J. X. *J. Phys. Chem. B* **2005,** *109,* 24231-24235.

[18] Liu, X. Y.; Sawant, P. D. *Adv. Mater.* **2002,** *14,* 421-426.

[19] Echalier, A.; Glazer, R.; Fülöp, V.; Geday, M. *Biol. Crys.* **2004,** *60,* 696-702.

[20] Guilloteau, J.; Fromage, N.; Ries-Kautt, M.; Reboul, S.; Bocquet, D.; Dubois, H.; Faucher, D.; Colonna, C.; Ducruix, A.; Becquart, J. *Proteins* **1996,** *25*, 112-119.

[21] Chow, P.; Liu, X.; Zhang, J.; Tan, R. *Appl. Phys. Lett.* **2002,** *81*, 1975-1977.

[22] Guilloteau, J.; Riès-Kautt, M.; Ducruix, A. *J. Cryst. Growth* **1992,** *122*, 223-230.

[23] Heijna, M.; van den Dungen, P.; van Enckevort, W.; Vlieg, E. *Cryst. Growth Des.* **2006,** *6*, 1206-1213.

[24] Ostwald, W. *Z. Phys. Chem.* **1897,** *22*, 289-230.

[25] Bhamidi, V.; Skrzypczak-Jankun, E.; Schall, C. *J. Cryst. Growth* **2001,** *232*, 77-85.

[26] van Veenendaal, E.; van Hoof, P.; van Suchtelen, J.; van Enckevort, W.; Bennema, P. *Surf. Sci.* **1998,** *417*, 121-138.

[27] Glicksman, M.; Marsh, S. . In *Handbook of Crystal Growth*, Vol. 1; Elsevier: Amsterdam, 1993; Chapter 15, pages 1082–1085.

[28] Kim, Y.; Myerson, A. *J. Cryst. Growth* **1994,** *143*, 79-85.

[29] Kashchiev, D.; van Rosmalen, G. *Cryst. Res. Technol.* **2003,** *38*, 555-574.

[30] Mutaftschiev, B. . In *Handbook of Crystal growth*, Vol. 1; Elsevier: Amsterdam, 1993; Chapter 4, page 208.

[31] MATLAB 6.5 (Release 13), The MathWorks Inc.

[32] Cayley, A. *Philos. Mag.* **1858,** *28*, 374.

Chapter 5

Crystal growth in a three-phase system: Diffusion and liquid-liquid phase separation in lysozyme crystal growth

In the phase diagram of the protein hen egg-white lysozyme, a region is present in which the lysozyme solution demixes and forms two liquid phases. In-situ observations by optical microscopy show the dense liquid droplets to dissolve when crystals grow in this system. During this process the demixed liquid region retracts from the crystal surface. The spatial distribution of the dense phase droplets present a special kind of boundary conditions for Fick's second law for diffusion. In combination with the cylindrical symmetry provided by the kinetically roughened crystals, this system allows for a full numerical analysis. Using experimental data for setting the boundary conditions, a quasi-steady-state solution for the time-dependent concentration profile was shown to be valid. Comparison of kinetically rough growth in a phase separated system and in a non-separated system shows the growth kinetics for a three-

87

phase system to differ from a two-phase system, in that crystals grow more slowly but the duration of growth is prolonged.

5.1 Introduction

The capability of concentrated lysozyme solutions to undergo a separation into two liquid phases was first indicated by light scattering from unbuffered lysozyme-salt solutions[1]. Later, observations of liquid-liquid phase separation in buffered lysozyme solutions[2] and also other protein solutions followed [3, 4]. A phase diagram for the lysozyme-chloride system, indicating the binodal and spinodal of the metastable liquid-liquid separation, has been well established[5, 6]. L-L phase separation is relevant for protein crystallization, because cycling through the binodal into the two-phase region and back promotes nucleation of crystals[5], as does choosing crystallization conditions near the L-L coexistence line[7].

Although the mechanism of forming a low and high protein concentration phase would suggest crystal nucleation to occur in the dense liquid phase, for lysozyme it was found that due to gel formation, kinetics in these high-density droplets are arrested[5, 8] and thus nucleation is inhibited. Optical micrographs showing the growth of crystals in the presence of droplets of the dense liquid phase provide evidence that the dense liquid droplets do not cause the nucleation of new crystals[8, 9]. The disappearance of the dense phase around the crystal phase indicates a depletion zone due to the growing crystal[10–12]. The depletion of the dilute phase results in the dense phase dissolving into the dilute phase to locally restore the equilibrium concentration of this phase in contact with the dense phase.

In this paper, we specifically investigate the dissolution of the dense phase and its spatial distribution with respect to growing crystals. Previously, L-L phase separation was used to maintain a constant surface concentration during spherulitic growth of lysozyme[13]. Here, on the contrary, we use the retracting dense phase as an iso-concentration line in a diffusive system. The system presents a diffusion problem with two moving boundaries, and a special

condition due to the dense liquid phase dissolving into the dilute phase. A numerical analysis is presented showing the kinetics to be different from the case of diffusion without L-L phase separation. This represents a general case of crystal growth in a three-phase system in which a solid or liquid metastable phase dissolves, while a stable phase grows.

5.2   Experimental methods

Hen egg-white lysozyme from Sigma-Aldrich (lot nr. 094K1454) and chemicals of analytical grade were used in this study. A buffer stock solution of sodium acetate and acetic acid was made in deionized water (>15 MΩcm) to result in a 0.05 M NaCH$_3$COO/HCH$_3$COO solution of pH 4.5. A stock lysozyme solution was prepared by dissolving the lysozyme in the buffer solution and filtering this solution over a 0.2 μm membrane (Schleicher & Schuell). A sodium-chloride stock solution was also prepared in buffer solution and filtered. Lysozyme, NaCl and buffer solutions were mixed with each other in the appropriate proportions just prior to the growth experiments. All experiments performed used a sodium chloride concentration of 0.685 M (i.e. 4% w/v), because for this concentration literature provides phase diagrams on the liquid-liquid coexistence line[6, 8].

After mixing, a droplet of 10 μl is placed on a sapphire substrate and covered by a thin glass slide, forming an approximately 100 μm thick liquid layer, and is sealed off at the sides by vacuum grease to prevent evaporation. Performing the experiment in a thin layer prevents convection to occur and allows for better optical images of both the crystals and the spatial distribution of the dense droplets in the plane of projection. Next, the sample is placed on a precooled, temperature-controlled stage and covered by a brass plate to bring the solution into the demixing region of the phase diagram by cooling down. A 6 mm hole in the temperature-controlled stage and a 15 mm hole in the brass cover plate allow for transmission optical microscopy. The temperatures of the stage and cover plate were monitored by thermocouples and found to differ at most 0.3 ^oC.

Observations were made by transmission optical microscopy using a Nikon Microphot-88. The optical micrographs were recorded using a microscope mounted CCD camera (Nikon DS5M). Data on growth kinetics and droplet dissolution rates were determined from subsequent images with the aid of image processing software (Image-Pro Plus).

5.3 Results and Discussion

5.3.1 Liquid-liquid phase separation and kinetic roughening

In figure 5.1 we present a series of optical micrographs of a growing tetragonal lysozyme crystal surrounded by a phase-separated solution. After cooling down the solution containing 37.4 mg/ml HEWL to 8.1 ^oC, dense liquid phase droplets formed. The sample was checked for crystals to nucleate, and once found these crystals were observed during growth. The crystals start out kinetically rough, and appear circular in the images. Patterns on the surface indicate the four-fold axis of the $P4_32_12$ structure of tetragonal lysozyme to point out of the plane of projection (i.e. the {101} faces grow tilted with respect to the image plane, while the {110} faces are oriented perpendicular to the image plane). Around the crystal an area develops in which no high-density droplets are present. The outer border of this area moves away from the crystal surface as time progresses, while the crystal continues to grow. In the end all dense liquid droplets have dissolved and the crystal has become square.

Figure 5.2a shows a schematic phase diagram of the lysozyme-NaCl-buffer system. The liquidus and solidus indicate the equilibrium concentration of protein in the liquid and crystalline phase respectively, at given temperature. Mixtures in between these two lines will eventually separate in a solid, crystalline phase and a saturated solution. In this phase region, a metastable liquid-liquid miscibility dome is present. Mixtures in this region will separate in two liquid phases, of which the lower density phase subsequently separates into solid and liquid (fig. 5.2b). The concentration of the dilute phase drops as a result of the formation of the solid phase. As the dilute phase leaves the
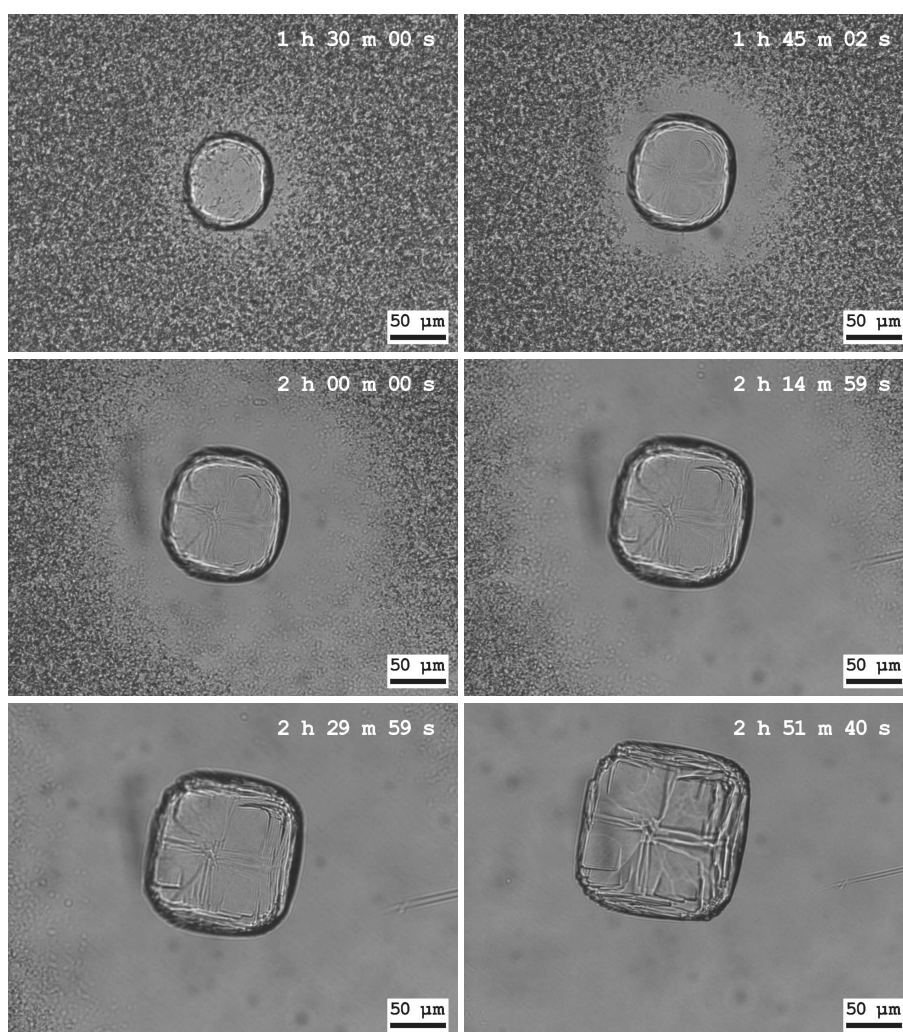
Figure 5.1: Optical micrographs of a tetragonal lysozyme crystal surrounded by a L-L phase separated solution at 8.1 °C. The crystal starts out kinetically rough, but as the surface concentration drops it becomes faceted. The high-density droplets dissolve into the low-density solution as a result of the low-density solution being depleted by the growing crystal. Before phase separation, the mother liquor consisted of 37.4 mg/ml HEWL, 0.685 M NaCl in a 0.05 M NaOAc/HOAc buffered solution at pH 4.5. The time in the upper right corner of the images indicates the time since cooling down below T_{cloud}.

liquid-liquid coexistence line, the dense phase dissolves into the dilute phase in an attempt to retain equilibrium (dotted arrow in fig. 5.2). The spatial distribution of the two-liquid-phases region is a result of the nucleation and growth of crystals in the dilute liquid. Figure 5.2c shows a micrograph of several crystals growing in a L-L phase separated region. Around the crystals depleted zones are visible, roughly following the shapes and positions of the crystals. Here, the high density droplets have dissolved, from which we conclude that the local concentration is lower than the dilute phase of the liquid-liquid coexistence (left dot in fig. 5.2b). At the edge of the depletion zone, the solution is in equilibrium with the dense solution droplets. Thus, this edge functions as an iso-concentration line and has the concentration of the low-density liquid.

At the beginning of the experiment, crystals nucleate in the low-concentration part of the solution. These crystals start out as circular crystals, but turn square in the course of the experiment (fig. 5.1). The rounded shape of the crystals indicates kinetic roughening of the surface[11, 14]. The mechanism by which a crystal grows depends on the supersaturation, σ. When the supersaturation is increased around a certain crossover supersaturation, σ_{tr}, the mechanism gradually changes from 2D nucleation to growth by continuous addition[11]. This transition to the kinetic roughening regime is a result of the supersaturation becoming so high that the critical nucleus for 2D nucleation, given by

$$r_{\mathrm{c}} = \frac{\Omega \gamma}{\Delta \mu \, h_{\mathrm{st}}} \ , \tag{5.1}$$

becomes equal to or smaller than the radius of one growth unit. In this equation γ is the edge free energy, and $\Delta \mu$ is the difference in chemical potential between liquid and solid phase. Further, Ω is the volume of a growth unit and h_{st} is the height of a growth layer. The thermodynamic supersaturation is linked to the chemical potential difference via $\frac{\Delta \mu}{kT} = \ln \frac{c}{c_{\mathrm{eq}}} \equiv \sigma$ (for an ideal solution). Thus, the change from a rounded shape into a square shape indicates a drop in concentration at the crystal surface during growth, in compliance with the dissolution of the dense liquid droplets near the crystal.

During a number of our experiments spherulites were formed simultane-
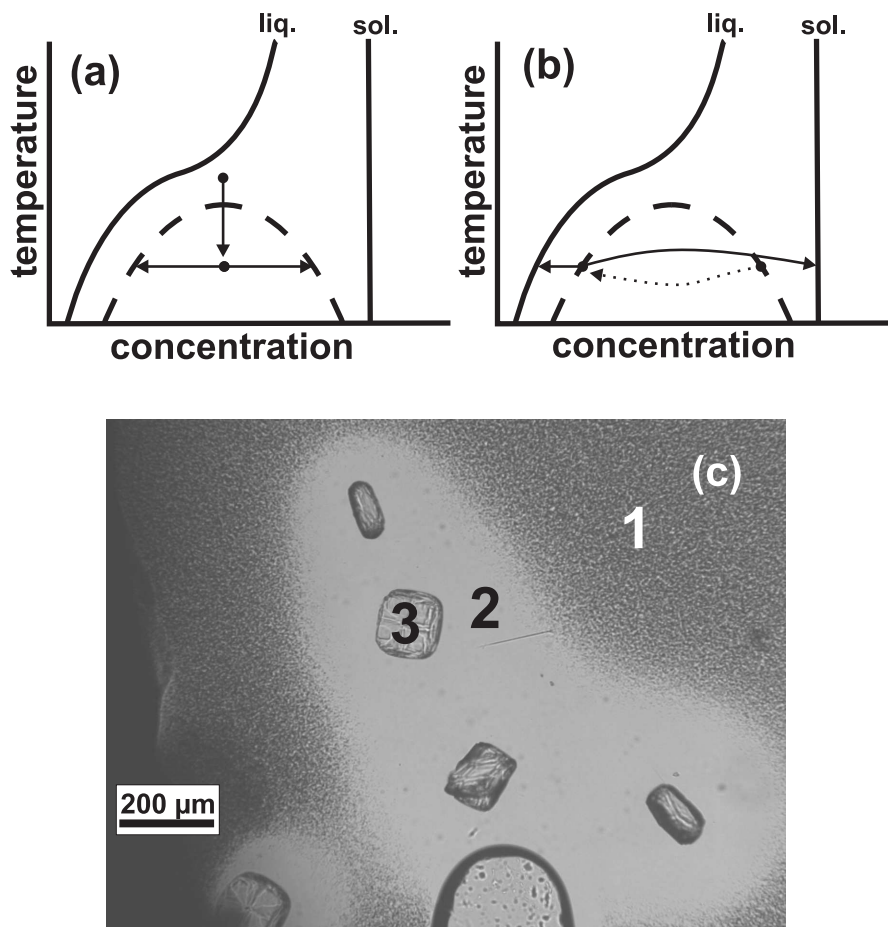
Figure 5.2: (a) Schematic phase diagram of the lysozyme-NaCl-buffer system. Experiments start out in the mixed phase between solidus and liquidus, and are brought into the liquid-liquid demixing region by cooling down (vertical arrow). The solution demixes and forms dense droplets in a diluted solution (horizontal arrows). The dense droplets gelate and kinetics are arrested. (b) The dilute solution, still between solidus and liquidus, separates in a solid, crystalline phase and an even more diluted solution (solid arrows). To maintain equilibrium with the dilute phase, the dense droplets dissolve into the dilute phase (dotted arrow). (c) Optical micrograph showing three phases of the lysozyme system simultaneously. The dense droplets (1) dissolve into the dilute phase as the growing crystals (3) deplete their surroundings (2).

ously with the tetragonal crystals. In reference [12] we showed that regular
crystal or spherulite growth is not necessarily related to the occurrence of the
liquid-liquid phase separation. In this paper the spherulites are not further
considered.

5.3.2   Droplet distribution and diffusion

From the optical images of the series in figure 5.1, the crystal growth rate
and the dense droplet retraction rate are determined. Figure 5.3a shows the
crystal size as function of time for two <110> directions and one <100>
direction. At 2.5 hours after cooling down, the crystal starts to become faceted,
i.e. the <100> direction grows faster than <110>. The change from kinetic
roughening to 2D nucleation growth is a gradual transition. After an initial
period (t <1.5 hrs), the dense droplets dissolve and "retract" from the crystal
surface faster than the crystal grows (fig. 5.3b). The L-L phase separation
boundary retracts from the crystal surface at 210 μm/hour, while the crystal
grows at a rate of 57 μm/hour.

Using the kinetics of crystal growth rate and dense droplet dissolution
rate, the concentration profile in the system can be evaluated. Due to the
thin geometry of the system, convection can be neglected. Mass transport in
the system follows Fick's laws of diffusion. Fick's second law gives a time-
dependent concentration field, by

$$\frac{\partial c(\vec{r}, t)}{\partial t} = D\nabla^2 c(\vec{r}, t) \ , \tag{5.2}$$

with $c(\vec{r}, t)$ the lysozyme concentration at position $\vec{r}$ at time t, and D the
diffusion coefficient. The combination of kinetically rough and approximately
circular crystals, and the circular pattern of dissolving dense droplets allows
the use of radial symmetry in solving equation 5.2 (see fig. 5.4). For the
{101} faces the roughening transition is at higher supersaturations, and in the
experiments these faces grow much slower than the {110} faces and thus have
far less influence on the concentration profile. Regarding the growing crystal
as a cylinder (fig. 5.4), the diffusion equation can be written in the cylindrical
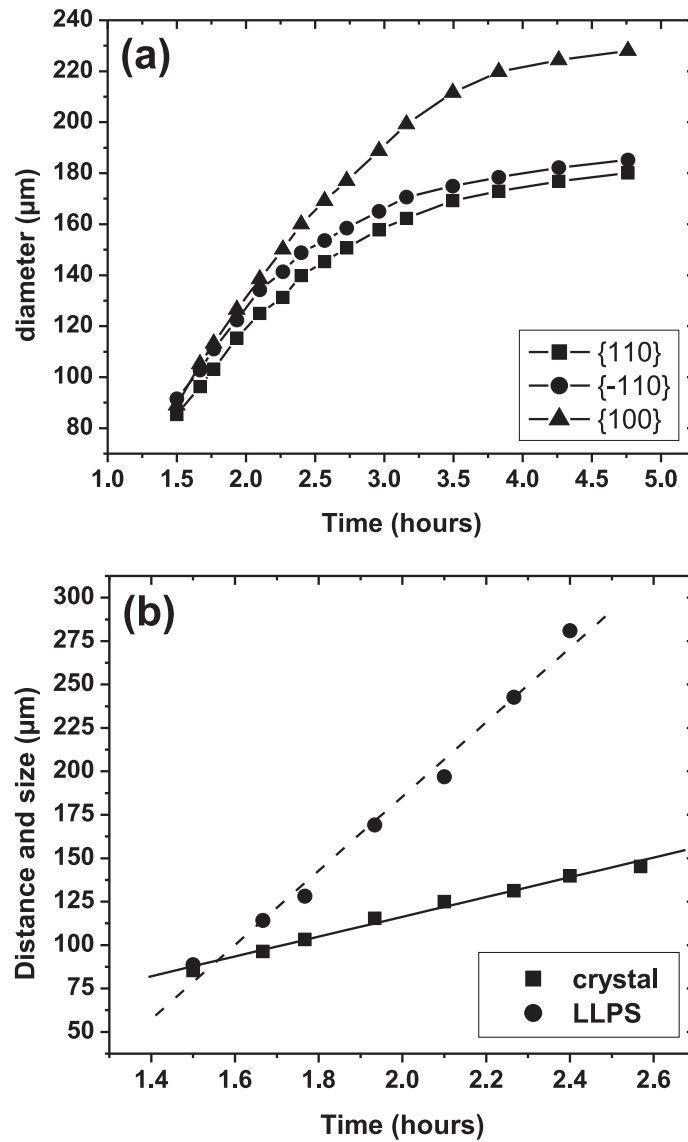
Figure 5.3: Data taken from the optical micrographs of figure 5.1. (a) Crystal size as function of time. (b) Size of the crystal and distance of the L-L phase separation boundary. The crystal grows at 57 μm/hour (slope of solid line), and the phase separation boundary retracts away from the crystal surface with 210 μm per hour (slope of dashed line).
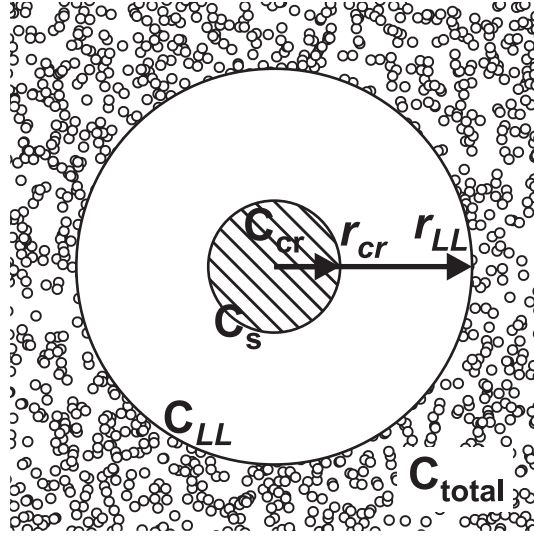
Figure 5.4: Schematic representation of a kinetically rough crystal growing from a L-L phase separated solution.

symmetric form:

$$\frac{\partial c(r,t)}{\partial t} = D\frac{\partial^2 c(r,t)}{\partial r^2} + \frac{D}{r}\frac{\partial c(r,t)}{\partial r} \;.$$

(5.3)

The solution of this equation depends on the boundary conditions. Experiments provide us with a set of boundary conditions, as the position of the crystal surface and the position of the L-L phase separation boundary at a certain time can be taken from the experimental data of figure 5.3. The concentration profile in between these boundaries follows from solving equation 5.3. The boundary condition at the crystal surface is determined by the flux at the surface. The flux across the crystal surface is determined by the crystal growth rate on the one hand, and by the concentration gradient at the surface on the other hand. The growth rate for kinetically roughened faces is given by[14, 15]

$$v_{\text{crys}} = \beta(c_{\text{s}} - c_{\text{tr}}) \;,$$

(5.4)

with β a kinetic coefficient* in $m^4\,s^{-1}\,g^{-1}$, c_{s} the surface concentration, and c_{tr}

---

*We assume the crystal to fill completely the vertical space in the growth cell. Finite

the cross-over concentration for kinetically roughened growth. For lysozyme, the cross-over concentration is 7.7 times the equilibrium concentration of the liquid phase[15], i.e. $c_{tr} = 7.7c_{eq}$. The mass flux into the crystal surface due to growth is given by

$$J_{cr} = v_{crys} \cdot c_{cr} = \beta \, c_{cr}(c_s - c_{tr}) \;, \tag{5.5}$$

in which c_{cr} is the lysozyme concentration in the tetragonal crystalline lysozyme phase. The diffusional mass flux at the crystal surface is given by

$$J_D = -D\frac{\partial c}{\partial r} \;. \tag{5.6}$$

The diffusional flux J_D is equal to the growth flux J_{cr}, and both give an expression for the relation between surface concentration and concentration gradient:

$$\frac{\partial c}{\partial r} = \frac{\beta c_{cr}}{D}(c_s - c_{tr}) \;. \tag{5.7}$$

The edge of the L-L phase separation region provides the outer boundary conditions for the radial diffusion equation. Here, at $r = r_{LL}$, the concentration is equal to the dilute phase concentration, c_{LL} (see figure 5.4), because dilute and dense phase are exactly in equilibrium. If for each moment in time the system is considered to be in a steady state, the time-independent diffusion equation can be used. In combination with the boundary conditions this leads to the solution[16]:

$$c(r) = \frac{c_{tr}r_{cr}h\ln(r_{LL}/r) + c_{LL}(1 + r_{cr}h\ln(r/r_{cr}))}{1 + r_{cr}h\ln(r_{LL}/r_{cr})} \;, \tag{5.8}$$

with r_{cr} the radius of the crystal, and h is $\beta c_{cr}/D$. The radii r_{cr} and r_{LL} are taken from experiment, and the physical parameters are taken from literature (see table 5.1). Figure 5.5 shows the concentration profiles at the various instances in time using this quasi-steady-state solution.

_____

elements calculations show that the concentration profile qualitatively remains the same when the crystal does not completely fills the vertical space. The effect on the boundary conditions is that we have an effective $\beta' = \beta \cdot h_{crystal}/h_{cell}$.

To evaluate if the quasi-steady-state approximation holds, we use the position of the crystal surface and phase separation as boundaries in a numerical solution of Fick's time-dependent equation by the finite differences method [16]. In this method, both time and radius are divided into discrete sections, and equation 5.3 can be written in a discrete form

$$\frac{c_i^{j+1} - c_i^j}{\Delta t} = \frac{D}{2i(\Delta r)^2} \left[(2i+1)c_{i+1}^j - 4ic_i^j + (2i-1)c_{i-1}^j \right] , \qquad (5.9)$$

in which c_i^j is the the concentration of the ith section of width Δr during the jth time section of length Δt. From equation 5.9 an expression for the concentration of the ith section at time $j+1$, c_i^{j+1} can be derived. We have calculated the time-dependent concentration profile using Matlab[17]. The positions of the moving boundaries, i.e. $r_{\text{cr}}(t)$ and $r_{\text{LL}}(t)$, are taken from experiment. Equation 5.7 and $c(r_{\text{LL}}) = c_{\text{LL}}$ are used at these boundaries similar to the quasi-steady-state case. The resulting concentration profiles (dashed lines in figure 5.5) show good agreement with the quasi-steady-state approximation. Thus, the quasi-steady-state model is a valid approximation. The surface concentration remains much higher than the equilibrium concentration (at least a factor 20), indicating that although the crystal grows kinetically rough, surface kinetics still play a major role in the growth process. This property of lysozyme crystal growth differs fundamentally from the kinetically rough growth of small molecules, in which rough growth depletes the surrounding solution to its equilibrium concentration and eventually leads to morphological instabilities. Here, the crystals grow rough, but do not loose their rounded shape. Although for a rough lysozyme crystal the critical nucleus has the size of one growth unit, the attachment of a properly oriented growth units takes more effort than for small molecules, and a barrier for incorporation still exists.

5.3.3   Two-phase system versus three-phase system

To investigate the difference between crystals growing in a L-L phase separated solution and those growing from a normal lysozyme solution, an experiment
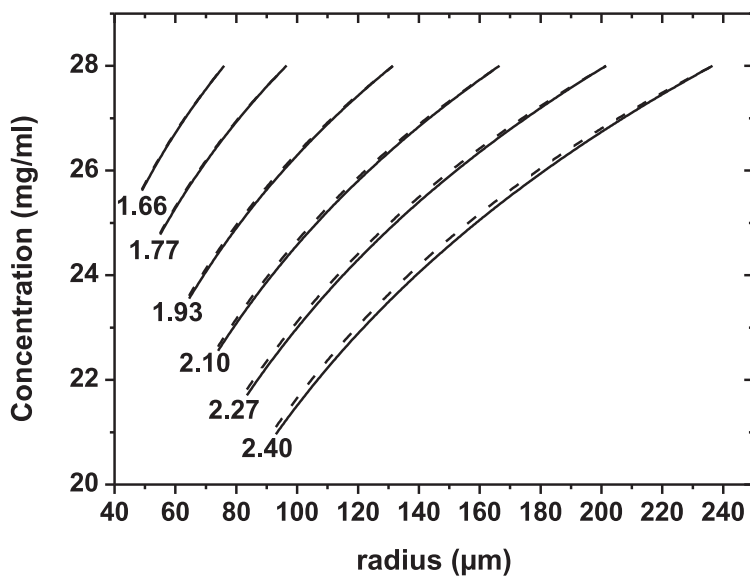
Figure 5.5: Concentration profiles at successive moments calculated using a quasi-steady-state approximation. The numbers indicate time in hours. The dashed lines indicate the time-dependent solution at the same instance calculated using finite differences. Data are taken from the experiment of figure 5.1

Table 5.1: Physical parameters taken from literature for finite differences calculations on the time-dependent diffusion equation, and for the quasi-steady-state calculations. c_{cr} is derived from the cell parameters of tetragonal lysozyme crystals and the molecular weight of lysozyme.

Parameter	Value	Ref.
β	$5 \times 10^{-8}\ cm^4\,s^{-1}\,mg^{-1}$	[15]
D	$8 \times 10^{-7}\ cm^2\,s^{-1}$	[18]
c_{equi}	$0.99\ mg/ml$	[19]
c_{tr}	$7.6\ mg/ml$	[15]
c_{LL}	$28\ mg/ml$	[6]
c_{cr}	$810\ mg/ml$	

was performed slightly above the L-L coexistence line at 8.5 ^{o}C. Here crystals also grow kinetically rough, but no dense liquid droplets are present in the vicinity. As the temperature difference between both experiments is minimal, we can consider the various constants, β, D, c_{equi} and c_{tr}, as identical, which allows for comparison between a system with and without L-L phase separation. Figure 5.6a shows the crystal size versus time for this experiment as well as that of the experiment at 8.1 ^{o}C, which includes phase separation. The crystal growing from the normal solid-liquid phase has a higher growth rate, but the growth rate drops more abrupt. With respect to the demixed system, the mixed system implies a higher supersaturation, as the lysozyme concentration here is higher than in the dilute phase of the L-L coexistence region. Temperature also influences the supersaturation, but works in favour of the demixed experiment and cannot be responsible for the difference in growth kinetics. Due to the absence of the dense liquid droplets, we cannot use these as an outer boundary condition in the quasi-steady-state approximation. Using a finite differences method, the time-dependent diffusion equations can be solved to investigate the differences in growth kinetics, now using different boundary conditions for the two experiments. Instead of using growth data to determine the boundary conditions, the fluxes at the interfaces are used to determine their movement. The growth rate of the crystal surface, $\frac{\text{d}r_{\text{cr}}}{\text{d}t}$, follows from equation 5.4, and is the driving force for the formation of a concentration gradient at the surface. The flux at the crystal-solution interface is given by eqs. 5.6 and 5.7. For the flux at the boundary of the L-L phase separated region we can write

$$J = (c_{\text{total}} - c_{\text{LL}})\frac{\text{d}r_{\text{LL}}}{\text{d}t} \ , \tag{5.10}$$

with c_{total} the effective concentration of dilute and dense phase combined. In the same manner as for the flux at the crystal surface, this flux is equal to the diffusional flux at the phase separation interface, resulting in

$$\frac{\text{d}r_{\text{LL}}}{\text{d}t} = \frac{D}{c_{\text{total}} - c_{\text{LL}}}\frac{\partial c}{\partial r}\bigg|_{r_{\text{LL}}} \ . \tag{5.11}$$

In contrast to the situation at the crystal surface, here we do not have an expression for the speed of the phase boundary. As the droplet surfaces are

rough and disordered and the surface-volume ratio is large, they can be considered to have an infinitely large kinetic coefficient for dissolution. Therefore, besides the flux boundary condition, a second boundary condition is given by the constant concentration as a result of the dissolution at an "infinitely" high rate, $c(r_{LL}) = c_{LL}$. The displacement of the L-L phase separation boundary now follows from the constant concentration at the boundary and the expression for the flux. For the system without phase separation present, at the outer boundary (the size of the growth cell or half the average distance between neighboring crystals), the concentration can change freely, but no flux of mass into the system is present, thus mimicking a finite system. The same boundary condition is used for the system *with* demixing at the moment the phase separation reaches the edge of the system. Figure 5.6b shows the calculated size of the crystal in both systems as function of time. Quantitatively, the calculated sizes do not fit the experiment completely, but qualitatively they do show the same sharp decrease of growth rate at 2.5-3 hours as the experimental data. Presumably this difference can be accounted for that depending on the quality of the lysozyme the actual values of the parameters given in table 5.1 might be slightly different. An important factor influencing the calculations is the choice of the size of the system. In an experiment, crystals in each others vicinity influence each others diffusion field and thus determine the "effective" system size. The moment of the sharp decrease in the crystal growth rate depends on the distance between adjacent crystals or the edge of the system. The calculations indeed show the unmixed system to grow faster than the demixed system, and also indicates a more abrupt stop in growth rate. Thus, the presence of the phase separation adds an extra step in the process of the material supply to the crystal surface by its dissolution, which leads to a different growth behaviour. The experiments show that the surroundings of a crystal influences growth kinetics and should be taken into account when interpreting the results of a crystallization experiment. These findings also hold for crystal growth systems with less constraining geometry, as long as convection is supressed so that the 3D versions of Fick's laws can be used. Such systems are crystal growth in microgravity[20], gels[21], nanoliter
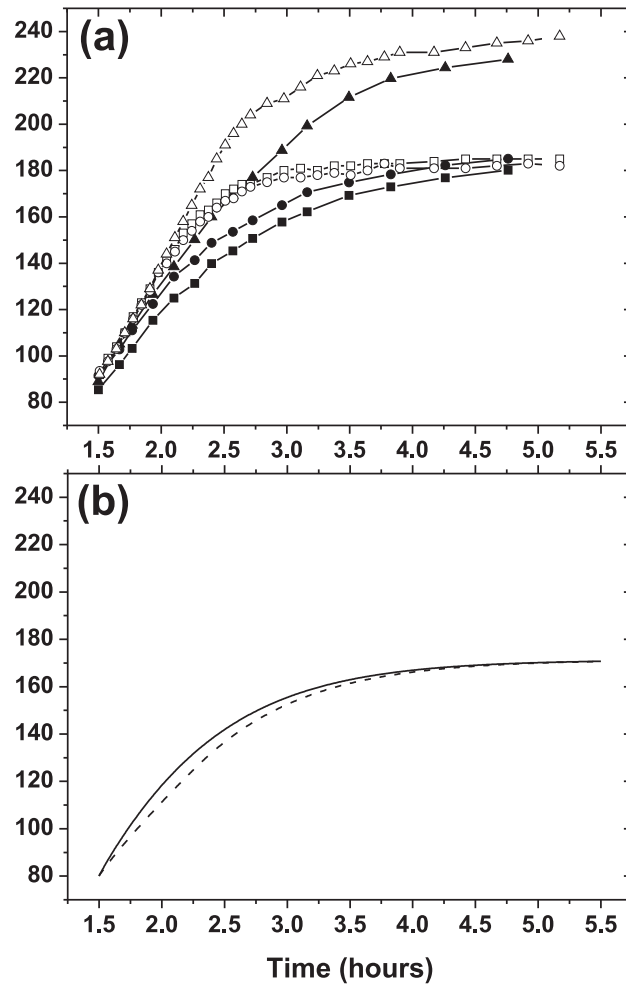
Figure 5.6: (a) Crystal size versus time for a kinetically rough crystal growing from a L-L phase separated system (solid symbols), and for a rough crystal growing in a system without L-L phase separation (open symbols). The squares and circles indicate the (110) and (1$\bar{1}$0) direction respectively, and the triangles indicate the (100) direction. (b) Crystal size for a system without (solid line) and with (dashed line) L-L phase separation modeled by using the finite differences method and boundary conditions as specified in the text. The physical parameters used are given in table 5.1; the effective radius of the finite growth system is 400 μm.

volumes[22], and strong inhomogeneous magnetic fields[23].

5.4 Conclusion

Hen egg-white lysozyme crystals growing in a liquid-liquid phase separated solution deplete their surroundings from growth units. The spatial distribution of the dissolving dense liquid droplets directly visualizes the role of mass transport in a diffusive lysozyme crystal growth system. The edge of the depleted zone can be seen as an iso-concentration line and therefore can be used as a boundary condition in calculations on diffusion. Crystals rounded as a consequence of kinetically rough growth allow for cylindrical symmetry to be applied in solving the diffusion equations. Finite differences calculations show that a quasi-steady-state approximation can be used to describe the time-dependent diffusion field using boundary displacements from experiment. Comparison of systems with and without liquid-liquid phase separation show that the presence of the phase separation alters the boundary conditions and thus the growth kinetics. To conclude, the lysozyme-NaCl system offers an interesting means of investigating mass transport in crystal growth, influenced by the presence of an extra metastable liquid or solid phase.

References

[1] C. Ishimoto and T. Tanaka, Physical Review Letters **39**, 474 (1977).

[2] V. G. Taratuta, A. Holschbach, G. M. Thurston, D. Blankschtein, and G. B. Benedek, Journal of Physical Chemistry **94**, 2140 (1990).

[3] M. L. Broide, C. R. Berland, J. Pande, O. O. Ogun, and G. B. Benedek, Proceedings of the National Academy of Sciences of the United States of America **88**, 5660 (1991).

[4] Y. G. Kuznetsov, A. J. Malkin, and A. McPherson, Journal of Crystal Growth **232**, 30 (2001).

[5] M. Muschol and F. Rosenberger, Journal of Chemical Physics **107**, 1953 (1997).

[6] D. N. Petsev, X. Wu, O. Galkin, and P. G. Vekilov, Journal of Physical Chemistry B **107**, 3921 (2003).

[7] O. Galkin and P. G. Vekilov, Proceedings of the National Academy of Sciences of the United States of America **97**, 6277 (2000).

[8] P. G. Vekilov, Crystal Growth & Design **4**, 671 (2004).

[9] S. Tanaka, M. Ataka, and K. Ito, Physical Review E **65**, 051804 (2002).

[10] S. Tanaka, M. Yamamoto, K. Ito, R. Hayakawa, and M. Ataka, Physical Review E **56**, R67 (1997).

[11] S. Gorti, J. Konnert, E. L. Forsythe, and M. L. Pusey, Crystal Growth & Design **5**, 535 (2005).

[12] M. C. R. Heijna, M. J. Theelen, W. J. P. van Enckevort, and E. Vlieg, Journal of Physical Chemistry **111**, 1567 (2007).

[13] P. S. Chow, X. Y. Liu, J. Zhang, and R. B. H. Tan, Applied Physics Letters **81**, 1975 (2002).

[14] E. van Veenendaal, P. J. C. M. van Hoof, J. van Suchtelen, W. J. P. van Enckevort, and P. Bennema, Surface Science **417**, 121 (1998).

[15] S. Gorti, E. L. Forsythe, and M. L. Pusey, Crystal Growth & Design **4**, 691 (2004).

[16] J. Crank, *The mathematics of diffusion* (Oxford University Press, London, 1975), 2nd ed.

[17] MATLAB 6.5 (Release 13), The MathWorks Inc.

[18] M. Muschol and F. Rosenberger, Journal of Chemical Physics **103**, 10424 (1995).

[19] E. L. Forsythe, R. A. Judge, and M. L. Pusey, Journal of Chemical and Engineering Data **44**, 637 (1999).

[20] C. E. Kundrot, R. A. Judge, M. L. Pusey, E. H. Snell, Crystal Growth & Design **1**, 87-99 (2001).

[21] M. C. Robert, F. Lefaucheux, Journal of Crystal Growth **90**, 358-367 (1988).

[22] D. C. Carter, P. Rhodes, D. E. McRee, L. W. Tari, D. R. Dougan, G. Snell, E. Abolac, R. C. Stevens, Journal of Applied Crystallography **38**, 87-90 (2005).

[23] M. C. R. Heijna, P. W. G. Poodt, K. Tsukamoto, W. J. de Grip, P. C. M Christianen, J. C. Maan, J. L. A. Hendrix, W. J. P. van Enckevort, E. Vlieg, Applied Physics Letters **90**, 264105 (2007).

Chapter 6

Suppression of convection using gradient magnetic fields during crystal growth of NiSO$_4$·6H$_2$0

A magnetic field was successfully used to suppress buoyancy driven convection during solution growth of a NiSO$_4$·6H$_2$O crystal. The disappearance of the convection plume and the expansion of the depletion zones, typical for crystal growth in the absence of gravity, were observed with schlieren microscopy when the product of magnetic field and field gradient corresponds to the condition that for all relevant concentrations buoyancy is compensated by paramagnetic counterforces. We show both theoretically and experimentally, that levitation of the growth solution is not the correct condition to suppress convection.

6.1   Introduction

For a wide variety of technical and scientific applications, the availability of high quality single crystals is of primary importance. For example in protein structure determination with X-ray diffraction, the crystal quality is often the limiting factor. Crystal quality is largely determined by processes during growth. To nucleate crystals from solution, highly supersaturated solutions are needed. Once crystals have nucleated, their growth depletes the solution in the vicinity of the crystal, resulting in a lower local density. This solution will rise due to buoyancy, which leads to convection that can be observed as a so-called growth plume[1]. Through a relatively thin (typically 0.1-0.3 mm) laminar flow boundary layer near the crystal surface, the crystal remains in contact with a highly supersaturated solution. Within this boundary layer, diffusion is the only means of mass-transport, leading to a thin depletion zone with a high concentration gradient. In a system where mass transport is important, this leads to a fast growth rate which affects crystal quality negatively, because defects have no time to heal. Therefore microgravity conditions, which suppress buoyancy, are believed to improve crystal quality, since without convection the depletion zone will extend continuously and crystal growth is automatically slowed down due to much slower mass transport[2].

A second effect that reduces the crystal quality arises from microcrystals that form at high supersaturations. Sedimentation of such microcrystals occurs in normal gravity and leads to increased mosaicity in the crystal after incorporation[3]. In this case microgravity conditions should also improve crystal quality. Therefore crystal growers and protein crystallographers in particular, have performed several growth experiments in space. However, space based experiments are rare and expensive, and have a low controllability and accessibility. The outcome of these studies on the beneficial effect of microgravity on crystal quality is therefore not conclusive[4–6].

6.2 Magnetic fields and convection

A promising alternative for space based experiments is the application of magnetic fields[7]. By applying a gradient magnetic field, a magnetic force is generated which can counteract gravity[8, 9]. Although many crystal growth experiments have been performed in magnetic fields, no experiment has yet shown that simulated microgravity in magnetic fields indeed leads to suppression of convection. In this paper we directly show by schlieren microscopy how the growth plume during crystal growth can be suppressed in a suitably chosen magnetic field.

Following a recent analysis of Ramachandran and Leslie[10] we first briefly discuss the forces acting on a body in a magnetic field. The net force F_z per unit volume along the z-direction on an object in a gradient magnetic field in vacuum or air is the sum of the magnetic force and the gravitational force given by[9, 10]

$$F_z = F_{magnetic} + F_{gravity} = \frac{\chi}{\mu_0} B_z B_z' - \rho g \ , \qquad (6.1)$$

with $B_z' = dB_z/dx$, χ the volume magnetic susceptibility, ρ the density, μ_0 the magnetic permeability of the vacuum, g the gravitational acceleration in the $-z$ direction and B_z the magnetic field along the z-direction. To achieve levitation, the magnetic and gravitational force should cancel each other so that $F_z = 0$, from which the levitation condition directly follows and which is demonstrated in levitating diamagnetic materials like bismuth[11], droplets of ionic solution[12], glass[12] and even frogs[9]. However, to obtain a microgravity-like condition for crystal growth where buoyancy driven convection is suppressed, levitation is not the correct condition. During crystal growth from solution, local variations in concentration occur, and thus also local variations in density and magnetic susceptibility. To achieve suppression of convection the force acting on different volume elements of the growth solution should be equal, leading to the following condition:

$$B_z B_z' = \frac{\Delta \rho}{\Delta \chi} \mu_0 g \ , \qquad (6.2)$$

with $\Delta\rho$ and $\Delta\chi$ the difference in the density and the volume magnetic susceptibility respectively between different solutal volume elements. For small variations in the concentration the density and susceptibility can be written as $\rho(c) = \alpha c + \rho_0$ and $\chi(c) = \beta c + \chi_0$, with α and β the coefficients of the linear concentration dependence of ρ and χ respectively. Eqn. (6.2) then becomes

$$B_z B_z' = \frac{\alpha}{\beta}\mu_0 g \ .$$ (6.3)

α is usually positive, while for diamagnetic materials χ is negative and of the order of 10^{-6}, with β usually also negative and small. Therefore, $B_z B_z'$ has to have a large and negative value, mostly beyond the reach of conventional magnets. For paramagnetic solutions, β is positive and much larger, which makes suppression of convection more easy. Note that Eqn. 6.2 and 6.3 show that if $\beta = 0$ it is impossible to suppress buoyancy driven convection, although it is possible to levitate the solution[13, 14].

Another consequence of the previous analysis is that the criterion to reduce sedimentation is given by Eqn. 6.2, which has been used by Maki *et al.* to grow lysozyme crystals floating in a paramagnetic solution[15]. Unlike in real microgravity, suppression of convection, reducing sedimentation or levitation cannot be done simultaneously using gradient magnetic fields.

6.3   Experimental setup

For an experimental validation of this method for convection suppression during growth, we investigated the growth of $NiSO_4\cdot6H_2O$ crystals from solution in a gradient magnetic field. Nickel sulfate crystals and their solution are paramagnetic. In order to calculate the conditions for convection suppression we measured the density and volume susceptibility as function of concentration range near the equilibrium concentration of 48.88 wt% at 25 ^{o}C[16]. The density measurements were performed by weighing a precisely determined volume of solution. The volume susceptibility measurements were performed using a MSB-Auto magnetic susceptibility balance from Sherwood Scientific Ltd. Results for these measurements are shown in Figure 6.1. We determined the
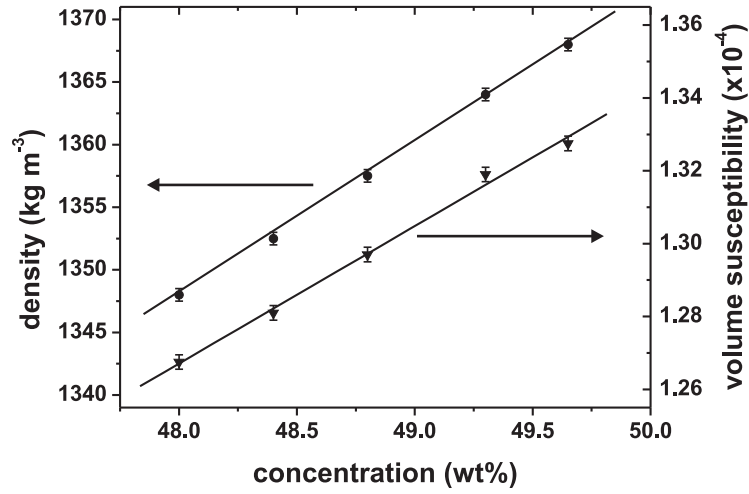
Figure 6.1: Density and susceptibility as function of concentration of an aqueous $NiSO_4 \cdot 6H_2O$ solution.

following values:

- $\alpha = 12.1 \pm 0.5$ kg m^{-3} wt% $^{-1}$

- $\beta = (3.8 \pm 0.2) \times 10^{-6}$ wt% $^{-1}$

6.4   Results and Discussion

With all parameter values known, we can calculate the required $B_z B_z'$ to suppress convection, stop sedimentation or to levitate the solution. We have estimated χ_{crystal} to be 3.2×10^{-4} by extrapolation of the data in figure 6.1. The values are shown in table 6.1, which also shows the predicted effective g value for convection.

Our experiments were performed using a 20 Tesla 32 mm bore resistive magnet with a calibrated field profile at the High Field Magnet Laboratory at the Radboud University Nijmegen. The position in the magnet we chose to perform our experiment has values of $B_z = 0.434B_0$ and $B_z' = 14.555B_z$, where B_0 is the maximum field at the center of the magnet. The samples were

prepared by gluing small single crystal fragments to a thin copper wire using superglue. These crystals were submerged in a slightly supersaturated solution so that they grew to a size of about 1 mm. The crystals were mounted in a glass cuvette with an inner volume of 7.5x7.5x15 mm^3. A long distance schlieren-type microscope was built to fit inside the magnet bore. With schlieren microscopy it is possible to visualize concentration gradients in-situ because the intensity is proportional to the gradient in concentration along the x-direction, i.e., $I \propto \partial n/\partial x \propto \partial c/\partial x$[17–19]. The temperature inside the bore was set to 25 ^{o}C and controlled by a double-walled tube connected to a thermostatic water bath. As growth solution, a 10.5% supersaturated nickel sulfate hexahydrate solution was used.

Figure 6.2 shows the main result of our experiment. At $B_z = 0T$, under normal gravity conditions, a growth plume can be seen rising from the crystal (Fig. 6.2a). At the sides of the crystal, zones of low and high intensities are visible. These are the depletion zones surrounding the crystal. The concentration gradient on the left side of the crystal is positive and on the right side of the crystal negative, leading to higher and lower intensities because of the schlieren principle. The average width of this depletion zone in the x-direction is 0.25 mm, which is a normal value. When slowly sweeping the field, we found that the growth plume disappeared for $B_z = 1.6T$. At this point, an effective microgravity condition was obtained with complete suppression of convection. After a transient of a few seconds due to the disappearance of the plume, the expansion of the depletion zones around the crystal took several minutes until the depleted zone reached a more or less fixed width of about 1 mm, 4 times as wide as at normal gravity conditions (fig. 6.2b).

Table 6.1 shows that the experimental value for $B_z B_z'$ as calculated from the field profile, agrees well with the predicted one from α and β. From this we can conclude that linearization of $\rho(c)$ and $\chi(c)$ is a valid approximation.

Increasing $B_z B_z'$ creates an inverse effective gravity. In figure 6.2c, a schlieren image is shown of the same growing crystal, but now with the growth plume directed downwards. The applied field was $B_z = 3.5T$. The width of the depletion zones decreased to approximately 0.25 mm again. We observed a
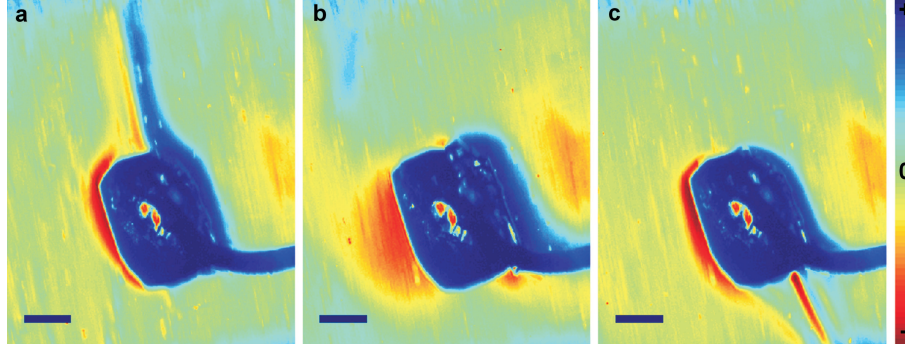
Figure 6.2: False color schlieren images of growing nickel sulfate crystals. (a) B_z=0 T (normal gravity). The crystal is solid blue and the blue stripe on the bottom-right is the copper wire on which the crystal is fixed. The plume is vertical, but the camera was slightly tilted. (b) After 5 minutes at B_z=1.6 T (suppression of convection) with an expanded depletion zone. (c) B_z=3.5 T (inverse effective gravity). The color indicates the concentration gradient, with red a large negative and blue a large positive gradient, according to the color bar on the right. The scale bar corresponds to 0.5 mm.

Table 6.1: The conditions to achieve suppression of convection, no sedimentation, or levitation.

Condition	$B_z B_z'$ (T^2 m^{-1}) Predicted	$B_z B_z'$ (T^2 m^{-1}) Experimental	$g_{\text{effective}}$ (m s^{-2})
No field	0		$1g$
Suppression of convection	39±3	37.5±0.5	$0g$
No sedimentation	45±5		$-0.1g$
Levitation	123±3		$-2g$

similar situation for all values of $B_z B_z'$ well above the convection suppression. Thus for the condition of magnetic levitation, convection is strong, and even enhanced as compared to normal gravity (see table 6.1).

In summary, we have reported for the first time that solutal convection during crystal growth can be suppressed by gradient magnetic fields, mimicking microgravity. We have found that the balance between magnetic and gravitational forces can be made sufficiently precise that the depletion zone expands, as expected in the absence of gravity. This leads to a strong reduction in the effective supersaturation, and thus holds promise to yield better crystals. We have proven theoretically as well as experimentally by in-situ schlieren microscopy that levitating the solution is not the right condition to achieve this situation. Some earlier experiments performed under levitation conditions can thus not have achieved convection suppression[13, 14]. Using gradient magnetic fields combined with in-situ optical techniques like schlieren microscopy offers a great opportunity to study the effects of microgravity-like conditions on crystal growth in general and protein crystal growth in particular. Although, unlike in real microgravity, suppression of convection and reducing sedimentation cannot occur simultaneously, the use of gradient magnetic fields can offer a good alternative for microgravity experiments in crystal growth.

Acknowledgements

References

[1] P.J. Shlichta, J. Cryst. Growth **76**, 656 (1986)

[2] A. McPherson, A.J. Malkin, Y.G. Kuznetsov, S. Koszelak, M. Wells, G. Jenkins, J. Howard, G. Lawson, J. Cryst. Growth **196**, 572 (1999)

[3] A. McPherson, A.J. Malkin, Y.G. Kuznetsov, S. Koszelak, J. Cryst. Growth **168**, 74 (1996)

[4] C.E. Kundrot, R.A. Judge, M.L. Pusey, E.H. Snell, Cryst. Growth Des. **1**, 87 (2001)

[5] T. Reichardt, Nature **404**, 114 (2000)

[6] E.H. Snell, J.R. Helliwell, Rep. Prog. Phys. **68**, 799 (2005)

[7] N.I. Wakayama, Cryst. Growth Des. **3**, 17 (2003)

[8] E. Beaugnon, R. Tournier, Nature **349**, 470 (1991)

[9] M.V. Berry, A.K. Geim, Eur. J. Phys. **18**, 307 (1997)

[10] N. Ramachandran, F.W. Leslie, J. Cryst. Growth **274**, 297 (2005)

[11] M. Hamai, I. Mogi, S. Awaji, K. Watanabe, M. Motokawa, Jpn. J. Appl. Phys. **40**, L1336 (2001)

[12] M. Motokawa, M. Hamai, T. Sato, I. Mogi, S. Awaji, K. Watanabe, N. Kitamura, M. Makihara, Physica B **294-295**, 729 (2001)

[13] N. I. Wakayama, Jpn. J. Appl. Phys. **44**, L833 (2005)

[14] D.C. Yin, N.I. Wakayama, K. Harata, M. Fujiwara, T. Kiyoshi, H. Wada, N. Niimura, S. Arai, W.D. Huang, Y. Tanimoto, J. Cryst. Growth **270**, 184 (2004)

[15] S. Maki, Y. Oda, M. Ataka, J. Cryst. Growth **261**, 557 (2004)

[16] R. Rohmer, Annales de Chemie **11**, 611 (1939)

[17] S. Kleine, W.J.P. van Enckevort, J. Derix, J. Cryst. Growth **179**, 240 (1997)

[18] G.S. Settles, *Schlieren and shadowgraph techniques*, Springer-Verlag, (2001)

[19] F.J. Weinberg, *Optics of flames*, Butterworths London, (1963)

Chapter 7

Magnetically controlled gravity for protein crystal growth

The occurrence of convective flows during crystal growth adversely affects crystal quality. Space-based crystal growth is therefore actively pursued, particularly for protein crystals, because buoyancy-driven convection is suppressed in microgravity. Here we demonstrate that magnetic fields can be used to tune the effective gravity from 1 g to -0.15 g during the growth of diamagnetic lysozyme crystals, and that convection can be damped, stopped and even reversed. This method provides a versatile and accessible way to realise an Earth-based tunable gravity environment for crystal growth, opening new avenues to optimise crystal quality.

117

7.1   Introduction

On earth, crystal growth from a supersaturated solution is accompanied by convection in the liquid; an effect often detrimental to crystal quality [1]. The convection is caused by buoyancy forces due to gravity, driven by the inherent density variations in the liquid near the growing crystal surface. For protein crystals a high quality is required for X-ray structure determination at high resolution [1, 2], which is of great biotechnological and pharmacological importance. However, protein crystals of high quality are difficult to grow, largely due to adverse effects of convection, which maintains a high growth rate and continuously supplies impurities to the surface of the crystals. For this reason much effort has been put in examining the virtues of space-based microgravity for protein crystal growth [1–3]. However, whether zero gravity is the ideal growth condition still is an open question and the attractive solution for optimising crystal quality, i.e. to be able to continuously tune the gravity, and thus convection, is yet to be achieved.

It has been shown that gradient magnetic fields can influence convective flows in paramagnetic fluids [4–6], and to apply the same approach to seemingly non-magnetic proteins is appealing, since in fact all diamagnetic materials can be magnetically levitated [7, 8]. For diamagnetic substances, the magnetic moment ($\mathbf{m}$) is proportional to the applied magnetic field ($\mathbf{B}$): $\mathbf{m} = \chi\mathbf{B}$, where χ is the magnetic susceptibility. A gradient magnetic field therefore leads to a magnetic force per unit volume given by $\mathbf{F}_{magn.} = \frac{\chi}{\mu_0}\mathbf{B}\nabla\mathbf{B}$, with μ_0 the magnetic permeability of free space, and pointed towards regions of low magnetic field.

The best known illustration of this effect is magnetic levitation, where the magnetic force counteracts the force of gravity $\mathbf{F}_{grav.} = \rho\mathbf{g}$ (ρ is the mass density and $\mathbf{g}$ is the gravitational acceleration), causing the object to float [7–9]. Magnetic levitation has been demonstrated for a large variety of diamagnetic materials [10–12], and even for living creatures [9]. The required condition for levitation is given by: $B_z B_z' = -\rho\mu_0 g/\chi$, where B_z' is the derivative of B_z in the z, i.e. vertical, direction. For most non-metallic diamagnetic substances the ratio ρ/χ is similar [12, 13] and the necessary field gradient (expressed in

terms of $B_z B'_z$) is approximately -1500 T^2/m.

The criterion for damping convection during crystal growth is quite different from that for levitation, because it relies on balancing buoyancy rather than gravitational force [5]. A growing crystal extracts solute from the solution and thus locally reduces the mass density of the solution. The diluted liquid close to the crystal surface will rise due to buoyancy, which leads to a convection pattern, comprising a thin (typically 0.1-0.3 mm) laminar flow boundary layer (depletion zone) and a so-called growth plume [14] on top of the crystal (Fig. 7.1a). Without convection this plume disappears, diffusion remains the sole means of mass transport and the depletion zone will expand to infinity (Fig. 7.1b). To suppress convection the buoyancy forces caused by differences in mass density ($\Delta\rho$) have to be opposed by magnetic buoyancy forces due to differences in magnetic susceptibility ($\Delta\chi$), giving $B_z B'_z = -\Delta\rho\mu_0 g/\Delta\chi$ [5, 6]. For small variations in concentration of the solute, both the density and the susceptibility depend linearly on concentration, i.e., $\rho(c) = \alpha c + \rho_0$ and $\chi(c) = \beta c + \chi_0$, leading to:

$$B_z B'_z = \frac{\alpha}{\beta}\mu_0 g \ . \tag{7.1}$$

The suppression of buoyancy depends therefore on the concentration dependence of the mass density and susceptibility (α and β), and not on the mass density and susceptibility themselves, as for normal and magneto-Archimedes [15, 16] levitation. In the latter case diamagnetic objects are lifted in a paramagnetic host environment in a relatively low field gradient (420 T^2/m), exploiting the large difference in susceptibility of object and host. In contrast, we need to balance buoyancy forces in a liquid with a *continuous* range of concentration dependent *diamagnetic* susceptibilities and mass densities, requiring very different values of the field gradient.
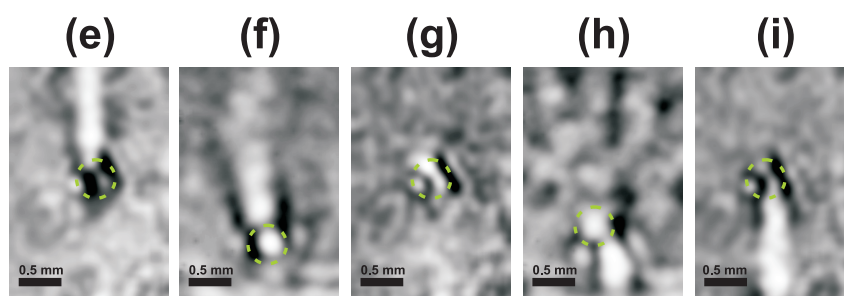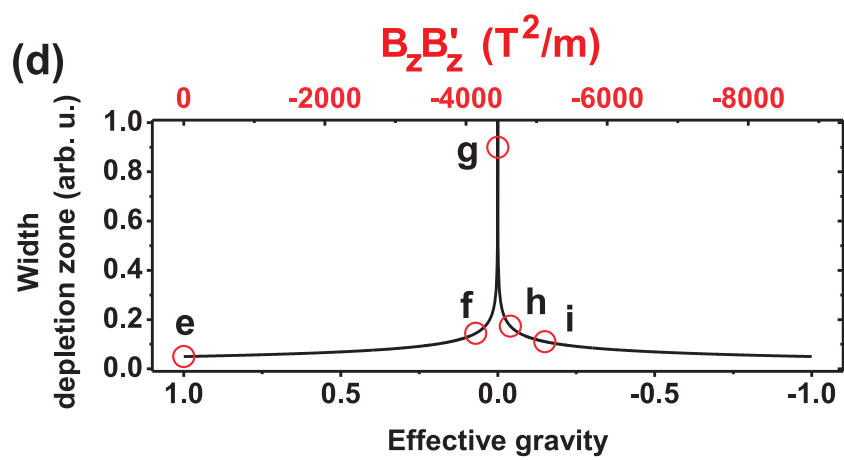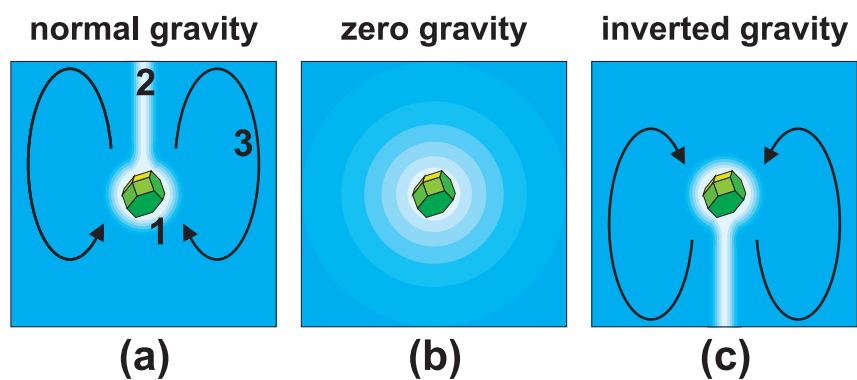
7.2   Experimental setup

We demonstrate the new method using the diamagnetic protein hen egg-white lysozyme (HEWL) for which crystallisation conditions have been well established and extensively investigated [17]. The experiments were performed in a

Figure 7.1: See page 121. Magnetically tuned gravity during crystal growth. (a) A growing crystal depletes its surrounding solution (1), leading to a growth plume (2) and convective flows (3). (b) At zero effective gravity convection is cancelled and the diffusion field expands. (c) In inverted gravity the buoyancy-driven convection is reversed, and a downward growth plume is formed. (d) Tuning of effective gravity is realised by changing the gradient magnetic field ($B_z B_z'$). G_{eff} affects the balance between convective and diffusive mass transport and determines the width of the depletion zone. (e)-(i) Experimental shadowgraphy images of a growing lysozyme crystal (indicated by the dashed green circles) in solution for G_{eff} ranging from -0.15 to 1.

33 T water-cooled resistive magnet with a bore diameter of 32 mm at the High Field Magnet Laboratory at the Radboud University Nijmegen. The magnet, fitted with a double-walled tube for temperature control by a thermostated water flow, contains a shadowgraphy [18] set-up for imaging convection patterns around the growing crystal (Fig. 7.2a). A glass cuvette (inner dimensions 8x4x18 mm^3) with crystal and solution was placed at the position of maximum field gradient $|B_z B_z'|$ (red curve in Fig. 7.2b), for a given maximum field B_0. The cuvette is illuminated from the side by a highly collimated beam of light from a halogen lamp, using an optical fibre in combination with a lens and a 75 μm pinhole, leading to an image on a CCD camera. Variations in the concentration of the fluid, like those between growth plume and bulk solution, lead to local differences in the refractive index, which appear as intensity variations in the image. The sensitivity to concentration differences scales with the degree of being out of focus [18].

We used hen egg-white lysozyme from Sigma-Aldrich (Lot nr. 094K-1454), which was dissolved and dialysed against a 0.05 M NaOAc/HOAc buffer solution of pH 4.5 at room temperature before use. Stock solution concentration was determined by UV absorption measurements at 281.5 nm [19]. Tetragonal lysozyme crystals were grown from a solution of 30 mg/ml HEWL, 0.685 M (or 4% w/v) NaCl and 0.05 M NaOAc/HOAc at pH 4.5 and 18 ^{o}C. Crystals

B_0	0	26.0	27.0	27.5	29.0 T
$B_z B'_z$	0	-4130	-4450	-4630	-5140 T^2/m
G_{eff}	1	0.07	0	-0.04	-0.15
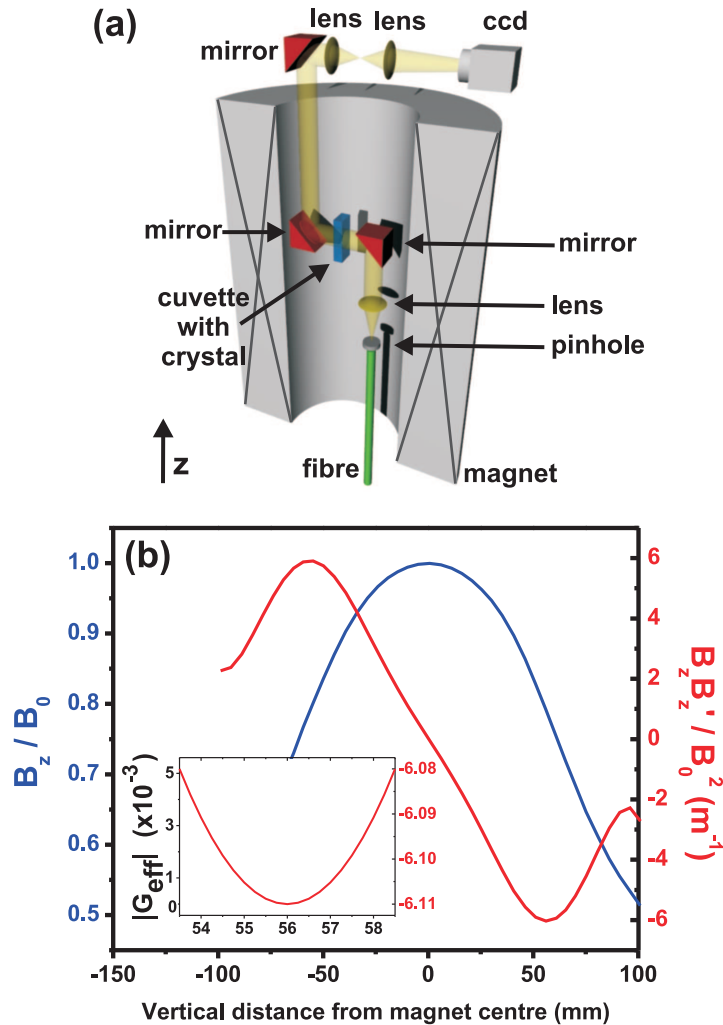
Figure 7.2: Experimental set-up for in-situ observation of convective fluid flows in a 33T magnet. (a) Schematic representation of the shadowgraphy insert used to visualise density variations in solutions. (b) Profiles of magnetic field and field times field gradient $(B_z B_z')$ scaled to a B_0 background field. The inset shows the $B_z B_z'$ profile around the optimum position and the corresponding effective gravity when convection is stopped. In this case, effective gravity ranges from 0 to 5×10^{-3} g over 5 millimetres in height, which demonstrates that milligravity is sufficient to cancel convection.

were taken from the growth vessel and placed as a seed in the glass cuvette for the magnet experiments. The crystal was manipulated to the right spot on the glass wall of the cuvette to be in the field of view of the insert, after which the solution was removed and the cuvette was placed in a refrigerator at 4 ^oC for 20 minutes. As a result, the crystal is attached to the glass wall of the cuvette. Finally, the cuvette was refilled with the same solution as used during growth and placed in the insert for experiments.

7.3   Results and discussion

The condition for convection damping is determined by α and β in equation 7.1. For HEWL α is 0.303 kg m^{-3} / mg ml^{-1} [20], and we have determined β to be (-1.2 $\pm$ 0.5)$\times 10^{-9}$ ml/mg using a magnetic susceptibility balance. Inserting these values in equation (7.1) we expect that convection is damped at $B_z B'_z$ = -3100 $\pm$ 1500 T^2/m, which is significantly larger than the -1500 T^2/m needed for simple levitation of the bulk solution. Given the inaccuracy of this estimated field gradient, caused by the small and difficult to determine value of β, we determined the actual gradient field at which the growth plume disappears by using shadowgraphy. Figure 7.1e shows a growing HEWL crystal at zero field gradient, and the convection plume is clearly visible as a white streak rising upward from the crystal. In the picture the crystal itself is blurred because for shadowgraphy out-of-focus images have to be taken. The growth plume disappears, and thus convection is suppressed, at a gradient magnetic field of -4450 $\pm$ 30 T^2/m (Fig. 7.1g). The value falls within our estimate using α and β, but is much higher than previously expected [5, 21] and requires the largest magnets currently available. In fact, this value for the gradient field accurately determines β as (-0.84$\pm$ 0.06)$\times 10^{-9}$ ml/mg.

This result unambiguously shows that gradient magnetic fields can create conditions on Earth that mimic those in space-based microgravity. Most importantly, however, is the fact that by changing the magnetic field strength the effective gravity for convection can be continuously varied. If we define

[22]

$$G_{\text{eff}} = 1 - \frac{\beta}{\alpha \mu_0 g} B_z B_z' \ , \tag{7.2}$$

G_{eff} is expressed in terms of the Earth's gravitational acceleration g. $G_{\text{eff}} = 1$ at zero magnetic field, while convection is cancelled at a field gradient for which $G_{\text{eff}} = 0$. By varying the magnetic field we are able to change G_{eff} from 1 to -0.15, and as a result the convection is tuned from normal, with a growth plume upwards (Fig. 7.1e,f, via cancellation at $G_{\text{eff}}{=}0$ (Fig. 7.1g), to inverted with the growth plume downwards for negative values of G_{eff} (Fig. 7.1h,i).

The range of field gradients at which convection is stopped is quite small, ±30 T^2/m centred around -4450T^2/m, which corresponds to $B = 27$ T in the magnet we used. Decreasing (increasing) the magnetic field by only 0.1 T ($G_{\text{eff}} \approx \pm0.005$) already results in appreciable convection and upward (downward) growth plumes. This strong effect is caused by the steep dependence of the balance between convective flow and mass diffusion on G_{eff}, which is reflected by the thickness of the depletion zone. For example, Fig. 7.1d shows the theoretically calculated, and for $NiSO_4 \cdot 6H_2O$ experimentally demonstrated [22], dependence of the thickness of the depletion zone δ on gravity. Since $\delta \propto |G_{\text{eff}}|^{-1/4}$ it diverges near zero, which implies that the field gradient has to be set quite precisely. Such a strong dependence also puts constraints on the spatial variation of G_{eff} within a magnet. From equation (7.2) we calculate G_{eff} as function of the position around the crystal using the experimental field profile (inset Fig. 7.2b), which shows that changes of G_{eff} over the relevant region are within ±0.005. Despite the precise condition on the required field gradient, *milligravity*, rather than microgravity [23], is sufficient to make convective transport slower than that due to diffusion, and successfully dampen convection.

To show that indeed the suppression of convection affects crystal growth, we have measured the growth rate of two lysozyme crystals, one at $G_{\text{eff}}{=}1$ (normal convection) and one at 0 (no convection), at otherwise identical conditions (Fig. 7.3). Here the same imaging set-up was used, but now with the crystal in focus to determine the position of its surface. The growth rate drops a factor of fifteen, from 30 ± 2 to 2 ± 2 μm per hour when convec-

tion is stopped and the depletion zone is expanded, which is similar to results obtained under space-based microgravity [24].
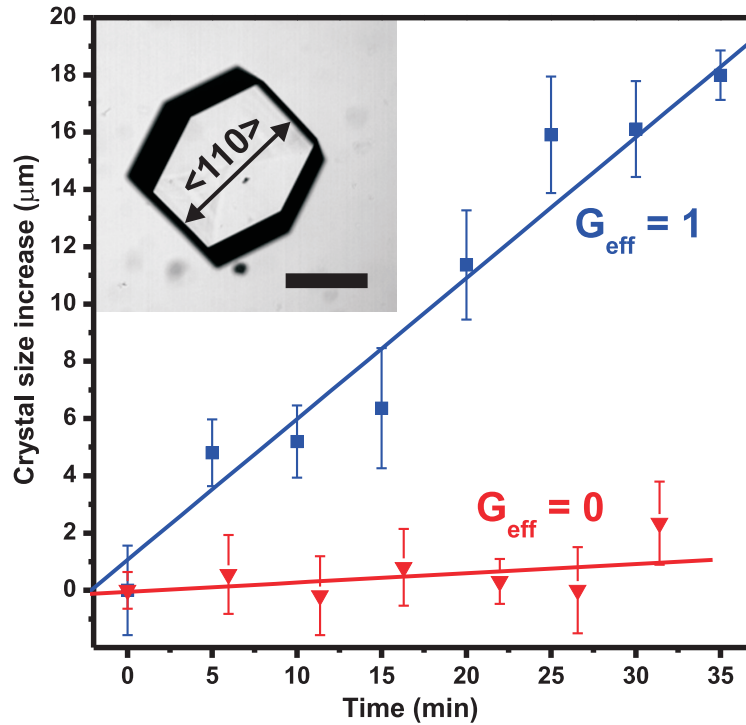
Figure 7.3: Growth rate of tetragonal hen egg-white lysozyme (HEWL) crystals at normal and zero effective gravity, G_{eff}. The squares (triangles) denote the increase in HEWL crystal size at a G_{eff} of 1 (0), obtained in the <110> direction, in a 30 mg/ml HEWL, 4% NaCl, 0.05 M NaOAc/HOAc solution at pH 4.5 and 18 ^{o}C. The growth rate at $G_{\mathrm{eff}}{=}0$ is 2 $\pm$ 2 μm/hr and is reduced by roughly a factor 15 compared to the growth rate at $G_{\mathrm{eff}}{=}1$ of 30 $\pm$ 2 μm/hr. The inset shows a tetragonal HEWL crystal similar to those used in the experiments, and the < 110 > direction with respect to the morphology. The scale bar indicates 500 μm.

In contrast with other methods to suppress convection [25, 26], gradient magnetic fields offer a powerful way to tune the effective gravity during crystal growth under Earth-based conditions, with far easier access, availability,

and including in-situ observation. Especially for protein crystal growth this possibility is very attractive, since the tunability allows us to optimise the crystal quality by finding the right balance between mass transport towards the crystal and the incorporation rate of molecules at the crystal surface. The required gradient magnetic fields for suppression of convection are found to be in the 4000-5000 T^2/m range, as expected from the concentration dependence of both mass density and magnetic susceptibility. Because density and susceptibility are closely related, we expect that this value is rather similar for most diamagnetic proteins, and possibly even for other diamagnetic compounds. For instance, we have found a value of (4070 ± 30) T^2/m for potassium dihydrogen phosphate. We foresee that our determination of the proper conditions for which convection is suppressed will trigger the design and construction of dedicated magnets (possibly combined with paramagnetic field enhancers), that are capable of sustaining high field gradients for the several days that are needed to grow protein crystals.

Acknowledgements

References

[1] E. H. Snell and J. R. Helliwel, Rep. Prog. Phys. **68**, 799 (2005).

[2] A. Vergara *et al.*, Biophys. Chem. **118**, 102 (2005).

[3] W. Littke and C. John, Science **225**, 203 (1984).

[4] D. Braithwaite, E. Beaugnon, and R. Tournier, Nature **354**, 134 (1991).

[5] N. Ramachandran and F. W. Leslie, J. Cryst. Growth **274**, 297 (2005).

[6] P. W. G. Poodt *et al.*, Appl. Phys. Lett. **87**, 214105 (2005).

[7] E. Beaugnon and R. Tournier, Nature **349**, 470 (1991).

[8] A. Geim, Physics Today **51**, 36 (1998).

[9] M. V. Berry and A. K. Geim, Eur. J. Phys. **18**, 307 (1997).

[10] E. Beaugnon and R. Tournier, J. Phys. III (Paris) **1**, 1423 (1991).

[11] J. S. Brooks *et al.*, J. Appl. Phys. **87**, 6194 (2000).

[12] M. Motokawa *et al.*, Physica B **294-295**, 729 (2001).

[13] J. F. Schenck, Ann. N.Y. Acad. Sci. **649**, 285 (1992).

[14] P. J. Shlichta, J. Cryst. Growth **76**, 656 (1986).

[15] Y. Ikezoe *et al.*, Nature **393**, 749 (1998).

[16] A. T. Catherall *et al.*, Nature **422**, 579 (2003).

[17] A. McPherson, *Crystallization of Biological Macromolecules* (Cold Spring Harbor Laboratory Press, New York, 1999).

[18] G. S. Settles, *Schlieren and Shadowgraphy Techniques* (Springer, Berlin, 2001).

[19] K. C. Aune and C. Tanford, Biochemistry **8**, 4579 (1969).

[20] W. J. Fredericks *et al.*, J. Cryst. Growth **141**, 183 (1994).

[21] N. I. Wakayama, Jpn. J. Appl. Phys. **44**, L833 (2005).

[22] P. W. G. Poodt *et al.*, Cryst. Growth Des. **6**, 2275 (2006).

[23] N. Ramachandran, C. R. Baugher, and R. J. Naumann, Microgravity Sci. Technol. **8**, 170 (1995).

[24] F. Otalora *et al.*, Acta Crystallogr. **D58**, 1681 (2002).

[25] M. C. Robert and F. Lefaucheux, J. Cryst. Growth **90**, 358 (1988).

[26] D. C. Carter *et al.*, J. Appl. Crystallogr. **38**, 87 (2005).

Chapter 8

PEG-induced morphologically unstable growth of tetragonal hen egg-white lysozyme crystals

Poly(ethylene glycol) (PEG) is an often used crystallising agent in screening experiments for protein crystallisation conditions. To investigate the influence of poly(ethylene glycol)-4600 on the diffusion process during protein crystal growth, a series of in-situ optical microscopy experiments was performed in which the diffusion coefficient was changed by the addition of PEG. Depending on the balance between diffusion coefficient and driving force, lysozyme crystals were found to grow faceted, kinetically rough, or morphologically unstable. In-situ observations show the development of a lysozyme crystal from polyhedral stability to instability and back to stability again as the balance changes within one experiment. A stability diagram showing the occurrence of morphological instability based on the starting conditions is presented, showing that kinetic roughening stabilises the crystal morphology. The results are interpreted in terms of a competition between 2D nucleation at the edges of the crystal and step flow on its surface. In this, surface protein concentration

profiles derived from observed crystal shapes are used.

8.1   Introduction

X-ray diffraction (XRD) is the main route towards structure determination of protein macromolecules. The success of structure determination by this method depends on the quality of the protein crystal, which is typically grown from an aqueous solution. In screening experiments for successful crystallisation conditions, poly(ethylene-glycol) (PEG) is often used as a precipitating agent additional to salts[1–4]. The addition of PEG reduces the solubility of proteins by steric exclusion[5] and thus stimulates nucleation and growth. The effectiveness of the added PEG depends on the concentration and its molecular weight[6, 7].

Besides acting as a precipitating agent, PEG also lowers the diffusion coefficient for proteins in the solution[8]. The rate of diffusion is relevant in crystal growth systems in which natural convection is reduced, for instance experiments in microgravity[9], using nanoliter volumes[10, 11], using gels[12–14], and damping of convection by magnetic fields[15]. Such systems are of interest because convection is thought to have a negative influence on crystal quality as it is an effective means for impurities to be transported towards the crystal surface[16].

Mass transport towards the crystal surface and surface kinetics (i.e. surface diffusion and incorporation of growth units) together determine the growth rate of the crystal. In convective systems mass transport is generally faster than surface kinetics, and surface kinetics is the rate limiting step. In systems where diffusion, which is typically two orders of magnitude slower than convection[17], is the sole means of mass transport, this balance is shifted towards equal contributions or even towards mass transport limitation. As a result, local differences in surface concentration are not compensated anymore by surface kinetics and the crystal looses its faceted form and becomes hopper shaped or grows in a dendritic fashion; in other words, the crystal looses its morphological stability[18, 19]. The occurrence of such instabilities not only

depends on the balance between diffusion and surface kinetics, but also on crystal size and supersaturation[20]. In protein crystal growth, surface kinetics are generally very slow[21, 22] and, for instance, lysozyme crystals grown under typical circumstances are expected to be stable up to 2-4 cm in size[23], which is very large for protein crystals. The occurrence of morphological instability is relevant to protein crystal growth as it can cause striations and lattice defects which are detrimental to crystal quality[24–26].

In this paper, we present a study on the influence of PEG-4600 on the macroscopic morphological stability of tetragonal hen egg-white lysozyme crystals grown in thin cells ($\sim$100 μm), mimicking the nowadays often used crystallisation technique of nanoliter volumes[3, 10, 11] in combination with the use of precipitation enhancers. The growth kinetics of morphologically unstable HEWL crystals are studied by in-situ optical microscopy in a systematic screening of growth morphology for various combinations of PEG-4600 concentration, lysozyme concentration and temperature. We present a "stability diagram" in which the transition from faceted to unstable tetragonal lysozyme crystals, induced by the addition of PEG, is expressed in terms of supersaturation and the diffusion coefficient. The results are interpreted in terms of a competition between 2D nucleation at the edges of the crystal and step flow on its surface.

8.2 Experimental procedures

Chemicals of analytical grade were used in this study. A buffer stock solution of sodium acetate and acetic acid was made in deionised water ($>$15 MΩcm) to result in a 0.05 M NaOAc/HOAc solution of pH 4.5. HEWL from Sigma-Aldrich (lot nr. 094K1454) in buffer was used as source material for crystal growth after reducing the lower MW contaminants by dialysis (MWCO 8 kDa) against the buffer solution. MALDI-TOF measurements did not reveal contaminations of higher MW. NaCl stock solutions of 1.37 M were prepared in buffer solution, filtered over a 0.2 μm membrane (Schleicher & Schuell) and mixed with PEG-4600 (Sigma-Aldrich) to obtain twice the PEG

and NaCl concentration required in experiment. Lysozyme stock solutions and buffer solutions were filtered over a 0.2 membrane and mixed to obtain a solution containing twice the required HEWL concentration for the experiment. HEWL-buffer and NaCl-PEG-buffer solutions were mixed one-to-one prior to experiments. Thus, all experiments were performed in a 0.685 M NaCl (4%w/v) and 0.05 M NaOAc/HOAc solution of pH 4.5. We determined the pH to vary linearly with PEG concentration following pH=4.50+0.01·[PEG], with [PEG] in %w/v.

A 10 μl droplet of the resulting mother liquor is placed on a sapphire window and a cover-slide is placed on top. The droplet forms an approximately 100 μm thick layer and is sealed off at the sides by vacuum grease to prevent evaporation of the solution. The small spacing in the vertical direction prevents the formation of free convection patterns, and mass transport during crystal growth is only determined by diffusion[26]. The sapphire window is placed in a temperature controlled cell for in-situ microscopy. Using sapphire instead of regular glass ensures a better heat conductivity and thus better temperature control of the system. Experiments were performed at temperatures between 9 ^oC and 20 ^oC with an accuracy of 0.1 ^oC. The in-situ cell consists of a brass plate through which water from a thermostatically controlled reservoir can flow. The sample is placed on top of the brass plate and covered by another brass plate without water through-put. Holes in the middle of the two brass plates allow for optical transmission microscopy.

Series of time-lapse micrographs were made using an Olympus Vanox optical microscope in combination with a Nikon DS5M CCD camera. Image processing software (ImagePro Plus[27]) and Matlab[28] were used to automatically acquire the crystal size and shape from subsequent images of the time-lapse series.

8.3 Results and Discussion

8.3.1 Morphological instability

In figure 8.1 a series of photographs shows a typical morphologically unstable growth experiment, performed at 10.5 ^oC with 30 mg/ml HEWL and 10% w/v PEG-4600. The images show a tetragonal lysozyme crystal viewed along its c-axis, which is also the four-fold symmetry axis of its $P4_32_12$ crystal structure; the sides are the {110} faces. In the first image of the experiment, about 4 minutes after placing the sample in the temperature controlled cell, the crystal is approximately 20 by 20 μm and nicely faceted. After just a few minutes, when the crystal is approximately 30 by 30 μm in size, it starts to loose its morphological stability. The crystal grows faster at the corners than in middle of the {110} side faces, which become concave and have re-entrant corners appearing in the middle.

The development of morphological instability is a result of an inhomogeneous concentration distribution at the crystal surface. For a square crystal growing from solution (figure 8.2a), experiment[29], conformal transformation [30] and numerical simulations [20] show that the concentration profile is approximately circular, and intersects the crystal surface. As the growth rate of a crystal depends on the surface concentration, the corners grow faster than the middle of the crystal faces (figure 8.2b). Thus, the morphological instability is the result of a square crystal being present in an approximately circular concentration field. Therefore, this kind of instability is also called polyhedral instability and is different from the instability due to perturbations as described by Mullins and Sekerka[31, 32].

Polyhedral instability can be regarded as the result of the competition between 2D nucleation of islands near the edges and corners of the surface and the subsequent spread of these islands over the crystal surface. For a small crystal the supersaturation difference between edge and middle of the surface is small, and 2D nucleation, exponentially dependent on the supersaturation, is much slower than step flow over the surface, which changes approximately linearly with supersaturation. While the crystal grows, the supersaturation
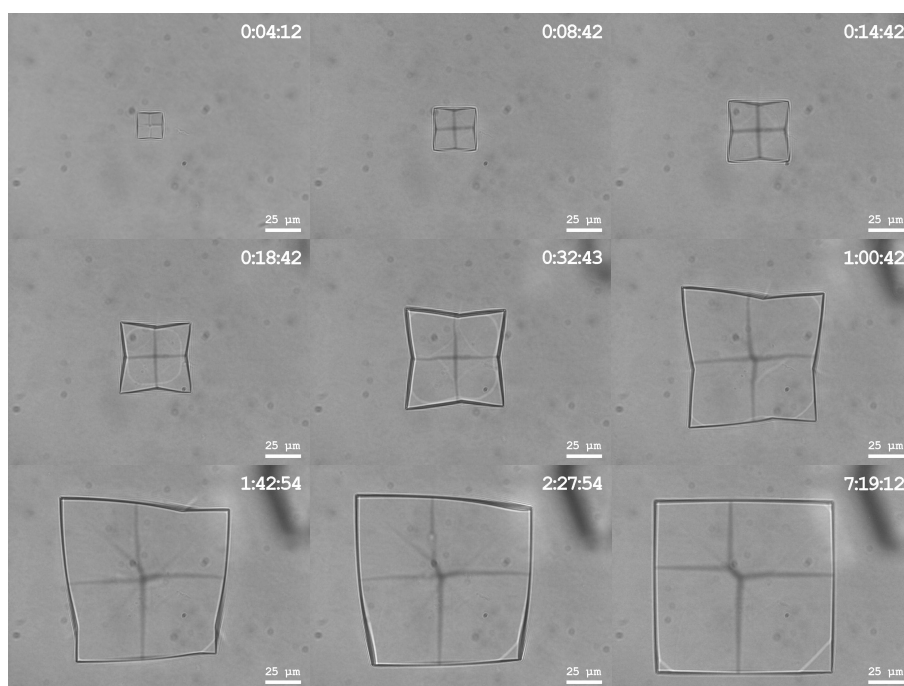
Figure 8.1: Series of images of a tetragonal hen egg-white lysozyme crystal which becomes morphologically unstable, but in the end regains its stability due to the exhaustion of the mother liquor. The time in the upper right corner of the images indicates hours, minutes and seconds since the sample was placed in the temperature controlled cell at 10.5 ^{o}C. The initial mother liquor consists of 30 mg/ml HEWL, 0.685 M NaCl, 10 % w/v PEG-4600 and 0.05 M NaOAc/HOAc buffer of pH 4.5. The scalebars indicate 25 μm.
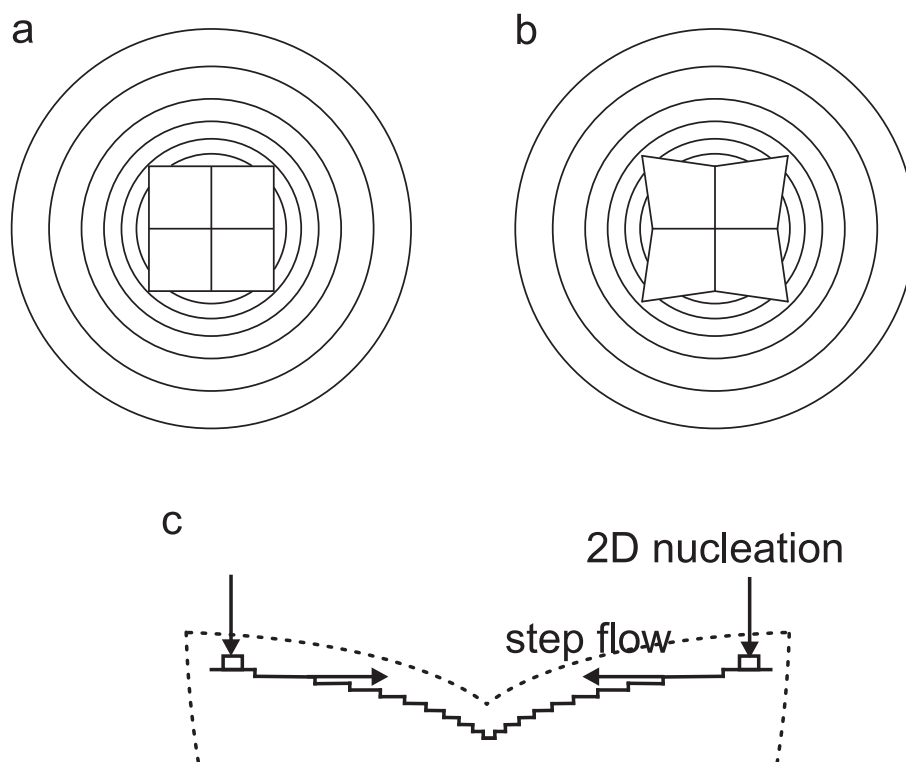
Figure 8.2: a) Schematic representation of the concentration profile around a growing tetragonal lysozyme crystal, viewed along its *c*-axis. The iso-concentration lines intersect the crystal surface. b) As a result, the edges and corners grow faster than the middle of the crystal faces. c) Principle of the morphologically unstable growth, resulting from the competition of 2D nucleation at the corners and edges due to the locally high supersaturation and subsequent step flow toward the middle. The dashed line indicates the macroscopic continuous crystal shape made up of microscopic, discrete steps.

difference between edge and middle becomes larger until at some point at the edges and corners new islands are formed faster than the previous ones completely cover the surface (figure 8.2c). As a result, the corners and edges of the crystal grow faster than the face centres and the crystal morphology becomes unstable.

Due to the finite supply of lysozyme molecules in the closed system, in the long run the overall solute content and thus the surface concentration drops. The supersaturation decreases and the crystal regains its morphological stability (figure 8.1) because the step flow is now faster again than 2D nucleation. This leads to a square, faceted crystal shape at the end of the experiment. In this later stage of growth, the crystal as a whole first develops in a slightly asymmetric fashion due to the presence of other crystals in its surroundings. This asymmetry, like the instability, is corrected when the surface supersaturation drops. However, the temporary asymmetry in the supply of lysozyme molecules to the crystal remains visible in the size difference of the {101} faces, as can often be encountered in lysozyme crystal growth experiments at higher supersaturation.

8.3.2 Stability diagram

To investigate the conditions at which growing tetragonal lysozyme crystals experience morphological instability, temperature, PEG-4600 concentration and lysozyme concentration were varied. Crystals were observed during growth by optical microscopy to check if they develop any instability. As the instability of a crystal partly depends on its size, a crystal might become unstable at larger sizes than observed during experiment. However, depending on starting conditions, on average a certain number of crystals will nucleate per unit volume, and deplete the solution while growing. Thus, depending on the starting conditions, the crystals have a certain maximum size depending on the available material. We call a condition "stable" if during the experiment, i.e. from nucleation to growth cessation, crystals do not show instability. The initial conditions for which morphologically unstable growth occurs are shown in the "stability diagram" of figure 8.3a.
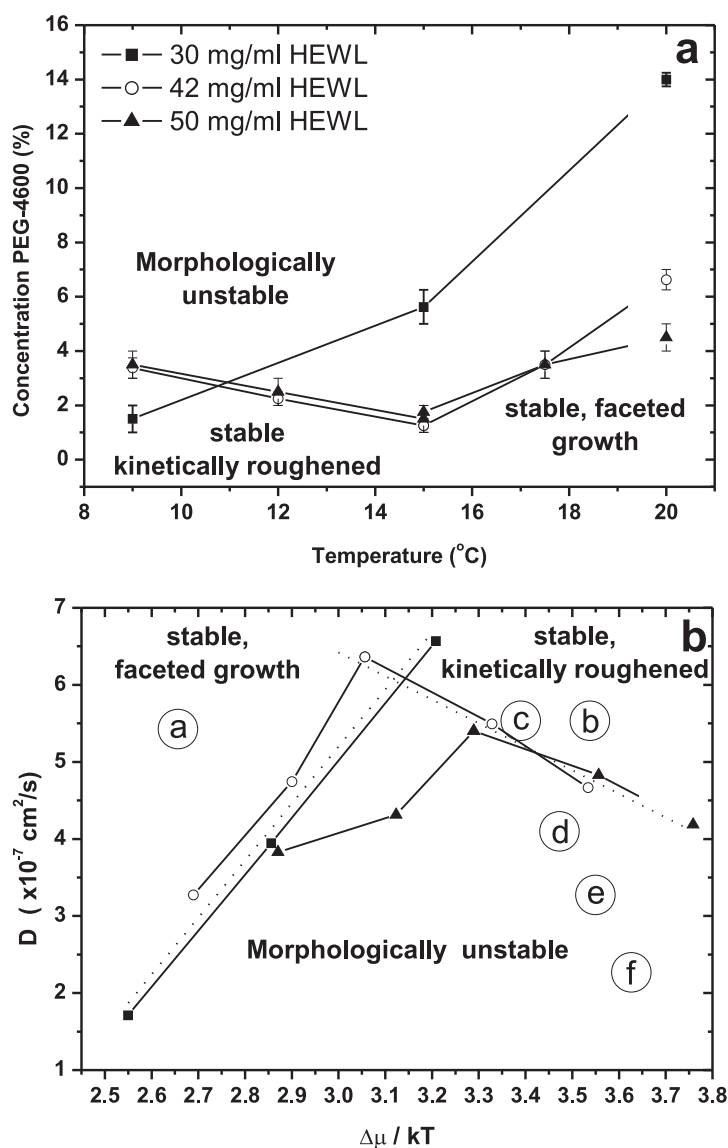
Figure 8.3: a) Instability diagram for the HEWL/NaCl/PEG-4600 system, with 0.685 M NaCl and 0.05 M NaOAc buffer solution at pH 4.5. b) Same data as in panel a, but now in terms of diffusion coefficient and driving force. The letters correspond to the panels of figure 8.4 showing crystals grown at these conditions.

In the stable region, lysozyme crystals develop as polyhedral crystals, with well-defined {110} and {101} faces (figure 8.4a). Increasing temperature, PEG-4600 concentration, lysozyme concentration or any combination of these parameters, brings the system into the unstable region. While in the unstable zone, the extent of instability depends on the conditions' distance to the stable zone. Figures 8.4d up to f show unstable lysozyme crystals at increasingly destabilising conditions. Figure 8.4f is close to growth in a dendritic fashion, as the reentrant corners suffer from a severe lack of growth units.

A third region at higher supersaturation is present in which the crystals are neither faceted nor unstable, but kinetically rough[33] (see figures 8.4b and c). Kinetically rough growth is a result of a high driving force, which reduces the critical nucleus size for 2D nucleation to equal or below the size of one growth unit[34]. As a result, the anisotropy in growth rates normally resulting in the formation of facets disappears and the surfaces get rounded and convex. Due to the rounded shape -which in some cases is even almost cylindrical, as shown in figure 8.4b*- polyhedral instability is reduced.

Although for practical purposes figure 8.3 suffices, for comparison of mass transport and surface kinetics conditions, one would like to have the stability as function of diffusion coefficient, driving force and crystal size instead of PEG concentration and temperature. In our experiments we usually find that instability starts to develop when the crystals have a size of 20 to 30 μm. The driving force for crystallisation is given by

$$\frac{\Delta\mu}{kT} = \ln\frac{c}{c_{\text{eq}}} \; , \tag{8.1}$$

in which c is the lysozyme concentration, and c_{eq} the equilibrium lysozyme concentration under given conditions. To convert lysozyme concentration to driving force, we use literature data on the equilibrium concentration at various temperatures for lysozyme in solutions as used in our experiments[35]. These data do not include added polyethylene-glycols. The equilibrium concentration

---

*The {101} faces have different step energy and thus kinetic roughening sets on at a higher driving force.
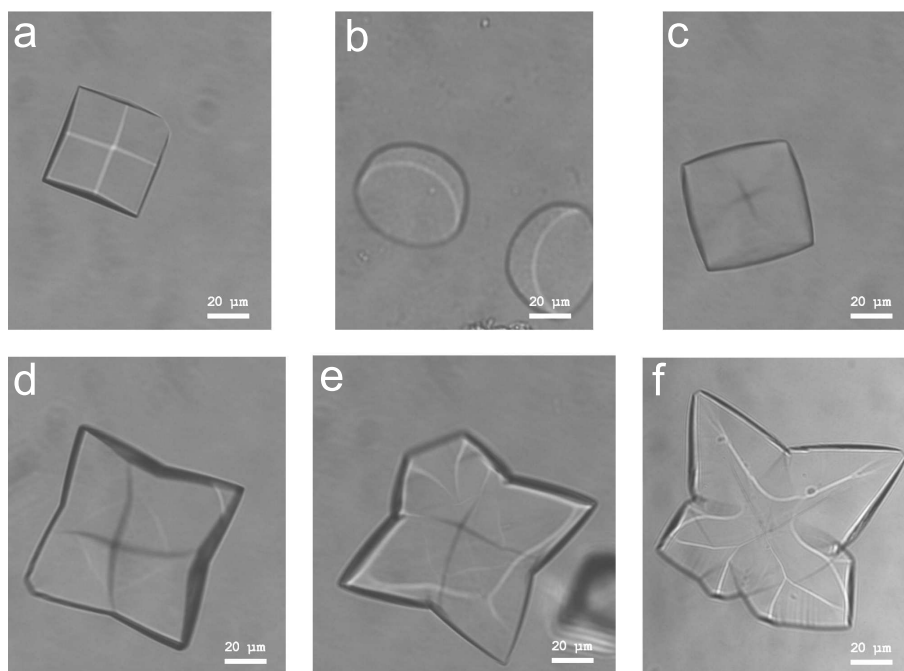
Figure 8.4: Examples of tetragonal lysozyme crystals grown under different conditions, all from a 0.685 M NaCl/0.05 M NaOAc buffer solution of pH 4.5. The scalebars indicate 20 μm. a) stable growth at 50 mg/ml HEWL, 0 %w/v PEG-4600 and 20 ^{o}C. For panels b up to e conditions are identical, 50 mg/ml and 9 ^{o}C, except for an increase in PEG-4600 concentration. b) kinetically rough growth at 0 %w/v PEG-4600. c) kinetically rough growth at 2 %w/v PEG-4600. d) morphologically unstable growth at 5 %w/v PEG-4600. e) morphologically unstable growth at 10 %w/v PEG-4600. f) morphologically unstable growth at 40 mg/ml HEWL, 25 %w/v PEG-4600 and 20 ^{o}C.

varies with PEG-concentration as well, and its dependence is given by[6]

$$\ln c_{\mathrm{eq}} = \ln c_{\mathrm{eq},0} - K[\mathrm{PEG}] \; , \tag{8.2}$$

in which $c_{\mathrm{eq},0}$ is the equilibrium concentration without PEG added, [PEG] the polyethylene-glycol concentration in % w/v, and K a proportionality constant. We determined K by solubility experiments to be approximately 0.02.

The diffusion coefficient of lysozyme changes with the addition of polyethylene-glycols[8], but also decreases with increasing lysozyme concentration[36]. The dependency of the diffusion coefficient on lysozyme concentration is given by[36]

$$D = D_0 \left[1 + k_D \phi \right] \; , \tag{8.3}$$

where ϕ is the volume fraction of lysozyme, k_D the diffusivity slope, and D_0 the single particle diffusion coefficient. The diffusivity slope depends on the exact solvent composition, i.e. both sodium acetate concentration and sodium chloride concentration. In our calculations we use the value -12.1 for 0.427 M NaCl as an upper limit as the slope k_D is expected to be slightly steeper for 0.685 M. Thus, the diffusion constant for higher lysozyme concentration is slightly overestimated, and mass transport is even slower. To include the effect of PEG-4600 on the diffusion constant, we use data on the reduced viscosity of PEG-4000 in water[5]. The effect of PEG on diffusion is mainly an effect of increase in viscosity[8]. The single particle diffusion D_0 is related to the dynamic viscosity through the Stokes-Einstein relation

$$D_0 = \frac{k_B T}{6 \pi \eta a_H} \; , \tag{8.4}$$

where η is the dynamic viscosity of the solvent, and $a_h \sim 1.7$ nm the hydrodynamic radius of a lysozyme molecule[37]. As an approximation we consider the added PEG-4600 to change the viscosity in equation 8.4, and thus also D_0 in equation 8.3. In this way, the diffusion coefficient is calculated using lysozyme concentration and PEG-4600 concentration. The appropriate driving forces and diffusion coefficients determined in this way are used in the stability diagram of figure 8.3b.

The stability diagram of figure 8.3b suggests that a simple, empirical criterion based on diffusion coefficient and driving force should be indicative of the polyhedral stability of tetragonal lysozyme crystals. The diffusion coefficient indicates the speed of the mass transport process, while the initial supersaturation determines the maximum growth rate of the crystal. From experiments, we find a stability criterion

$$\xi = \frac{-17 + 7.4 \times \Delta\mu/kT}{D \times 10^7} \ , \tag{8.5}$$

where D is the diffusion coefficient in cm^2/s. For $\xi < 1$, crystals can be expected to retain their stability, while for $\xi > 1$ the balance between surface kinetics and transport will induce morphological instability. It should be realised that the above mentioned stability criterion only holds for the present growth system. Changing the type of salt may result in different polymorphs, which have different energetics, and even changing salt concentration may change the polymorph[38] and growth mode[33].

The stability criterion for kinetically roughened crystals is very different from the faceted ones, being

$$\zeta = \frac{16 - 3.1 \times \Delta\mu/kT}{D \times 10^7} \ . \tag{8.6}$$

Here, the factor before $\Delta\mu/kT$ is now *negative*, i.e. morphological stability increases for increasing supersaturation. This effect, which is surprising, can be understood in terms of the polyhedral nature of the instabilities. Slightly rounded crystals will experience a lower supersaturation difference than properly faceted crystals, because the surface more closely follows the cylindrical concentration profile. For a rounded, cornerless crystal obtained at the highest $\Delta\mu/kT$, no supersaturation difference between corner and middle can even exist.

8.3.3 Dynamic aspects

As is clear from the series of images of figure 8.1, morphological instability is a transient state. Series of images like those of figure 8.1 offer the possibility to acquire quantitative data on growth rates and stability of lysozyme
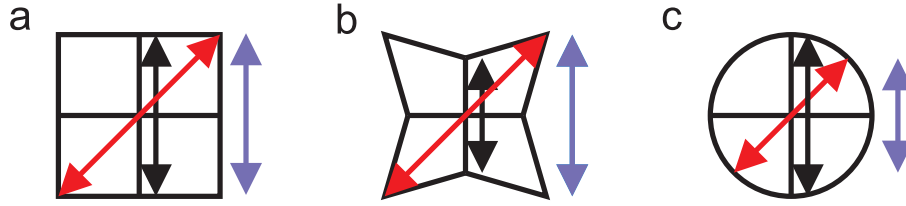
crystals. Figure 8.5a shows the corner-to-corner distance and the middle-to-middle distance of the crystal in figure 8.1. These are determined by using the software program ImagePro Plus to automatically acquire the maximum and minimum diameter of the crystals in the optical images, as indicated by the red and black arrows respectively in figure 8.6. From the maximum diameter the corner-to-corner distance is derived by using Pythagoras' theorem (blue arrows in figure 8.6). The solid line in figure 8.5a indicates the ratio between middle-to-middle and corner-to-corner distance. This ratio in combination with its time-derivative is a benchmark for the stability of the crystal. A ratio of one indicates a square crystal (figure 8.6a). If the ratio is smaller than one (figure 8.6b) and decreasing, the crystal is morphologically unstable. If the ratio is smaller than one but the ratio increases, the crystal is stable and recovering its square form. Using the method of the minimum and maximum diameter has the extra benefit that kinetic roughness can also be adjudicated by this ratio, as for circular crystal shapes and square crystals with rounded corners it is larger than one (figure 8.6c).

In the example of the experiment of figure 8.1, the stability of the crystal decreases up to 55 minutes after the start of the experiment. At this point, the growth rates of the face centres become larger than those of the corners (figure 8.5b), and the stability ratio increases as the crystal regains its stability. Theoretically, the instability should increase while the crystal continues to grow. However, the growing crystal and also other crystals nucleated in the solution deplete their surroundings from lysozyme molecules. When the diffusion field of a crystal starts to overlap with that of neighbouring crystals, the growth rate drops. This moment coincides with the minimum in the instability ratio after which the stability is regained (dashed line in figure 8.5a). The growth rates indicate diffusion limitation before the 55 minute mark following a $1/\sqrt{t}$ dependence (dashed line in figure 8.5b), but continue to drop faster due to the depletion.

Kinetic data were taken by the described method from series of images of crystals growing under various conditions for a lysozyme concentration of 42 mg/ml (figures 8.7 and 8.8). Figure 8.7 shows corner-to-corner size and stabil-
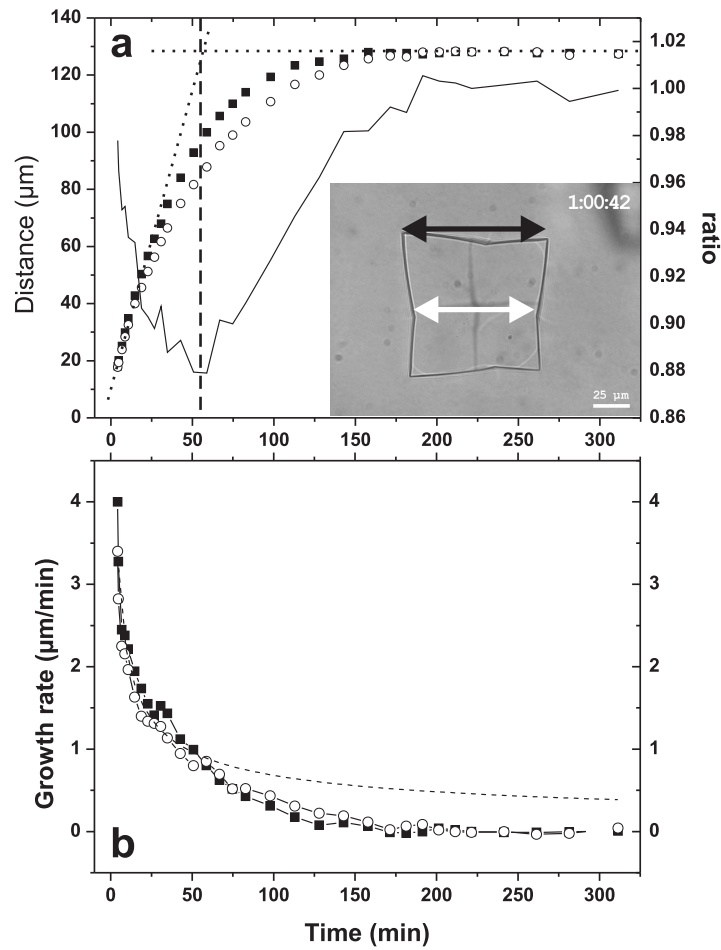
Figure 8.5: Growth data taken from the series of images in figure 8.1. (a) Squares indicate the distance between the top left and top right corner as indicated by the black arrow in the inset. Circles indicate the distance from the middle of the left (110) face to the right (110) face (white arrow in inset). The solid line depicts the ratio between corner-to-corner and middle-to-middle distance indicating instability when decreasing and smaller than 1. The dotted lines are slopes of the growth curve, the intersection of which indicates the moment at which the growth rate drops due to overlapping diffusion fields. (b) Growth rates of the corners (squares) and middle (circles) of the {110} faces. The dashed line indicates a $1/\sqrt{t}$ fit.

Figure 8.6: Schematic representation of the automatic acquisition of the dimensions of a crystal. The maximum (red arrows) and minimum diameter (black arrows) are acquired from the images. Via Pythagoras' theorem, the "corner-to-corner" distance is determined (blue arrows). The stability ratio is equal to the ratio between red, L_{centre}, and blue, L_{corner}, arrows. (a) The instability ratio is equal to 1 for stable crystals. (b) The instability ratio is smaller than 1 for morphologically unstable crystals. (c) For kinetically rough crystals the ratio is larger than 1.

ity ratio for experiments at 5 %w/v PEG and 10 %w/v PEG for temperatures ranging from 9 ^{o}C to 21 ^{o}C. Because the diffusion coefficient is only slightly temperature dependent, these data can be considered as function of $\Delta\mu/kT$. For 5 %w/v PEG the diffusion coefficient is approximately 3.7×10^{-7} cm^2/s, while for 10 %w/v PEG the diffusion coefficient is approximately 2.1×10^{-7} cm^2/s. For unstable crystals at 10 %w/v PEG, it takes longer to regain their stability than at 5%w/v PEG. Also, the ratio shows a slightly higher instability. At both PEG concentrations, crystals in the lower supersaturation experiment (i.e. higher temperatures) continue to grow for a longer time and to a larger size than crystals at high supersaturation. At high supersaturation, not only the growth rate but also the 3D-nucleation rate is high compared to low supersaturation. A higher number of crystals in the system speeds up the process of depletion of the mother liquor and thus the moment at which diffusion fields start to overlap.

Figure 8.8 shows size and stability ratio for experiments at 9 ^{o}C and 15 ^{o}C for PEG concentrations ranging from 0 %w/v to 10 %w/v. At higher PEG concentrations the crystals are polygonized and behave in the same way as those shown in figure 8.7. As the diffusion coefficient is lowered and $\Delta\mu/kT$
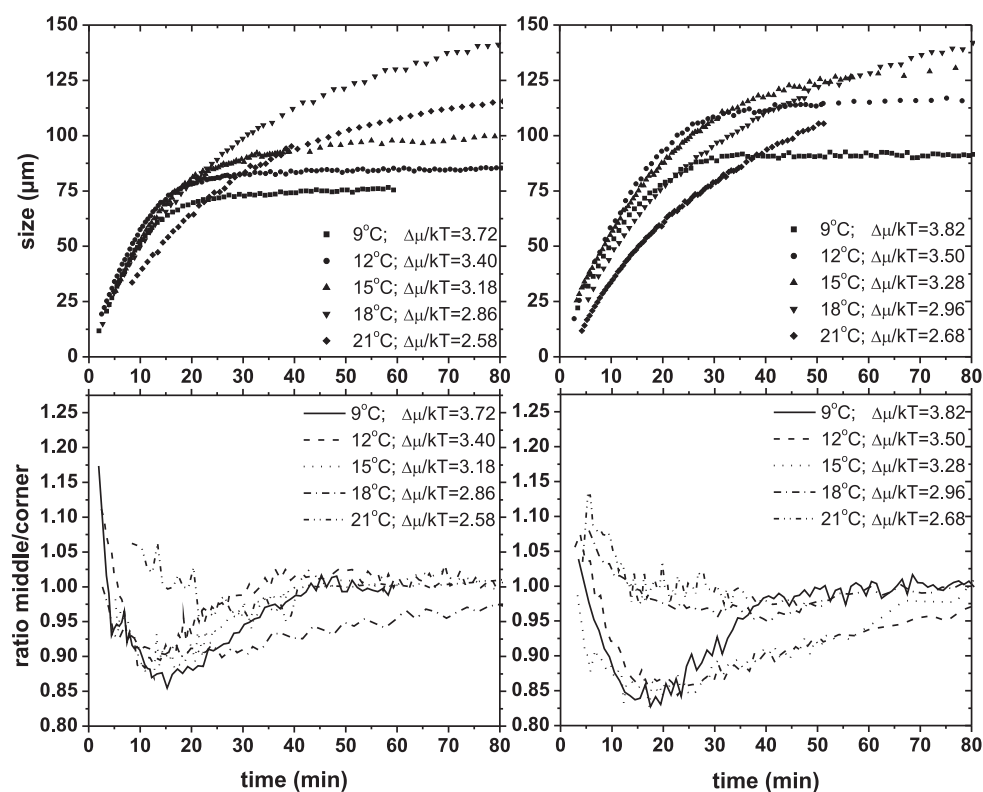
Figure 8.7: Kinetic data for 42 mg/ml HEWL, 0.685 M NaCl, 0.05M NaOAc/HOAc, pH 4.5, 5%w/v PEG-4600 (left column) and 10 %w/v PEG-4600 (right column) at various temperatures. The top row shows the corner-to-corner distance. The bottom row shows the instability ratio (see text).
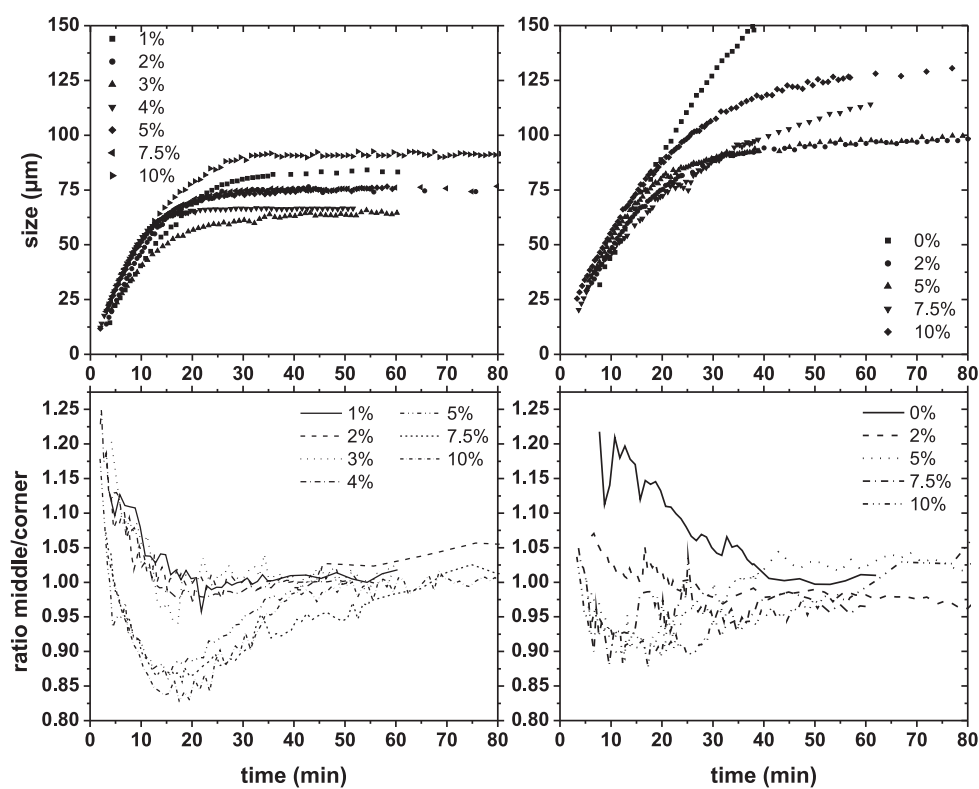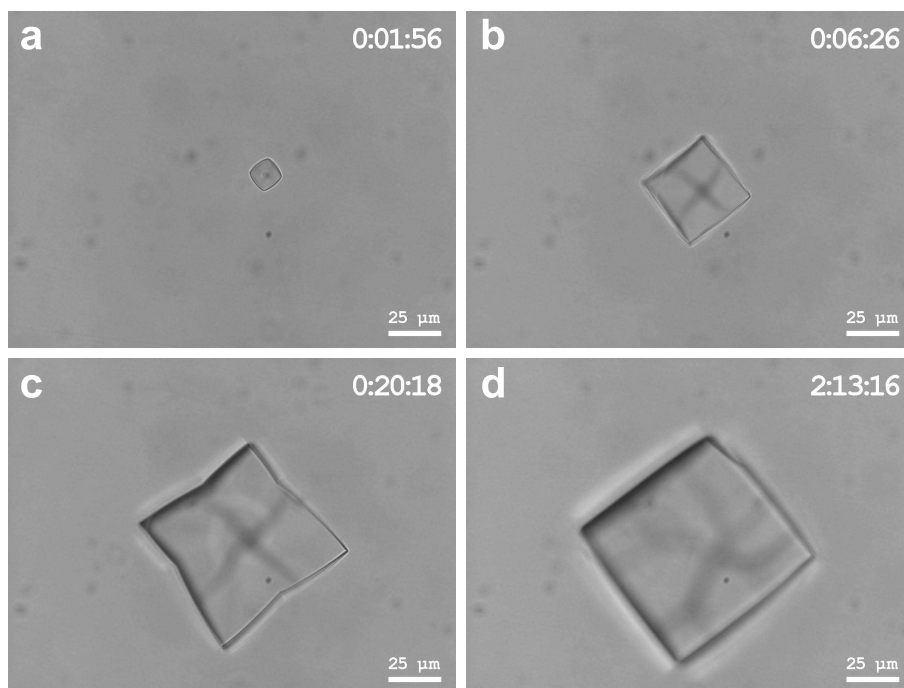
Figure 8.8: Kinetic data for 42 mg/ml HEWL, 0.685 M NaCl, 0.05M NaOAc/HOAc, pH 4.5 and various PEG concentrations at 9°C (left column) and at 15°C (right column). The top row shows the corner-to-corner distance. The bottom row shows the instability ratio (see text).

is increased, we expect a higher degree of morphological instability at these conditions. Experimental data show a general trend following this concept, but in detail are not consistent as a consequence of the 3D-nucleation effect as described above. Crystals grown at 15 ^oC continue to grow to larger sizes than crystals grown at 9 ^oC, confirming the influence of nucleation on growth kinetics (fig. 8.8). However, at lower PEG concentrations the situation is different. Here the crystals were found to be kinetically rough, resulting in a stability ratio larger than one. Thus, in general, crystals starting out rough stay stable throughout the experiment (figure 8.8, 9 ^oC, 1-4%w/v PEG, and 15 ^oC, 0 and 2%w/v PEG). In some experiments, at the rough-unstable transition line, the crystals start out slightly rough, develop facets as the supersaturation drops and enter in the polyhedral instability region and loose their stability (figure 8.9). In the end the solution is depleted and the crystal changes back to its faceted shape, thus having progressed through all morphological stages. The morphological changes are reflected in the stability ratio which starts at 1.18, drops to 0.88 and ends up at 1.0 (figure 8.8: 9^oC and 5% PEG).

In general, the shape of crystal, i.e. being faceted or being rounded due to roughening, appears to have a larger influence on the morphological stability than variations in $\Delta\mu$ and D.

8.3.4   2D nucleation versus step flow

To investigate qualitatively the influence of the finite dimensions of the crystal and its environment on the kinetics of a growing lysozyme crystal and its stability, we use a model based on the 2D nucleation rate and step velocity. At high supersaturations the formation of new layers occurs via "Birth and Spread", i.e. 2D nucleation and subsequent spread of the 2D islands over the crystal surface. Because the surface concentration for a polyhedral crystal is higher at its corners than in the middle, 2D nuclei are mainly formed at the corners. From here the layers spread out towards the middle of the crystal face (figure 8.2c). For a crystal to maintain its polyhedral shape, the average time for a new layer to nucleate should be at most equal to the time it costs for such a layer to cover the crystal surface. If nucleation of a new layer is

Figure 8.9: Tetragonal lysozyme crystal growing from a 42 mg/ml HEWL, 0.685 M NaCl, 0.05 M NaOAc/HOAc solution of pH 4.5 with 5 % PEG at 9 ^{o}C. The crystal starts out kinetically rough (panel a), changes to faceted growth (panel b), subsequently looses its morphological stability (c), and in the end regains its stable, faceted shape (d). The scalebars indicate 25 μm.

faster, the corners will grow faster than the middle.

Thus, the shape of the crystal is determined by the balance between 2D nucleation at the edges and corners of the crystal and step flow at the face centre. Using this concept, we can perform the following analysis to find a relation between the local supersaturation and the local slope of the crystal surface. The step flux is constant over the surface and is equal to the nucleation rate, i.e. $J_{st} = J_{nucl}$. The step flux J_{st} is the number of steps passing the crystal surface at each point x per unit time, and is the product of step velocity $v_{st}(x)$ and the step density $\phi_{st}(x)$, which is the number of steps per unit length:

$$J_{st} = v_{st}(x) \cdot \phi_{st}(x) \ . \tag{8.7}$$

The step speed is given by

$$v_{st}(x) = \beta_{st} \cdot \sigma(x) \ , \tag{8.8}$$

in which β_{st} is the step kinetic coefficient, which we presume to be independent of step spacing. These two equations can be used to find an expression for the step density depending on nucleation rate and supersaturation:

$$\phi_{st}(x) = \frac{J_{nucl}}{\beta_{st} \, \sigma(x)} \ . \tag{8.9}$$

Since the local slope of the surface, $p(x)$, is determined by the step density and the step height h_{st}, i.e. $p(x) = \phi_{st}(x) \cdot h_{st}$, we now obtain an expression for the local slope

$$p(x) = \frac{J_{nucl} \, h_{st}}{\beta_{st} \, \sigma(x)} \ . \tag{8.10}$$

The nucleation rate can be found by using the growth rate of the crystal at the corner, as the number of new layers is equal to the growth rate normal to the surface divided by the height of one layer, $J_{nucl} = R_{corner}/h_{st}$. Thus, we find an expression for the local supersaturation as function of the local slope and the growth rate at the corner:

$$\sigma(x) = \frac{R_{corner}}{\beta_{st}} \cdot \frac{1}{p(x)} \ . \tag{8.11}$$

This expression can be used in analysing surface profiles taken from experiment. Figure 8.10a shows a time-lapse series of surface profiles of a morphologically unstable lysozyme crystal, and figure 8.10b shows the corresponding supersaturation profiles $\sigma(x) \cdot \beta_{\mathrm{st}}$, which is identical to $R_{\mathrm{corner}}/p(x)$. Determination of the actual supersaturation value $\sigma(x)$ is not possible as the step kinetic coefficient is not known. However, the supersaturation profiles are consistent within the experiment. Using equation 8.11, we find that the average supersaturation drops more than a factor of 10 during this growth run, whereas the supersaturation ratio between corner and middle of the crystal face remains roughly a factor two. The dotted line shows a typical surface profile for a square crystal growing by 2D nucleation as calculated using the finite differences method. When the stability is regained, the experimental supersaturation profiles have a shape similar to this calculated profile, which is typical for stable growth.

In section 8.3.3 we defined an instability criterion based on the ratio between the surface centre-to-centre distance L_{centre} and the corner-to-corner distance L_{corner}. If growth is unstable this ratio decreases, and vice versa. An expression for this ratio can be given by

$$\frac{L_{\mathrm{centre}}}{L_{\mathrm{corner}}} = \frac{L_{\mathrm{corner}} - 2\lambda h_{\mathrm{st}}}{L_{\mathrm{corner}}} = 1 - \frac{2\lambda h_{\mathrm{st}}}{L_{\mathrm{corner}}} \;, \tag{8.12}$$

in which λ is the number of steps the centre lags behind the corner, and h_{st} the height of one step. Although the slope $p(x)$ is not constant along the crystal surface, an average slope can be defined based on the corner-to-corner distance and the lag at the centre of the crystal surface:

$$\bar{p}(x) = \frac{\lambda h_{\mathrm{st}}}{\frac{1}{2} L_{\mathrm{corner}}} \;. \tag{8.13}$$

Substitution into equation 8.12 gives $L_{\mathrm{centre}}/L_{\mathrm{corner}} = 1 - \bar{p}(x)$. The change in $L_{\mathrm{centre}}/L_{\mathrm{corner}}$ with time, i.e. $\mathrm{d}(L_{\mathrm{centre}}/L_{\mathrm{corner}})/\mathrm{d}t$, is given by $-\mathrm{d}\bar{p}(x)/\mathrm{d}t$.
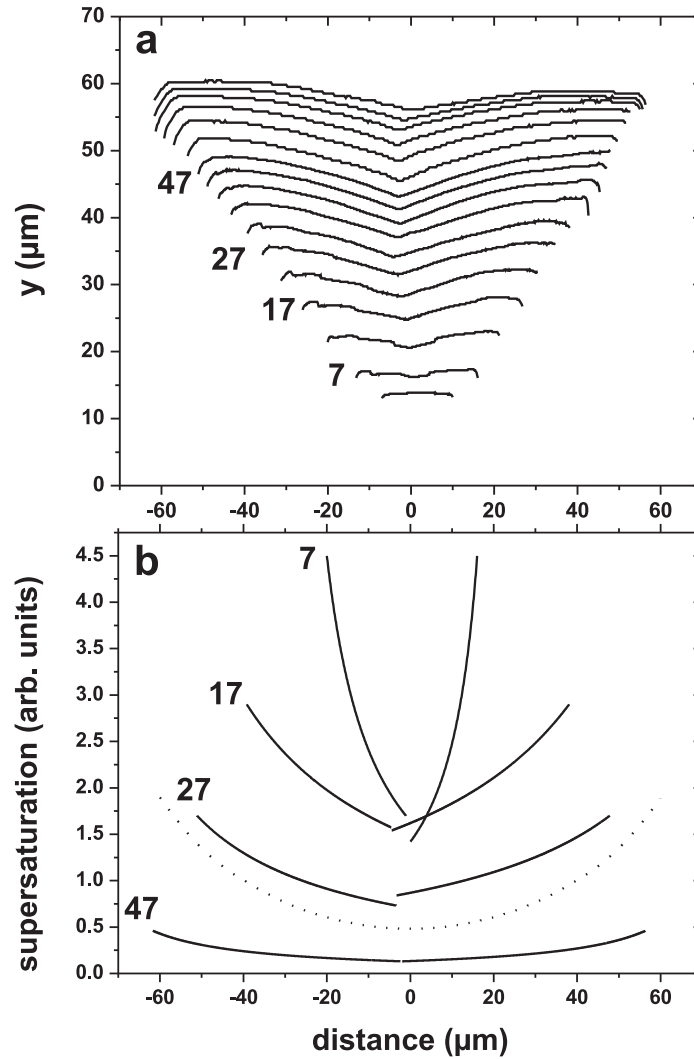
Figure 8.10: (a) Surface profiles extracted from time-lapse series of microscope images of a growing lysozyme crystal at 5 %w/v PEG-4600 and 18 ^{o}C. Interval between succesive lines is approximately 5 minutes. (b) Relative supersaturation σ, proportional to $R_{\text{corner}}/p(x)$, derived from the surface profiles of panel (a) and the growth rate at the corner of the crystal. The dotted line indicates a typical surface profile of a square crystal growing by 2D nucleation, calculated by finite elements. The numbers indicate time in minutes.

In combination with equation 8.10 this results in

$$\frac{d\left(\frac{L_{\text{centre}}}{L_{\text{corner}}}\right)}{dt} = -\frac{h_{\text{st}}}{\beta_{\text{st}}}\frac{d\left(J_{\text{nucl}} < \frac{1}{\sigma(x)} >\right)}{dt}$$

$$= -\frac{h_{\text{st}}}{\beta_{\text{st}}}\frac{d\left(J_{\text{nucl}}/\sigma_{\text{avg}}\right)}{dt} , \tag{8.14}$$

with σ_{avg} is $< 1/\sigma(x) >^{-1}$. For 2D nucleation the supersaturation dependent nucleation rate is approximated by[39]

$$J_{\text{nucl}} \cong A'(v_{\text{step}})_{\text{corner}} \exp\left\{-\frac{B}{\Delta\mu_{\text{corner}}/kT}\right\}$$

$$= A'\beta_{\text{st}}\sigma_{\text{corner}} \exp\left\{-\frac{B}{\ln(\sigma_{\text{corner}}+1)}\right\} , \tag{8.15}$$

with A' and B supersaturation independent coefficients, and σ_{corner} the supersaturation at the corners of the crystal. Thus, by combining equation 8.14 and 8.15 the change in (in)stability ratio becomes

$$\frac{d\left(\frac{L_{\text{centre}}}{L_{\text{corner}}}\right)}{dt} = -\frac{d\left(A\frac{\sigma_{\text{corner}}}{\sigma_{\text{avg}}}\exp\left\{-\frac{B}{\ln[\sigma_{\text{avg}}+1]}\right\}\right)}{dt} . \tag{8.16}$$

Evaluating equation 8.16 in combination with figure 8.10 we find three regions of interest. For small crystals, i.e. at the start of the experiment, the surface profile is a straight line without a cusp (bottom profile in fig. 8.10a), indicating that $\sigma_{\text{corner}} \approx \sigma_{\text{avg}}$. 2D nucleation occurs on the whole crystal surface, which is planar. Next, the crystals become larger and as a result the ratio $\sigma_{\text{corner}}/\sigma_{\text{avg}}$ increases, while the change in the exponential term does not play a role yet. The ratio $L_{\text{centre}}/L_{\text{corner}}$ decreases, which indicates loss of stability. During continued growth of the crystals, the overall concentration in the finite system goes down and as a result also the surface concentration decreases. Now the exponential term in equation 8.16 plays a major role as its value drops rapidly and $d(L_{\text{centre}}/L_{\text{corner}})/dt$ becomes positive, which makes the ratio $L_{\text{centre}}/L_{\text{corner}}$ going back to 1. Thus, stability is regained even though the ratio $\sigma_{\text{corner}}/\sigma_{\text{avg}}$ remains larger than 1. In the end the system is depleted from growth units and the surface concentration drops to the region of spiral growth, in which the crystal finds its stable form[20].

8.4 Conclusions

Polyhedral instability for lysozyme crystals was previously estimated to occur for crystals larger than 2 cm. We have shown that by the addition of PEG-4600 the balance between surface kinetics and mass transport can be shifted such that instability occurs for crystals a mere 30 μm in size. In-situ measurements using optical microscopy showed that the morphological stability of the crystals decreases for higher driving force and lower solute diffusion coefficients. However, if the crystal is kinetically roughened the situation differs and stability increases for increasing driving force, which can be explained by the rounded shape deviating from the polyhedral shape of the crystal. Due to the finite supply of lysozyme in the system crystals regain their stability, not revealing their history of instability. Thus, a look at crystals at the end of an experiment does not necessarily reveal any processes detrimental to crystal quality. Changing crystallization conditions during growth based upon in-situ observations may avoid the occurrence of morphological instability while retaining the high initial supersaturation needed for nucleation. A qualitative model based on the balance between 2D nucleation at the corners of the crystal and step velocity toward the middle explains the influence of mass transport on stability and shows the regain of stability when the supply of growth units runs dry.

References

[1] Luft, J.; Collins, R.; Fehrman, N.; Lauricella, A.; Veatch, C.; De-Titta, G. *J. Struc. Biol.* **2003,** *142,* 170-179.

[2] Hennessy, D.; Buchanan, B.; Subramanian, D.; Wilkosz, P.; Rosenberg, J. *Acta Crystallogr., Sect. D: Biol. Crystallogr.* **2000,** *56,* 817-827.

[3] Zheng, B.; Roach, L.; Ismagilov, R. *J. Am. Chem. Soc.* **2003,** *125,* 11170-11171.

[4] Cudney, R.; Patel, S.; Weisgraber, K.; Newhouse, Y.; McPherson, A. *Acta Crystallogr., Sect. D: Biol. Crystallogr.* **1994,** *50*, 414-423.

[5] Bhat, R.; Timasheff, S. *Protein Sci.* **1992,** *1*, 1133-1143.

[6] Atha, D.; Ingham, K. *J. Biol. Chem.* **1981,** *256*, 2108-2117.

[7] Vivarès, D.; Bonneté, F. *Acta Crystallogr., Sect. D: Biol. Crystallogr. 58*, 472-479.

[8] Vergara, A.; Capuano, F.; Paduano, L.; Sartorio, R. *Macromolecules* **2006,** *39*, 4500-4506.

[9] Kundrot, C.; Judge, R.; Pusey, M.; Snell, E. *Cryst. Growth Des.* **2001,** *1*, 87-99.

[10] Carter, D.; Rhodes, P.; McRee, D.; Tari, L.; Dougan, D.; Snell, G.; Abolac, E.; Stevens, R. *J. Appl. Crystallogr.* **2005,** *38*, 87-90.

[11] Cherezov, V.; Caffrey, M. *J. Appl. Crystallogr.* **2003,** *36*, 1372-1377.

[12] Robert, M.; Lefaucheux, F. *J. Cryst. Growth* **1988,** *90*, 358-367.

[13] Biertümpfel, C.; Basquin, J.; Suck, D.; Sauter, C. *Acta Crystallogr., Sect. D: Biol. Crystallogr.* **2002,** *58*, 1657-1659.

[14] Garcia-Ruiz, J.; Moreno, A.; Viedma, C.; Coll, M. *Mater. Res. Bull.* **1993,** *28*, 541-546.

[15] Poodt, P.; Heijna, M.; Tsukamoto, K.; de Grip, W.; Christianen, P.; Maan, J.; van Enckevort, W.; Vlieg, E. *Appl. Phys. Lett.* **2005,** *87*, Art. No. 214105.

[16] Snell, E.; Helliwel, J. *Rep. Progr. Phys.* **2005,** *68*, 799-853.

[17] Lin, H.; Rosenberger, F.; Alexander, J.; Nadarajah, A. *J. Cryst. Growth* **1995,** *151*, 153-162.

[18] Chernov, A. *J. Cryst. Growth* **1974,** *24-25*, 11-31.

[19] Wilcox, W. *J. Cryst. Growth* **1977,** *38,* 73-81.

[20] Kuroda, T.; Irisawa, T.; Ookawa, A. *J. Cryst. Growth* **1977,** *42,* 41-46.

[21] Vekilov, P.; Rosenberger, F. *J. Cryst. Growth* **1996,** *158,* 540-551.

[22] Heijna, M.; van den Dungen, P.; van Enckevort, W.; Vlieg, E. *Cryst. Growth Des.* **2006,** *6,* 1206-1213.

[23] Nanev, C.; Penkova, A. *J. Cryst. Growth* **2002,** *237-239,* 283-288.

[24] Wilcox, W. *J. Cryst. Growth* **1983,** *65,* 133-142.

[25] McEwan, A.; Ristic, R.; Shekunov, B.; Sherwood, J. *J. Cryst. Growth* **1996,** *167,* 701-708.

[26] Vekilov, P.; Alexander, J.; Rosenberger, F. *Phys. Rev. E* **1996,** *54,* 6650-6660.

[27] IMAGEPRO PLUS 4.5, MediaCybernetics.

[28] MATLAB 6.5 (Release 13), The MathWorks Inc.

[29] Berg, W. *Proc. R. Soc. London, A* **1938,** *164,* 79-95.

[30] Seeger, A. *Philos. Mag.* **1953,** *44,* 1-13.

[31] Mullins, W.; Sekerka, R. *J. Appl. Phys.* **1963,** *34,* 323.

[32] Mullins, W.; Sekerka, R. *J. Appl. Phys.* **1964,** *35,* 444.

[33] Gorti, S.; Forsythe, E.; Pusey, M. *Cryst. Growth Des.* **2004,** *4,* 691-699.

[34] van Veenendaal, E.; van Hoof, P.; van Suchtelen, J.; van Enckevort, W.; Bennema, P. *Surf. Sci.* **1998,** *417,* 121-138.

[35] Forsythe, E.; Judge, R.; Pusey, M. *J. Chem. Eng. Data* **1999,** *44,* 637-640.

[36] Muschol, M.; Rosenberger, F. *J. Chem. Phys.* **1995,** *103,* 10424-10432.

[37] Tanford, C. *Physical Chemistry of Macromolecules;* Wiley: New York, 1961.

[38] Heijna, M.; Theelen, M.; van Enckevort, W.; Vlieg, E. *J. Phys. Chem. B* **2007,** *111,* 1567-1573.

[39] van der Eerden, J. . In *Handbook of Crystal Growth*; Elsevier Science Publishers: Amsterdam, 1993.

Summary

Protein molecules play an important role in the machinery of life, participating in every process within cells. Knowledge of their three-dimensional structure can provide insight into the way they function and thus into the way life functions. X-ray diffraction (XRD) is the main route to determine the three-dimensional molecular structure of proteins. The success of this method depends on the availability of high-quality protein single crystals. Due to the wide variety of protein molecules a single recipe for the growth of XRD-quality crystals does not exist. To find the right crystallisation conditions for a given protein, one needs to perform an extensive screening of solution conditions. On the one hand, technology speeds up the process of finding the proper conditions using large-scale (automated) trial-and-error screening methods. On the other hand, understanding the fundamentals of the crystal growth processes can help in reducing the parameter space.

Crystal growth from solution, like protein crystal growth, can be regarded as a combination of two successive processes; mass transport of growth units toward the crystal, and incorporation of those growth units into the crystal, i.e. the surface kinetics. The growth rate of the crystal is determined by the slowest of these two processes. This thesis focuses on the balance between mass transport and surface kinetics in protein crystal growth, and aims to contribute to the understanding of these processes. Hen egg-white lysozyme (HEWL) is an often used test case for protein crystal growth experiments, and as a result literature on HEWL is widely available. To take advantage of this large base of knowledge, lysozyme is used in the studies on protein crystal growth in this thesis.

In chapter 2 and 3 the surface kinetics during growth of lysozyme crystals are investigated by using optical and atomic force microscopy. Atomic force microscopy reveals rounded, highly anisotropic spirals on the (001) surface of triclinic lysozyme. The sticking fraction for HEWL molecules to become attached to a kink site at a step on the (001) surface is significantly different from that of the orthorhombic lysozyme polymorph. The difference between lysozyme polymorphs is further investigated by optical microscopy in chapter 3. Series of time-lapse microscope images show different growth kinetics for different polymorphs. Depending on the symmetry of the polymorph the growth of one of a pair of opposite crystal faces is blocked. This effect may be attributed to the surface phenomenon of self-poisoning; molecules can metastably attach to the surface in the wrong orientation with respect to the crystal structure. Such an effect might explain why some proteins are notoriously difficult to crystallise.

Moving toward the subject of mass transport, in chapter 4 spherulitic growth of lysozyme crystals is investigated. Spherulites consist of a bundle of crystalline needles, which often are found in protein crystallisation processes and are usually discarded as they are useless for XRD structure determination. With respect to surface kinetics, a tip splitting mechanism is proposed for the formation of the characteristic sheave-like structure of the lysozyme spherulites. For the mass transport mechanism, growth kinetics indicate that for a single needle surface kinetics determine the overall growth process, but all needles together deplete the solution faster than mass diffusion can replenish.

Besides the separation into a diluted solution phase and a crystalline phase, a lysozyme solution has a third phase consisting of a dense liquid phase. The formation of this phase is called liquid-liquid phase separation. The dense liquid phase is dense to such an extent that a gel network is created. This gel prohibits the formation of crystals in the dense phase, thus leaving the nucleation to the dilute phase. When crystals have formed, a three-phase system exists consisting of the dilute liquid phase, the dense gelled phase, and the crystalline phase. The presence of the dense liquid phase offers a means to investigate mass transport, as explained in chapter 5. Optical micrographs

and comparison with a computer simulation indicates that the presence of a third phase influences the kinetics of the growth process by changing the supply of growth units.

Convection is considered an important mass transport process in protein crystallisation, because it is efficient in supplying impurities to the crystal surface. When present at the crystal surface, these impurities may be incorporated into the crystal and break down the crystal quality. Natural convection is a result of solution density differences created by the growing crystal combined with gravity. When gravity is cancelled, these density differences do not give rise to convection, and the much slower process of mass diffusion remains. To damp convection, various methods have been and are being developed, including experiments in microgravity. Normally, microgravity for a prolonged time as needed for protein crystal growth can only be achieved in outer space. Another way to counteract the gravitational forces is to use a magnetic force, albeit at present not long enough for a typical protein growth experiment. Chapter 6 shows the utilisation of this technique for the paramagnetic salt nickel sulphate hexahydrate, for which an inhomogeneous field of around 1.6 Tesla is required. In these experiments, the concentration profiles are visualised by schlieren microscopy. Proteins typically are diamagnetic and thus require a significantly larger magnetic field, 27 Tesla for lysozyme, to damp convection. Chapter 7 describes this experiment in which shadowgraphy is used to visualise the disappearance of natural convection during lysozyme crystal growth.

Whether convection occurs or not depends not only on gravity but also on (vertical) system size and viscosity. In chapter 8 a study is presented into the influence of polyethylene-glycol on the morphological stability of tetragonal lysozyme. In the almost two-dimensional system of a droplet of solution placed in between two glass microscope slides, the viscosity of the solution controls the rate of mass diffusion. If mass transport limits the growth rate, a crystal looses its faceted shape because its corners protrude, increasing locally the supply of growth units. In the experiments, lysozyme crystal growth is followed from start to depletion of the closed system, i.e. equilibrium between solution

and crystal, showing the whole spectrum of different balances between mass transport and surface kinetics.

The experiments described in this thesis show that the way a protein crystal grows depends on the balance between mass transport and surface kinetics. One can improve a protein crystallisation by in-situ observations of the growth process. By observing the protein crystal growth process, one can explain unexpected end results based on the crystals early life, and even act upon these observation to improve crystallisation conditions, for instance with respect to the balance between mass transport and surface kinetics.

Samenvatting

Eiwitmoleculen spelen een belangrijke rol in de mechanismen van het leven, en nemen deel aan elk proces in levende cellen. Kennis van hun drie-dimensionale structuur kan inzicht verschaffen in de manier waarop ze functioneren en dus in de manier waarop het leven functioneert. Röntgendiffractie (XRD) is de belangrijkste methode om de drie-dimensionale moleculaire structuur van eiwitten te bepalen. Het slagen van deze methode hangt af van de beschikbaarheid van hoge kwaliteit eiwit éénkristallen. Vanwege de brede variëteit aan eiwitmoleculen bestaat er geen alom geldend recept voor het groeien van kristallen die goed genoeg zijn voor röntgendiffractie. Om de juiste kristallisatiecondities voor een gegeven eiwit te vinden moet men vele mogelijke oplossingssamenstellingen uitproberen. Aan de ene kant heeft de technologie het proces om de juiste condities te vinden versneld door het op grote schaal (geautomatiseerd) aftasten van de parameterruimte met behulp van "trial-and-error". Aan de andere kant kan door begrip van de fundamentele processen van de eiwitkristalgroei de parameterruimte verkleind worden.

Kristalgroei vanuit de oplossing, zoals eiwitkristalgroei, kan beschouwd worden als een combinatie van twee opeenvolgende processen; massatransport van groei-eenheden naar het kristaloppervlak, en de inbouw van die groei-eenheden in het kristal, oftewel de oppervlaktekinetiek. De groeisnelheid van het kristal wordt bepaald door de langzaamste van deze twee processen. In dit proefschrift wordt de balans tussen het massatransport en de oppervlaktekinetiek voor eiwitkristalgroei onderzocht met als doel bij te dragen aan het begrip van deze processen. Kippenei eiwit lysozyme (HEWL, naar het Engelse Hen Egg-White Lysozyme) is een vaak gebruikte modelstof voor ei-

witkristalgroei experimenten, waardoor er veel literatuur over beschikbaar is. Om dit tot voordeel te gebruiken, wordt lysozyme in dit proefschrift gebruikt als studieobject voor eiwitkristalgroei.

In hoofdstuk 2 en 3 wordt gebruik gemaakt van atomaire-kracht microscopie (AFM) en optische microscopie om de oppervlaktekinetiek gedurende de groei van lysozyme kristallen te onderzoeken. Met behulp van AFM worden op het (001) vlak van trikliene lysozyme kristallen afgeronde, zeer anisotrope groeispiralen zichtbaar gemaakt. Uit deze AFM metingen blijkt de fractie van HEWL moleculen die blijft plakken aan een kink-positie in een trede op dit oppervlak significant te verschillen van die voor de orthorombische lysozyme polymorf. In hoofdstuk 3 wordt vervolgens optische microscopie gebruikt voor verder onderzoek naar de verschillen tussen de diverse lysozyme polymorfen. Afhankelijk van de symmetrie van de desbetreffende polymorf is de groei van één van een paar tegenoverliggende kristalvlakken geblokkeerd. Dit effect kan toegeschreven worden aan zelfvergiftiging; dat wil zeggen dat de lysozyme moleculen zich in meerdere, metastabiele, oriëntaties aan het oppervlak kunnen hechten. Een dergelijk verkeerd georiënteerd molecuul kan het verdere groeiproces blokkeren. Dit effect zou kunnen verklaren waarom eiwitten vaak lastig te kristalliseren zijn.

In hoofdstuk 4 verschuiven we de aandacht naar massatransport. In dit hoofdstuk wordt de sferulitische groei van lysozyme kristallen onderzocht. Sferulieten zijn bundels kristallijne naaldjes die vaak worden aangetroffen in eiwitkristallisatie experimenten. Omdat ze niet nuttig zijn voor 3D structuurbepalingen met behulp van XRD, worden ze normaal gesproken als ongewenst resultaat beschouwd. De oppervlaktekinetiek speelt een belangrijke rol in de vorming van de typische korenschoofachtige vorm van de lysozyme sferulieten; een model waarin de naaldjes herhaaldelijk aan de punt opsplitsen verklaart de vorm. Wat betreft het massatransport laat de groeikinetiek zien dat voor één enkel naaldje de oppervlaktekinetiek de groeisnelheid domineert, maar dat de hele bundel naaldjes bij elkaar de oplossing sneller uitput dan massadiffusie weer kan aanvullen.

Naast de scheiding in een vaste fase en een verdunde oplossingsfase, kan

lysozyme in oplossing ook een derde fase tonen. Deze fase is een oplossingsfase van hoge dichtheid, en het vormen van deze fase wordt vloeistof-vloeistof fase-scheiding genoemd. De hoge-dichtheidsfase heeft een dusdanig hoge dichtheid dat deze een gel vormt, zodat nieuwe kristalletjes niet in deze fase kunnen gevormd worden, en dus alleen in de verdunde fase nucleëren. De druppels van de hoge-dichtheidsfase om deze kristalletjes heen geven de mogelijkheid massatransport te onderzoeken, zoals uitgelegd in hoofdstuk 5. Optische microscopie en vergelijking met computersimulaties geven aan dat de aanwezigheid van een derde fase de kinetiek van het groeiproces beïnvloedt door verandering in de aanvoer van groei-eenheden.

Men beschouwt convectie als een voor eiwitkristallisatie belangrijk massatransport proces, omdat het een efficiënt proces is voor de aanvoer van onzuiverheden naar het kristaloppervlak. Deze onzuiverheden kunnen, wanneer ze het kristaloppervlak hebben bereikt, ingebouwd worden en op die manier de kwaliteit van het kristal verslechteren. Natuurlijke convectie ontstaat door dichtheidsverschillen in de oplossing en de aanwezigheid van de zwaartekracht. Deze dichtheidsverschillen zijn het gevolg van het groeiende kristal dat de oplossing om zich heen verdund. Schakelt men de zwaartekracht uit, dan zullen de dichtheidsverschillen niet meer leiden tot convectie. Diffusie is dan het enige massatransport proces. Om de convectie te dempen, zijn en worden er verscheidene methodes ontwikkeld, onder andere experimenten in microgravitatie. Normaal gesproken kan men slechts in de ruimte microgravitatie-experimenten gedurende langere tijd doen, zoals nodig voor eiwitkristalgroei. Een alternatieve manier om de zwaartekracht tegen te gaan is het gebruik van een magnetische kracht. Hoofdstuk 6 laat zien hoe deze techniek gebruikt wordt voor kristalgroei van het paramagnetische zout nikkelsulfaat hexahydraat, waarvoor een inhomogeen veld van 1.6 Tesla voldoende is om de convectie te dempen. In deze experimenten worden de concentratieprofielen zichtbaar gemaakt met behulp van schlieren microscopie. Eiwitten zijn vaak diamagnetisch en hebben daarom een sterker inhomogeen magneetveld nodig om convectie te dempen. Voor lysozyme is dit 27 Tesla, een dusdanig sterk veld dat het technisch nog niet mogelijk is om dit in stand te houden

voor de langere tijdsduur die nodig is om een eiwitkristal te groeien. Dat de methode in principe werkt, wordt in hoofdstuk 7 aangetoond met behulp van schaduwgrafie.

De sterkte van de convectie is niet alleen afhankelijk van de zwaartekracht, maar ook van de viscositeit van de oplossing en de (verticale) afmetingen van het systeem. In hoofdstuk 8 wordt de invloed van polyethyleen-glycol op de morfologische instabiliteit van tetragonale lysozyme kristallen onderzocht. In het bijna twee-dimensionale systeem van een druppeltje groei-oplossing tussen twee microscoopglaasjes bepaalt de viscositeit de snelheid van het massatransport. Als massatransport de groeisnelheid bepalende stap is in het kristallisatieproces, kan een kristal zijn gefacetteerde vorm verliezen. Dit fenomeen, morfologische instabiliteit, is het gevolg van het "uitsteken" van de hoeken van het kristal in een bolvormig concentratieprofiel waardoor voor de hoekpunten lokaal meer groei-eenheden voorhanden zijn. Tijdens de experimenten beschreven in dit hoofdstuk wordt de groei van lysozyme kristallen van begin tot eind met de microscoop gevolgd, waarbij het hele spectrum van verschillende verhoudingen tussen massatransport en oppervlaktekinetiek de revue passeert.

Uit de experimenten beschreven in dit proefschrift blijkt dat het verloop van het eiwitkristalgroei afhankelijk is van de balans tussen massatransport en oppervlaktekinetiek. Het eiwitkristallisatie-proces kan verbeterd worden door in-situ de groei van een kristal te volgen. Op basis van deze observaties kan men onverwachte eindresultaten verklaren door wat er in het beginstadium van de groei gebeurt is, en zelfs gedurende het groeiproces de omstandigheden optimaliseren, bijvoorbeeld door de balans tussen massatransport en oppervlaktekinetiek te beïnvloeden.

Nawoord

Ondanks dat ik me graag voorstel dat u, de lezer, de voorgaande 164 bladzijden als een jongensboek in één ruk heeft uitgelezen, weet ik uit ervaring dat de meeste mensen het dankwoord als eerste en vaak als enige lezen. In deze is dit hoofdstuk dus bijzonder, en verdient nog meer aandacht bij het schrijven dan de voorgaande hoofdstukken hebben genoten. De tekst van dit hoofdstuk zoals deze nu voor u ligt is niet de eerste versie. Voorgaande versies bleken keer op keer enigszins repetatief het woord "bedankt" te herhalen. Op zich pas ik me graag aan aan de gebruikelijke usance[1] van het "bedank-lijstje", maar een dergelijke opsomming vind ik niet prettig lezen. Echter, onder het motto van "van je zwakte je sterkte maken", in combinatie met enige interactiviteit, zal dit hoofdstuk naar voorbeeld van een uitgave van een bekend nederlands dagblad[2] meerkeuzevragen bevatten en dus uitmunten in het lijstjes-achtige. Enigzins pretentieus hoop ik hiermee een vermakelijk nawoord te schrijven dat zich kan meten met andere bij de vakgroep Vaste Stof Chemie bekende, memorabele dankwoorden[3,4].

Desalniettemin is het hoofddoel van dit betoog natuurlijk de mensen bedanken zonder wie ik dit dankwoord geeneens had hoeven schrijven. Gedurende de vier jaar van m'n promotie hebben allerlei mensen hun bijdrage geleverd aan de totstandkoming van dit boekje in de vorm van advies, praktisch werk,

---

[1]Vrij naar K. van Kooten en W. de Bie.

[2]Zie "Volkskrant Banen".

[3]S.X.M. Boerrigter, "Modeling of Crystal Morphology", thesis, Katholieke Universiteit Nijmegen, 2003.

[4]M. Plomp, "Crystal growth studied on a micrometer scale", thesis, Katholieke Universiteit Nijmegen, 1999.

of morele en sociale ondersteuning. Doordat het "eiwitproject" waarbinnen ik mijn promotieonderzoek heb uitgevoerd een samenwerkingsproject was van drie vakgroepen van de Radboud Universiteit, heb ik vanuit verschillende hoeken deze bijdragen mogen ontvangen en is dit proefschrift onder auspiciën van het maximum aantal (co)promotores tot stand gekomen. **1. Het maximum aantal is**

a. 1 promotor en 3 copromotores.

b. 3 promotores en 1 copromotor.

c. 2 promotores en 2 copromotores.

Het grootste deel van mijn onderzoek heb ik uitgevoerd in de vakgroep Vaste Stof Chemie. Hier ben ik in wetenschappelijke zin voornamelijk ondersteund door Willem van Enckevort, copromoter, en Elias Vlieg, promotor. Willem, dankjewel voor de begeleiding door de jaren heen, en de vele prettige al dan niet wetenschapppelijke discussies. Van de bewonderenswaardige wijze waarop je aanduidde waar de krenten in de pap van mijn metingen zaten heb ik veel geleerd (mooi verwoord in een ander dankwoord: "...een begenadigd interpretator zoals jij..."[5]). Uiteraard zal ook je stijl van onderwijzen, promotie- en afstudeertoespraken, en manier van wetenschap bedrijven in het algemeen, me in zeer positieve zin bijblijven.

Elias, bedankt voor je enthousiamse voor ons onderzoek en de wetenschappelijke discussies, en de ruimte tot zelfontplooïïing de je ons promovendi biedt. Je openheid voor discussie, niet gebonden door de hiërarische structuren die men wellicht zou kunnen verwachten binnen een vakgroep, vond ik erg prettig. Aan de gezamenlijke nachtdienst bij het ESRF, naast de wetenschappelijke plicht bestaande uit propjes-basketbal en vacuümring werpen, denk ik met veel plezier terug. **2. Het European Synchrotron Radiation Facility (ESRF) ligt in**

a. Grenoble, Frankrijk.

b. Genève, Zwitserland.

c. Hamburg, Duitsland.

---

[5]E. van Veenendaal, "From an Atomistic to a Continuum Description of Crystal Growth", thesis, Katholieke Universiteit Nijmegen, 2001.

Hoewel Hugo niet officieel met het eiwitproject te maken had, heb ik goed van zijn kennis kunnen profiteren, vooral het jaar dat ik bij hem op de kamer zat. Dat jaar heb ik menigmaal mensen al dan niet telefonisch kunnen melden dat je ergens in bespreking zat. Daarentegen had ik ook de luxe ten opzichte van die mensen dat ik altijd wist wanneer je er was en dus makkelijk allerlei vragen over polymorfie en fasediagrammen op je los kon laten (naast natuurlijk verder geklets met grote kernen van waarheid). Hugo, bedankt! En succes met het forsen.

Zoals gezegd, heb ik niet alleen bij de afdeling Vaste Stof Chemie rondgehangen, een deel van het onderzoek vond plaats bij het HFML. **3. Waar staat HFML voor?**

a. High Flux Magnet Laboratory.

b. High Field Magnet Laboratory.

c. High Frequency Magnet Laboratory.

Jan-Kees en Peter (copromotor), bedankt voor jullie onmisbare bijdrage van kennis over experimenten in hoge magneetvelden en magnetische levitatie. Jan-Kees wil ik graag bedanken voor het lezen van mijn manuscript, voor zijn interesse voor onze metingen, en het kritisch lezen van onze publicaties. Ook Peter wil ik graag bedanken voor het, gelijk aan Jan-Kees, geïntereseerd zijn hoofd om de hoek van het lab steken wannneer Paul en ik bezig waren, en het meehelpen met onze publicaties. Voor de goeie technische ondersteuning voor onze magneet-experimenten wil ik graag Jos R., Lijnis, en Ramon bedanken.

De derde vakgroep betrokken bij het eiwit-project was de biochemie-groep van Wim de Grip, ook mijn promotor. Wim, bedankt voor je raad en daad vanuit de biochemische hoek. Hoewel de tijd dat ik daadwerkelijk bij je vakgroep heb doorgebracht klein was, was je inbreng in ons project bij de meetings van grote waarde. Jenny en Petra wil ik graag bedanken voor de crash course biochemie en eiwitkristalgroei die ik aan het begin van m'n promotietijd van hen gekregen heb.

4. En natuurlijk grote

a. dank

b. dank

c. dank

aan Paul, mijn collega-promovendus op het eiwit-project, überhaupt zowiezo vanwege de mooie resultaten die we samen bereikt hebben. En daarnaast voor het prettige samenwerken, discussiëren, praten, ouwehoeren, koffie drinken, conferenties bezoeken, etc. Samengevat, het was goed!

I would also like to thank prof. García Ruiz for reading my manuscript, and prof. Tsukamoto for allowing me and Paul to visit his laboratory to learn about interferometry. Ook wil ik graag prof. Wijmenga bedanken voor het plaatsnemen in de manuscript-commissie.

René de Gelder en Jan Smits wil ik bedanken voor de XRD metingen aan mijn eiwitkristallen.

Als promovendus kan je de mazzel hebben dat je studenten mag begeleiden, in ruil waarvoor ze helpen met het uitvoeren van je vele experimenten. Als eerste mocht ik Patrick begeleiden. Patrick, bedankt dat je voor mij die vele uren in de AFM-kelder hebt gezeten. **5. Wat is de AFM-kelder?**

a. De kelder van de Autoriteit Financiële Markten.

b. Een soort SM-kelder, maar dan voor wetenschappers.

c. De kelder onder het voormalige bèta-gebouw van de RU waar de atomaire-kracht microscoop stond.

Daar heb je met volharding AFM metingen gedaan aan boterzachte lysozyme kristalletjes, wat geresulteerd heeft in een mooi artikel in Crystal Growth & Design. De tweede student die ik onder mijn hoede kreeg was Mirjam. Mirjam, je hebt allerlei exploratieve experimenten voor me gedaan, maar ook een succesvolle reeks experimenten op het gebied van sferulieten-groei met als resultaat een mooie publicatie in het Journal of Physical Chemistry B. Van je kunde om allerlei apparatuur bijelkaar te bietsen bij andere afdelingen heb ik dankbaar gebruik gemaakt. Bedankt voor je bijdrage aan dit proefschrift! Ook heb ik nog een student gehad voor een stage voor een paar weken (hoe al die verschillende soorten stages precies heten is me niet bijgebleven/nooit

duidelijk geworden). Frank heeft me goed geholpen met de basis voor wederom een artikel, door strak het "instability diagram" af te scannen, waarvoor dank!

6. Het "instability diagram" staat uitgelegd in hoofdstuk

a. 3 van dit proefschrift.

b. 5 van dit proefschrift.

c. 8 van dit proefschrift.

Ondersteuning komt in vele vormen en maten, en de sociale kanten van een werkomgeving mogen niet onderschat worden. Zoals zovele wetenschappers, heb ik tijdens mijn promotie een lichte afhankelijkheid van koffie ontwikkeld. Mede oorzaak hiervan is de sterke koffie en gezellige ambiance "Chez Jan van Kessel", elke ochtend. Jan bedankt voor de goeie koffie en kick start elke dag! Gedurende de vier jaar die een promotie-tijd duurt is het een komen en gaan van collega's, collega-promovendi, en studenten, zeker als je bij twee vakgroepen over de vloer komt. Dus, voor alle gezellige koffiepauzes, lab-uitjes, vrijdagmiddagborrels, Andreas, Cristina, Cécile, Daniel, Edwin, Elizabeth, Erik, Fieke, Frans, Gerbe, Giorgia, Hans E., Hans de J., Harry, Henk, Herma, Hung, Igor, Ine, Iris, Ismail, Jan L., Janneke, Jelena, Jeroen, Jordy, Jos G., Jos P., Maaike, Martha, Menno, Natalia, Neda, Paul T., Paul V., Rienk, Sander, Saskia, Stef, Teun, Uli, Victor, Wim N., Wiesek, Zjak, bedankt!

Dit dankwoord zou niet compleet zijn zonder vermelding van de geduchte tegenstanders op de tafelvoetbaltafel: Gerbe, Günther, John (met dank voor de tafel!), Joop, Peter, Tim, en natuurlijk mijn "teamgenoot" en mede-krul-lebol Wim N., allemaal met hun eigen specifieke kwaliteiten (er bestaat een officieuze mondeling overgedragen lijst met naar al deze mensen vernoemde "shots"/technieken). **7. De "klinker" is ook een bekend fenomeen bij het tafelvoetbal. Een klinker is**

a. een schot dat gelijk een baksteen het doel inrolt.

b. een schot waarbij de bal via de achterkant van het doel weer naarbuiten komt rollen, vaak gepaard gaand met een hard geluid van de weerkaatsing.

c. een schot dat zo mooi is dat men een klinker als "Aahh" of

"Oooh" laat horen uit bewondering.

Buiten de universiteit om zijn er natuurlijk ook nog mensen die op enigerlei manier mij moreel ondersteund hebben. Mijn ex-huisgenoot Marcel wil ik bedanken voor de gezellige tijden aan de Johannes Vijghstraat, en ook later na je verhuizing naar een luxueus onderkomen elders in Nijmegen. Alle mensen van NSAV 't Haasje bedankt voor de gezellige trainingen, clubweekends en wedstrijdbezoeken.

Mijn ouders wil ik graag bedanken voor hun steun door de jaren heen. Het mooie van dit boekje is dat ik mijn grote dank voor jullie steun zwart op wit kan vastleggen, inclusief ISBN-nummer!

En als laatste wil ik Sas bedanken voor haar steun.

14 januari 2008,
Maurits

8. Het aantal keer dat het woord "bedankt" in dit hoofdstuk voorkomt is een priemgetal. Welk getal?
a. 7
b. 11
c. 13
d. 17
e. 131

List of Publications

"Growth inhibition of protein crystals: a study of lysozyme polymorphs"
M.C.R. Heijna, W.J.P. van Enckevort, and E. Vlieg
Crystal Growth & Design, 2008, **8** (1), 270-274.

"Crystal growth in a three-phase system: diffusion and liquid-liquid phase separation in lysozyme crystal growth"
M.C.R. Heijna, W.J.P. van Enckevort, and E. Vlieg
Physical Review E, 2007, **76** (1), 011604.

"PEG-induced morphologically unstable growth of tetragonal hen egg-white lysozyme crystals"
M.C.R. Heijna, F.F.M. van Wamel, W.J.P. van Enckevort, and E. Vlieg
Crystal Growth & Design, 2007, **7** (10), 1999-2008.

"A comparison between simulations and experiments for microgravity crystal growth in gradient magnetic fields"
P.W.G. Poodt, M.C.R. Heijna, P.C.M. Christianen, W.J.P. van Enckevort, J.C. Maan, and E. Vlieg
Submitted to Crystal Growth & Design, 2007.

"Magnetically controlled gravity for protein crystal growth"
M.C.R. Heijna, P.W.G. Poodt, J.L.A. Hendrix,
K. Tsukamoto, P.C.M. Christianen, W.J.P. van Enckevort, W.J. de Grip,
J.C. Maan, and E. Vlieg
Applied Physics Letters, 2007, **90** (26), 264105.

"Spherulitic growth of hen egg-white lysozyme crystals"
M.C.R. Heijna, N.J. Theelen, W.J.P. van Enckevort, and E. Vlieg
Journal of Physical Chemistry B, 2007, **111** (7), 1567–1573.

"Using gradient magnetic fields to suppress convection during crystal growth"
P.W.G. Poodt, M.C.R. Heijna, K. Tsukamoto, W.J. de Grip,
P.C.M. Christianen, J.C. Maan, W.J.P. van Enckevort, and E. Vlieg.
Crystal Growth & Design, 2006, **6** (10), 2275–2280.

"An atomic force microscopy study of the (001) surface of triclinic hen egg-white lysozyme crystals"
M.C.R. Heijna, P.B.P. van den Dungen, W.J.P. van Enckevort, and E. Vlieg.
Crystal Growth & Design, 2006, **6** (5), 1206–1213.

"Suppression of convection using gradient magnetic fields during crystal growth of $NiSO_4 \cdot 6H_2O$"
P.W.G. Poodt, M.C.R. Heijna, K. Tsukamoto, W.J. de Grip,
P.C.M. Christianen, J.C. Maan, W.J.P. van Enckevort, and E. Vlieg.
Applied Physics Letters 2005, **87** (21), 214105.

"Structure of the {1 1 1} NaCl crystal surface grown from solution in the presence of $CdCl_2$."
N. Radenović, W.J.P. van Encekevort, D. Kaminski, M.C.R. Heijna, and E.Vlieg
Surface Science, 2005, **599** (1-3), 196–206.

Curriculum Vitae

Maurits Heijna was born on the 24th of September 1976 in Utrecht, the Netherlands. From 1988 to 1994, he was in high-school ("gymnasium") at the "De Bruijne Lyceum" in Utrecht. After graduation he started his studies of physics at the Vrije Universiteit in Amsterdam. In January 2002, he obtained his MSc. degree in experimental physics after concluding the research for his master thesis in the Solid State Physics. The subject of his master thesis was the "Pulsed Laser Deposition of Yttrium Dihydride Thin Films". Upon conclusion of his MSc., he travelled through New-Zealand for a few months. In November 2002, he started as a PhD-student at the Radboud University in Nijmegen, partly in the Solid State Chemistry group of prof. Vlieg, partly at the High Field Magnet Laboratory of prof. Maan. The PhD research was part of a research project of these two groups and that of prof. de Grip on the improvement of protein crystal quality using gradient magnetic fields. As part of this project, he visited the laboratory of prof. Tsukamoto in Sendai, Japan, presented a poster at a Gordon Research Conference in South Hadley in Massachusetts, USA, and gave an oral presentation at the 2nd International Workshop on Materials Analysis and Processing in Magnetic Fields in Grenoble, France. Since February 2007, Maurits is working as a scientist in the Solar Energy unit of the Energy Research Centre of the Netherlands (ECN) in Petten.

tetragonal hen egg-white
lysozyme crystal